VYSOKÉ UČENÍ TECHNICKÉ V BRNĚ
BRNO UNIVERSITY OF TECHNOLOGY

FAKULTA STROJNÍHO INŽENÝRSTVÍ
FACULTY OF MECHANICAL ENGINEERING

ENERGETICKÝ ÚSTAV
ENERGY INSTITUTE

KAVITACE V MIKROFLUIDICE
CAVITATION IN MICROFLUIDICS

BAKALÁŘSKÁ PRÁCE
BACHELOR'S THESIS

AUTOR PRÁCE — Martin Holub
AUTHOR

VEDOUCÍ PRÁCE — doc. Ing. Pavel Rudolf, Ph.D.
SUPERVISOR

BRNO 2016

VYSOKÉ UČENÍ TECHNICKÉ V BRNĚ
FAKULTA STROJNÍHO INŽENÝRSTVÍ

Zadání bakalářské práce

Ústav:	Energetický ústav
Student:	**Martin Holub**
Studijní program:	Strojírenství
Studijní obor:	Základy strojního inženýrství
Vedoucí práce:	**doc. Ing. Pavel Rudolf, Ph.D.**
Akademický rok:	2015/16

Ředitel ústavu Vám v souladu se zákonem č.111/1998 o vysokých školách a se Studijním a zkušebním řádem VUT v Brně určuje následující téma bakalářské práce:

Kavitace v mikrofluidice

Stručná charakteristika problematiky úkolu:

Využití kavitace v oblasti mikrofluidiky nabízí velký potenciál především v oblasti biomedicíny a chemie (cílená doprava léčiv, desinfekce, atd.). Cílem práce je zjištění současného stavu dané problematiky a provedení výpočtové simulace kavitujícího proudění v kanálu se šířkou v řádu stovek mikrometrů.

Cíle bakalářské práce:

1. Úvod, definice základních pojmů
2. Rešerše, současný stav poznání
3. Výpočtová simulace kavitace v mikrokanálu
4. Návrh experimentu

Seznam literatury:

Franc, J.P., Michel, J.M.: Fundamentals of Cavitation, Springer, 2005

Rooze et al: Hydrodynamic cavitation in micro channels with channel sizes of 100 and 750 micrometers, Microfluidics and nanofluidics 12(1-4):499-508, 2012

Termín odevzdání bakalářské práce je stanoven časovým plánem akademického roku 2015/16

V Brně, dne

L. S.

doc. Ing. Jiří Pospíšil, Ph.D. ředitel ústavu	doc. Ing. Jaroslav Katolický, Ph.D. děkan fakulty

SUMMARY

Microfluidics has recently gained attention of numerous research groups. Its applications are manifold and could potentially bring about significant advances in several fields including healthcare, battery energy storage and high-performance computing.

The thesis “Cavitation in Microfluidics” deals with cavitation at the microscale level. Its relevance to the up-to-date research is emphasized by recent studies which show that various aspects of cavitating flows observed at microscale often differ from their macroscale counterparts. Better understanding of this phenomenon can be directed towards addressing crucial challenges of microfluidics including fluid mixing and pumping. Cell stretching and lysis, chemical catalysis and targeted drug delivery count among other possible applications.

The first part of this work deals in turn with fluid mechanics and chemistry fundamentals of cavitation. This is followed by concise overview of its conventional as well as microscale applications. Finally, numerical flow simulations of cavitating flow in two distinct domains are presented together with results analysis and validation. The results include distribution of phases, report on areas of recirculation and influence of changing cavitation number on flow variables. Based on this, an experiment enabling accurate investigation of flow characteristics is proposed. This will enable to draw parallels between the experimental and numerical investigations and allow for evaluation of the suitability of laminar model. This thesis lays foundation for future work on the topic planned at Brno University of Technology, hence recommendations for prospective endeavors are included.

KEYWORDS

Microfluidics, Cavitation, CFD, μ-PIV, MEMS

ABSTRAKT

Mikrofluidice byla v posledních letech věnována intenzivní pozornost výzkumnými týmy takřka po celém světě. Její možné aplikace jsou velmi početné, zejména pak v oblasti zdravotnictví, ukládání energie do baterií nebo chlazení vysoce výkonných počítačů.

Bakalářská práce „Kavitace v mikrofluidice“ se zabývá kavitací na mikro-měřítku. Nedávný výzkum ukazuje, že mnohé charakteristiky kavitujícího proudění na takto malých rozměrech se podstatně liší oproti charakteristikám pozorovaným na konvenčních makro-rozměrech. Toto podtrhuje relevantnost této práce. Lepší pochopení tohoto jevu může být využito například k řešení jednoho ze značných úskalí mikrofluidiky a to sice mísení tekutin, nebo dále také k jejich pumpování. Mezi další možné aplikace se řadí mechanické namáhání a rozklad mikroorganismů a buněk, katalýza chemických reakcí a cílená doprava léčiv.

První část této práce je věnována postupně základům z oblasti mechaniky tekutin a chemie kavitace. Tato část je následována stručným přehledem aplikací kavitace a to jak na měřítkách tradičních, tak na měřítkách v řádech mikrometrů. Poté je uveden popis numerického řešení kavitujícího proudění spolu s analýzou a ověřením získaných výsledků. Mezi výsledky je například popis rozložení fází, informace o tom, kde dochází k recirkulaci a také přehled vlivu změny kavitačního čísla na tvar a charakteristiky proudění. V závěrečné části práce je pak na základě získaných znalostí navržen experiment, který umožní dále studovat tuto problematiku a poslouží také k vyhodnocení vhodnosti laminárního modelu. Tato bakalářská práce slouží jako základní kámen pro další výzkum v této oblasti plánovaný na Vysokém učením technickém v Brně, a z tohoto důvodu jsou v textu uvedena doporučení pro další práci.

KLÍČOVÁ SLOVA

Mikrofluidika, Kavitace, CFD, μ-PIV, MEMS

BIBLIOGRAPHIC INFORMATION

HOLUB, M. *Kavitace v mikrofluidice.* Brno: Vysoké učení technické v Brně, Fakulta strojního inženýrství, 2016. 65 s. Vedoucí bakalářské práce doc. Ing. Pavel Rudolf, Ph.D..

ACKNOWLEDGMENTS

Foremost, I would like to express my gratitude to my supervisor doc. Ing. Pavel Rudolf Ph.D. for his open-mindedness when devising a topic for this thesis. I would like to further thank to Ing. Darina Jašíková, Ph.D. from Technical University in Liberec for valuable pieces of advice on the design of experiment.

Last but definitely not least, I would like to thank my family for the support they have provided me throughout my entire life and their great patience.

AFFIRMATION

I declare that this bachelor thesis is the result of my own work led by doc. Ing. Pavel Rudolf, Ph.D. and all used sources are duly listed in the bibliography. I proclaim that all presented information is true and valid to the best of my knowledge.

Martin Holub

In case of any questions regarding the presented thesis, do not hesitate to contact me at: mholub@outlook.cz.

TABLE OF CONTENTS

DEFINITION OF TERMS

This chapter serves for fast reference. Reader will find here brief definitions of key terms used throughout the thesis. The definitions are based mainly on [1], [2], [3].

Axisymmetric flow:

A flow specified by cylindrical coordinates (r, θ, z) which does not vary in angular direction. All derivatives with respect to θ are zero.

Cavitation:

Formation of vapor bubbles in a liquid under very low pressures.

Computational Fluid Dynamics (CFD):

Numerical method used to estimate field variables on a discretized grid (i.e. mesh). Conservation laws with boundary and initial conditions in mathematical discretized form are applied.

Continuum approximation:

Treatment of matter as continuous distribution of finite mass differential volume elements. Each element must contain enough molecules so that their individual effects do not need to be considered. For liquid flows this particularly means, that characteristic length scale must be greater than $2 - 5\ nm$ (i.e. 10–50 times bigger than characteristic free path of the system).

Dynamic pressure:

The term in Bernoulli equation that represents kinetic energy per unit volume, namely $\frac{1}{2}\rho v^2$.

Fully developed flow:

Used to describe a flow region where the velocity field is constant along a specified direction in the flow. The derivatives of velocity with respect to variable describing this direction are zero. In a flow in a channel this direction is an axial one.

Gage pressure:

Pressure relative to atmospheric pressure.

Incompressible flow:

A fluid flow where density variations are small and can be neglected.

Inviscid flow:

A fluid flow in which viscous forces are negligible in comparison to other forces.

Jet:

A friction-dominated region issuing from an orifice and formed by surface boundary layers. Jets are characterized by highest velocities in the center and lowest velocities at the edges.

Laminar flow:

A flow in which the fluid moves in orderly sheets of lamina. For specified boundary conditions, a single flow is experimentally observed and this is stable to perturbations. Steady boundary conditions result in steady laminar flows.

Microfluidics:

Flows of fluids and suspensions in submillimeter-sized systems influenced by effects of external forces.

Newtonian fluid:

A fluid which strain rate is proportional to the applied shear stress. The constant of proportionality is viscosity (also called dynamic viscosity).

No-slip condition:

A boundary condition that specifies that at the interface of a fluid and motionless surface their velocities are equal, thus zero.

Static pressure:

Another term for pressure used to distinguish it from dynamic pressure appearing in Bernoulli equation.

Steady flow:

A flow in which all fluid variables may vary spatially but remain constant in time. In steady flows are all partial derivatives in time zero.

Transitional flow:

Flow that is no longer laminar, but is not yet fully dominated by random vortical structures and cannot be described as turbulent.

Turbulent flow:

A flow which structure is dominated by fluid motions that are random. Turbulent flow is always three dimensional and unsteady, even if the boundary conditions are steady.

Vapor pressure:

The pressure threshold under which a fluid at given temperature evaporates and forms vapor cavities in bulk liquid.

Viscosity:

Fluid property that quantifies the ratio of shear stress to strain rate of a fluid particle. In the bulk, viscosity describes how much certain fluid resists deformation when subjected to shear stress. It is temperature-dependent. The terms viscosity and dynamic viscosity are used interchangeably.

LIST OF SYMBOLS AND ABBREVIATIONS

NOMENCLATURE

Symbol	Meaning	Units
c_{gp}	gas specific heat measured at constant pressure	$J \cdot kg^{-1} \cdot K^{-1}$
E_a	activation energy	$J \cdot mol^{-1}$
R_m	universal gas constant ($R_m = 8.314\, J(Kmol)^{-1}$)	$J \cdot K^{-1} \cdot mol^{-1}$
S_α	net mass transfer source term	$kg \cdot\ m^{-3} \cdot\ s^{-1}$
c_{gv}	gas specific heat measured at constant volume	$J \cdot kg^{-1} \cdot K^{-1}$
k_B	Boltzmann's constant ($k_B = 1.38 \times 10^{-23}\, JK^{-1}$)	$J \cdot K^{-1}$
$\dot{m}$	mass flow rate	$kg \cdot s^{-1}$
τ_p	particle lag time	s
τ_{rr}	radial component of viscous stress tensor	Pa
$\boldsymbol{\tau_{ij}}$	viscous stress tensor	Pa
Δ	increment	$-$
∇	vector differential operator nabla	$-$
h	height, depth	m
A	area; pre-exponential factor	$m^2;\ s^{-1}$
C	concentration of gas	$kg \cdot m^{-3}$
CN	cavitation number	$-$
D	particle diffusivity	$m^2 \cdot s^{-1}$
D, d	diameter	m
H	Henry's constant	$s^2 \cdot m^{-2}$
L	characteristic dimension	m
Q	volume flow rate	$m^3 \cdot s^{-1}$
R	bubble radius	m
Re	Reynolds number	$-$
Sk	Stokes number	$-$
T	temperature; period	$°C, K$; s
V	volume	m^3
f	frequency	s^{-1}, Hz
i	index	$-$
j	index	$-$
k	rate constant	s^{-1}
m	integer, pixel offset	$-$
n	bubble number density	m^{-3}
n	polytropic index, pixel offset	$-$
p	pressure	Pa
p	number of pixels	$-$
q	number of pixels	$-$
r	radial coordinate – cylindrical coordinates	m
s	integer	$-$
t	time	s
v	velocity	$m \cdot s^{-1}$
w	width	m
x	x coordinate	m

y	y coordinate	m
z	z coordinate	m
α	vapor volume fraction	$-$
γ	surface tension	$N \cdot m^{-1}$
δ	relative radius change	$-$
ε	ratio of amplitude of pressure oscillations to magnitude of static pressure	$-$
θ	angle of angular coordinate – cylindrical coordinates	$rad, °$
μ	dynamic viscosity	$Pa \cdot s$
ρ	density	$kg \cdot m^{-3}$
σ	cavitation number	$-$
τ	shear stress	Pa
φ	azimuthal spherical coordinate	$rad, °$
ω	angular frequency	$rad \cdot s^{-1}$
ϑ	half of apex angle, colatitude spherical coordinate	$rad, °$
$\varkappa$	adiabatic coefficient	$-$
ϕ	cross correlation	$-$

LIST OF ABBREVIATIONS

Abbreviation	Meaning
AC	Acoustic cavitation
AOP	Advanced Oxidation Process
BUT	Brno University of Technology
CCD	Charge-coupled device
CFD	Computational fluid dynamics
DNA	Deoxyribonucleic acid
DOC	Dissolved oxygen concentration
HC	Hydrodynamic cavitation
LOD	Luminescent dissolved oxygen
MEMS	Microelectromechanical systems
PDMS	Polydimethylsiloxane
PIV	Particle image velocimetry
PMMA	Polymethyl methacrylate
RMS	Root-mean-square
TUL	Technical University in Liberec
US	Ultrasound

MEANING OF SUBSCRIPTS

Subscript	Meaning
0	initial (volume, radius), natural (frequency, angular frequency)
1	initial, upstream (pressure, velocity)
2	final, downstream (pressure, velocity)
∞	value far from observed point, property of bulk (pressure)
h	hydraulic (diameter)
Ch	choking (cavitation number at, volume flow rate at)
DS	downstream, reference value (of pressure)

Subscript	Meaning
a	activation (energy)
c	critical (radius, pressure); at constriction (velocity, Reynolds number)
f	property of fluid (temperature of)
g	property of gas (partial pressure)
i	inception (cavitation number at)
l	property of liquid (density)
o	orifice (width, cross section area)
p	channel (width, cross-section area), property of particle (density)
r	radial (component of stress tensor); triple (point of water)
s	saturation (concentration of gas at)
t	total (period of oscillations)
v	property of vapor (pressure, density)
α	property of vapor volume fraction (mass source term)

MEANING OF SUPERSCRIPTS

Superscript	Meaning
$\dot{}$ (overdot)	time derivative
$'$ (prime)	modified variable, relative size

1 INTRODUCTION

Microfluidics is a topic that has recently gained attention of research groups practically all over the globe. The applications are numerous and could eventually generate significant advances in several domains including healthcare, energy storage and high-performance computing. Similarly, cavitation is a topic that attracts interest of many researchers worldwide. It can be regarded as detrimental or it can be ingeniously exploited to achieve various means including water disinfection and harvesting of biological material. The introductory chapter explains basics of cavitation which are built upon in following text.

1.1 THE PHYSICAL PHENOMENON OF CAVITATION [2]

Cavitation is defined as the breakdown of a liquid medium under low pressures. The breakdown results in creation of cavities, i.e. voids filled with vapor and gas, in liquid volume. It can occur in any type of liquid, but the main concern is with cavitation in water as it is the most ubiquitous medium. Therefore, if not stated otherwise, water is going to be the discussed fluid in this thesis.

Cavitation can be induced in either moving or static liquid. In the former case we call it **hydrodynamic** cavitation (HC). It is often encountered when liquid flows through narrow passages and constrictions. It appears frequently around propeller and turbine blades and also around wings. In the latter case, cavitation arises in liquid that is static or nearly static. It is mostly the case of oscillating pressure field applied to the liquid medium, this type is then referred to as **acoustic** cavitation (AC).

Apart from these, another two types of cavitation generation [4] are: **optical**, which can be realized by a laser-induced plasma that expands and rips cavities in the fluid. And **particle-induced**, this way of cavities production is based on introduction of high energy particles into the fluid. Both these two methods of cavitation generation are mostly used for single-bubble investigations and theoretical studies. For application in processes only the hydrodynamic and acoustic cavitation are considered [4].

1.2 ON EFFECTS OF PRESSURE

The transition from initially homogeneous medium to two phase mixture of liquid and cavities is driven by low pressure. There exists a certain limiting threshold value of pressure that marks the phase change. This value is known as vapor pressure p_v. For water at temperature 20 °C and 25 °C it is equal to 2 339 Pa and 3 540 Pa respectively [5].

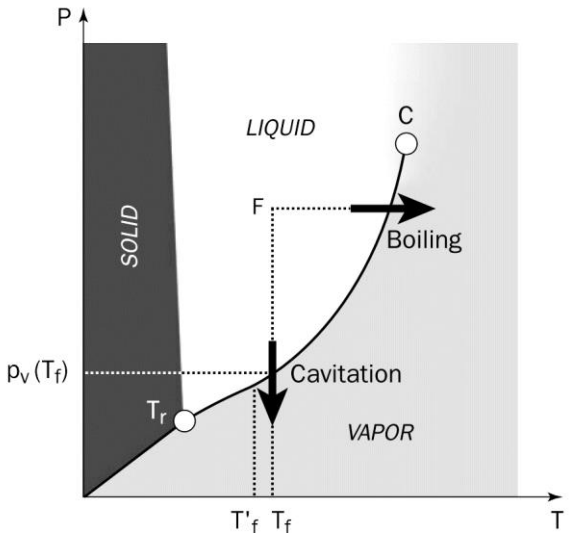

Figure 1.1: *Phase diagram of water [2]. T_r is triple point of water*

Let us consult the phase diagram of water (Figure 1.1) to understand better the way in which phase change in water occurs. The parallel between boiling and cavitation can be seen. We observe that pressure remains constant, when we bring water to evaporate, i.e. to change phases, when putting a pot on stove and heating it up. Nevertheless, the result is quite like what happens when we keep the value of temperature fixed and induce the phase change by lowering the

pressure. In both cases bubbles appear in initially homogeneous liquid. We further observe that vapor pressure p_v is function of temperature. If the ambient temperature rises, so does the tendency of the liquid to cavitate. This is caused mainly by increase of vapor pressure and decrease of surface tension. In ideal case, cavitation happens isothermally. This assumption stems from the fact that the phase change from liquid to gaseous form necessitates very little energy to be extracted from the bulk. If we want to be more precise we define the **thermal delay**, which is the difference $T_f - T'_f$. The thermal delay represents the deviation from the idealistic isothermal phase change assumption. It increases for bigger bubbles and remains small for nuclei.[1]

The temperature of bulk medium is of great concern in many applications, especially in microfluidics when sensitive biological material is to be treated [6]. Moreover, when the cavitation is to be induced acoustically, by ultrasound (US) of high frequencies, the temperature increase due to energy transmission must be often carefully controlled.

To predict hydrodynamic cavitation inception in case of unidirectional flow, it is sufficient to calculate the minimal value of pressure that Bernoulli equation yields. This value should then be compared with a threshold pressure value for cavitation which usually is the vapor pressure p_v. This is simplified approach. It ignores for example the effect of velocity profile shape (this is usually caught up on by introducing correction factor) or the changes in pressure distribution owing to occurrence and collapse of cavitation bubbles clouds in liquid.

[1] We make a distinction between the terms nucleus and bubble. Nuclei are small gas and vapor inclusions that are present in any liquid, their dimensions are of the order of micrometers. Once the nucleus grows, exceeds certain size and becomes observable, we refer to it as bubble. Nuclei can be then called microbubbles [2].

2 CAVITATION GENERATION

2.1 GENERATION OF HYDRODYNAMIC CAVITATION

Several methods of inducing hydrodynamic cavitation are used [7]. The simplest consists of introducing a constriction in the liquid flow. Other may be based on rotating elements [8] or special combination of orifice and blade creating pressure oscillations [9]. The shape of the constriction may vary. Commonly used designs are venturi (i.e. convergent-divergent nozzle) or orifice plate. The latter may have arbitrary number of small constrictions. Their exact size and position is to be optimized with respect to desired outcome and working conditions [10].

The pressure-velocity relationship of the flowing liquid is expressed by **Bernoulli equation:**

$$p_1 + \rho \frac{v_1^2}{2} = p_2 + \rho \frac{v_2^2}{2} = const, \tag{2.1}$$

where p_1, p_2 – pressure up- and downstream $[Pa]$ and v_1, v_2 – velocity up- and downstream $[m \cdot s^{-1}]$.

The increase of velocity induced by constriction will result in pressure head drop. This is depicted schematically in Figure 2.1. If it drops below the threshold value (usually vapor pressure of liquid at operating temperature denoted p_v) cavities are generated. The region with lowest pressure is referred to as Vena contracta. Once the pressure recovers above the threshold value, the mass transfer reverses and the bubbles tend to collapse.

A dimensionless number known as the **cavitation number** (σ, sometimes also CN) characterizes the degree of development of cavitation. It is defined as follows:

$$\sigma = \frac{p_{DS} - p_v}{\frac{1}{2}\rho v_c^2}, \tag{2.2}$$

p_{DS} – fully recovered downstream pressure (i.e. p_2) $[Pa]$, v_c – the mean liquid velocity in the constriction $[m \cdot s^{-1}]$.

When we evaluate the cavitation number at the instant when first cavities start to develop we obtain the **cavitation number at inception** σ_i. Ideally cavitation occurs as soon as $\sigma \leq 1$. However cavitation has been observed to occur at higher cavitation numbers (in the range 1 to 4) [7], possibly due to presence of dissolved gas or significant impurities housing nuclei in the liquid medium. Yan and Thorpe [12] have also shown that σ is a function of the flow geometry and mostly increases with increasing size of the constriction. This has been confirmed by recent studies on hydrodynamic cavitation in microscale constrictions [13], [14] where cavitation numbers as low as 0.3 were reached without any observable cavitation occurring.

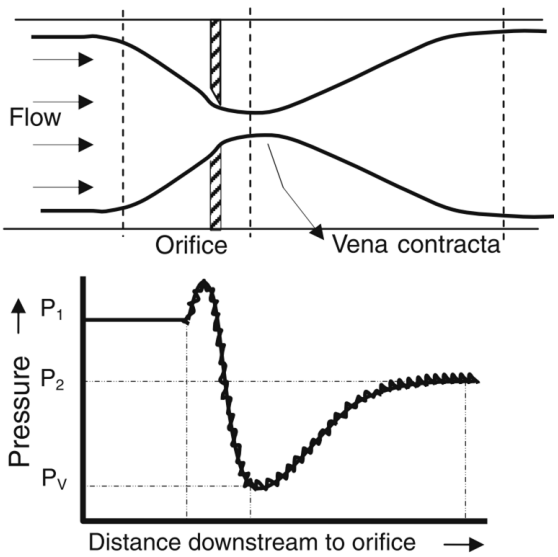

Figure 2.1: *Fluid flow and pressure variation during hydrodynamic cavitation [11]*

2.2 GENERATION OF ACOUSTIC CAVITATION

Generation of cavitation by ultrasound (i.e. acoustically) can be achieved by devices based on two well-known physical phenomena, electrostriction and

magnetostriction. Both of them result in dimension change of material. This deformation is then translated into the bulk liquid, producing pressure oscillations.

2.2.1 ELECTROSTRICTION AND PIEZOELECTRIC EFFECT

In simplified terms, both effects are based on polarization of elementary dipoles in given dielectric[2] material. The dipoles are exposed to external electrical field and subsequently partially oriented, in other words polarized, and this leads to bulk dimension change. The difference between electrostriction and piezoelectric effect lies in their dependencies on intensity of applied field. Electrostriction deformation scales with square of the intensity, whereas piezoelectric deformation depends on the intensity linearly. This difference stems from absence of center of symmetry in crystal lattice of piezoelectric materials (e.g. $SiO_2, BaTiO_3$), this characteristic thus represents a necessary condition for an material to be piezoelectric. On the other hand, all dielectrics, irrespective of symmetry, show electrostriction [15].

2.2.2 MAGNETOSTRICTION

The next phenomenon, magnetostriction, is in many ways similar to electrostriction. It arises in all ferromagnetic[3] materials subdued to effect of external magnetic field. This field causes orientation of domains and subsequently dimension change of given component. The material must have crystal lattice and the deformation does not grow linearly. The process also shows significant hysteresis [15].

It is interesting to note that all these effects (i.e. electro- and magnetostriction and piezoelectric effect) also work the other way around. That means that change of shape induces electric charge which can be later translated to current and measured. This is applied in sensors for measurement of pressure in many cavitation experiments.

[2] Dielectric material is an electric insulator that can be polarized by an application of electric field.
[3] Material is called ferromagnetic when it is magnetized by exposure to magnetic field.

3 BUBBLES NUCLEATION

Until now in the text, the threshold pressure for cavitation inception was considered to be equal to vapor pressure. Nevertheless, this assumption is often violated. Cases were reported when a liquid medium was even subjected to negative pressures, i.e. tensions [2]. This discrepancy can be better understood if the mechanisms of the nucleation of cavitation bubbles are closer studied. This will be dealt with in this chapter.

3.1 CAVITATION NUCLEI

Many experiments were carried out in past [16], [17] during which the threshold pressure value was observed. Although the results were scattered, it can be concluded that if the liquid was preliminary treated (e.g. degassed or pressurized for longer period of time) it was capable of withstanding higher tensions [18]. Moreover, experiments were carried out in which the dependency of threshold pressure on the amount of gas dissolved in liquid was observed. The value of pressure threshold was effectively reduced (even to negative values) when the gas concentration was lowered [15].

This very well supports the conclusion that micro-sized gas bubbles already present in bulk liquid serve as cavitation nuclei. They represent the points in the bulk from which phase change develops. This type of cavitation inception is referred to as **heterogeneous.** The nuclei can be either free in stream or they can be attached to walls and housed in crevices of immersed impurities. Relative importance of these forms changes with several aspects including wettability of the surface, preliminary filtration and also the length scale [19], [13], [20]. In theory, second type of cavitation can be considered as well. It supposes **homogeneous** phase change inception throughout the whole liquid volume. Nevertheless, this type is not observed in practical applications as neither liquid, nor the container walls can ever be completely deprived of gas bubbles.

The phenomenon of heterogeneous phase change can be easily observed on an example from everyday life. When one brings water near to boiling in a pot, the vapor bubbles emerge and grow either on pot walls or on objects immersed in liquid. Once the forces in bulk liquid inciting the bubble to detach exceed the force from surface tension, the bubble sets free. This moment is described by limiting value of diameter of the bubble called **departure diameter**. At the same temperature, liquids with higher surface tension have greater departure diameters [13].

3.2 NUCLEUS STABILITY WITH REGARD TO DIFFUSION

In this section the joint mechanical and diffusive equilibrium of spherical nucleus in a static liquid will be treated. This lays foundations for understanding the stability of nuclei in liquid and serves as transition towards bubble dynamics. The **mechanical equilibrium** condition was firstly considered by Blake [21]. It takes into account surface tension and supposes the pressure of the bulk liquid (denoted as p_∞) to be uniform. The resulting equilibrium condition of the two phase interface is then:

$$p_\infty = p_g + p_v - \frac{2\gamma}{R}, \tag{3.1}$$

where p_∞ – pressure of bulk liquid at infinity $[Pa]$, p_g – partial pressure of gas enclosed in the bubble $[Pa]$, p_v – vapor pressure $[Pa]$, R – bubble radius $[m]$, γ – surface tension[4] $[N \cdot m^{-1}]$.

[4] γ is used throughout the text to denote surface tension, whereas the more common notation σ is reserved for cavitation number.

Before proceeding to the second part of the Blake's equilibrium, recall that gas is present in liquid in two forms. Either it is dissolved and forms homogeneous medium with the bulk or it is trapped in nuclei. Between these two forms the mass is continuously exchanged. The **diffusion equilibrium** can be expressed in terms of concentration of gas at saturation C_s $[kg \cdot m^{-3}]$ by following equation:

$$C_s = H \cdot p_g, \tag{3.2}$$

where H – Henry's constant $[s^2 \cdot m^{-2}]$.
Two main situations can occur [2]:

- The concentration far from the nucleus is smaller than C_s. The gas then migrates from nucleus and its radius decreases. It results in the increase of surface tension term in the equation of mechanical equilibrium. This decrease is for constant p_∞ made up by increase of p_g which augments the diffusive imbalance and the nucleus is resorbed.
- The concentration far from the nucleus is larger than C_s. This leads to the exact opposite and the nucleus size grows.

It can be concluded that considered joint mechanical-diffusive equilibrium is unstable. The nucleus either vanishes or it grows until it eventually transforms into bubble. However, we all know that water does not start to boil homogeneously. It must contain nuclei and they must exist for lifetimes that are longer than this result suggests [2]. The most plausible explanation is of small crevices in solid walls or in solid particles carried by the flow. These crevices can shelter stable nuclei [22]. If the contact angle is lower than $\pi/2 + \vartheta$ for a conical crevice with apex angle 2ϑ, the curvature of the interface is negative and the surface tension term in mechanical equilibrium condition changes sign. In consequence both R and p_g decrease until reaching an equilibrium. It is interesting to note at this point that if the contact angle was π, i.e. 180°, the surface would be completely wetted and it would allow for improved degassing. Surface providing fur such an angle would be called completely hydrophobic.

Regarding the nucleus growth, one more case is of interest and will be briefly discussed. It is a nucleus being exposed to pressure oscillations (e.g. induced by ultrasound) resulting in its changing size. This phenomenon was studied by Hsieh and Plesset [23] and is generally referred to as **rectified diffusion**. Imagine the nucleus at diffusive equilibrium at time $t = 0$. During the first half period of growth the internal pressure of nucleus lowers and the gas migrates from the surrounding liquid into it. During the second half period, the external pressure rises, the nucleus becomes smaller and loses some of the gas gained in the first phase. However, the nucleus is larger and therefore has bigger surface area in the first part of the cycle and there is a net flux of gas into the nucleus. It remains relatively small, resulting in slow and stable growth of nucleus over many periods of pressure variations. Once the volume of the enclosed gas and vapor increases to such an extent that the natural frequency of the nucleus is equal to the frequency of ultrasound, the bubble rapidly increases in size and then immediately collapses. This is then cavitation inception for single bubble scenario.

Up until now a single nucleus was considered. Contrary to this simplification, every liquid contains many nuclei of various sizes [2]. All nuclei grow owing to rectified diffusion but the bigger ones reach the critical sizes earlier and transform to collapsing bubbles before the other nuclei have chance to do so. This collapse causes a pressure wave that superposes on initial pressure oscillations and these higher pressure amplitudes in turn incite further bubbles to collapse. Eventually a chain reaction develops and we may observe a collapsing cloud of bubbles.

4 THE DYNAMICS OF SPHERICAL BUBBLES

Having described the main features of cavitation nucleus, we are now concerned with the dynamics of bubble growing from it. In simplified scenario, it can be modelled by a spherical bubble with fixed center that undergoes pressure variations at infinity. We employ this model to study bubble collapse as well as its oscillations.

To make the calculations more straightforward, several additional assumptions are taken into account. Namely the following:

- The considered liquid is incompressible and either Newtonian[5] or inviscid[6]
- Gravity is neglected
- The mass exchange via diffusion is neglected
- The bubble is saturated with vapor at pressure p_v.

4.1 BOUNDARY AND INITIAL CONDITIONS

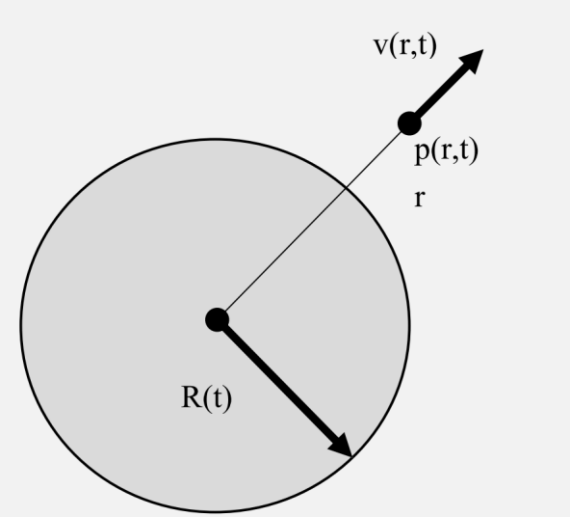

Figure 4.1: *Pressure and speed in the vicinity of the bubble*

As the mass transfer is neglected the liquid velocity at the interface $v(R,t)$ is equal to the interface velocity $\dot{R} = dr/dt$ (see Figure 4.1). For liquid with dynamic viscosity μ is the balance of normal stresses, respectively forces, on the interface (at distance $r = R$) at time t written as following:

$$p(R,t) - 2\mu\left(\frac{\partial v}{\partial r}\right)_{r=R} = p_v + p_g(t) - \frac{2\gamma}{R}, \tag{4.1}$$

where $p(R,t)$ – pressure on the cavity interface $[Pa]$, $2\mu\left(\frac{\partial v}{\partial r}\right)_{r=R}$ – radial stress due to viscosity[7] $[Pa]$.

On the left-hand side of the equation there is the normal stress at the interface. It is equilibrated on the right-hand side by the sum of gas and vapor pressures inside the bubble reduced by the effect of surface tension.

For polytropic gas transformation it holds that:

$$\frac{p_g(t)}{p_{g0}} = \left(\frac{V_0}{V(t)}\right)^{3n}, \tag{4.2}$$

[5] For in-plane flow in Newtonian fluids [1] holds: $\tau = \mu(dv/dy)$ where τ – shear stress $[Pa]$, μ – dynamic viscosity $[Pa \cdot s]$, (dv/dy) – velocity gradient. Water is Newtonian fluid.

[6] Inviscid fluid refers to a fluid flowing in a region where net viscous forces are negligible compared to pressure and inertial forces. Irrotational flow is an example used later in the text. The fluid, however, has a nonzero viscosity.

[7] More precisely it is a τ_{rr} component of symmetric viscous stress tensor $\boldsymbol{\tau_{ij}}$, where $i,j = r,\vartheta,\varphi$ are spherical coordinates.

where V_0 – initial bubble volume $[m^3]$, p_{g0} – initial partial gas pressure $[Pa]$, $p_g(t)$ – pressure at time t $[Pa]$, $V(t)$ – volume at time t $[m^3]$ and n – polytropic index $[-]$.
For isothermal expansion is $n = 1$. For adiabatic expansion is n given as ratio of gas specific heats c_{gp} and c_{gv}. For **nuclei** can be the transformation considered **isothermal**, whereas for **explosively growing** and especially **collapsing** bubble, the **adiabatic** coefficient $\varkappa$ should be used. For cavitation in aqueous liquids, the value of $\varkappa = 1.67$ corresponding to argon is usually used [24] [25].

The equation (4.2) can be further simplified:

$$p_g(t) = p_{g0}\left(\frac{R_0}{R(t)}\right)^{3n}, \tag{4.3}$$

R_0 - initial bubble radius [m].
This yields expression for pressure at the cavity interface:

$$p(R,t) = p_v + p_{g0}\left(\frac{R_0}{R}\right)^{3n} - \frac{2\gamma}{R} + 2\mu\left(\frac{\partial v}{\partial r}\right)_{r=R}. \tag{4.4}$$

The value of pressure at infinity $p(\infty, t)$ is given and denoted as $p_\infty(t)$, while the velocity of liquid at infinity is assumed to be zero, i.e. $v(\infty, t) = 0$.

At time $t = 0$ the bubble is in equilibrium and therefore the interface velocity $\dot{R}(0)$ is equal to 0. This ensures that the mechanical equilibrium of spherical bubble is satisfied and we verify this in rewriting the equation (4.4) to obtain:

$$p_{\infty 0} = p_{g0} + p_v - \frac{2\gamma}{R_0}, \tag{4.5}$$

which is the same result as equation (3.1).

4.2 RAYLEIGH-PLESSET EQUATION

The liquid is assumed incompressible[8], which means that the net flux through any spherical surface with the same centre is equal. If $v(r,t)$ is the liquid velocity at distance r from the bubble centre this condition can be written as:

$$\dot{m} = Av\rho_0 = const, \tag{4.6}$$

$$4\pi r^2 v\rho_0 dt = 4\pi R^2 \dot{R}\rho_0 dt, \tag{4.7}$$

where $\dot{m}$ – mass flow rate $[kg \cdot s^{-1}]$, A – spherical surface area $[m^2]$, ρ_0 – fluid density $[kg \cdot m^{-3}]$.
This is the **continuity equation**.

This equation can be simplified and following expression for $v(r,t)$ is obtained:

$$v(r,t) = \dot{R}\frac{R^2}{r^2}. \tag{4.8}$$

The flow is symmetric and irrotational. This allows us to write [1]:

$$\nabla^2 \cdot \vec{v} = 0, \tag{4.9}$$

where $\nabla = \left(\frac{\partial}{\partial x}, \frac{\partial}{\partial y}, \frac{\partial}{\partial z}\right)$ – vector differential operator nabla and $\nabla^2 = \nabla \cdot \nabla = \frac{\partial^2}{\partial x^2} + \frac{\partial^2}{\partial y^2} + \frac{\partial^2}{\partial z^2}$ is Laplacian operator.

[8] Having constant density ρ_0, in three dimensions this means $\nabla \cdot \vec{v} = 0$. This assumption holds for velocities lower than 0.3 of the speed of sound in given medium at given temperature [1].

The viscous term of Navier-Stokes equation[9] therefore vanishes and it subsequently becomes **Euler equation** and can be written as:

$$\frac{\partial v}{\partial t} + v\frac{\partial v}{\partial r} = -\frac{1}{\rho}\frac{\partial p}{\partial r}, \tag{4.10}$$

where $\frac{\partial v}{\partial t}$ – local acceleration caused by inertial forces $[m \cdot s^{-2}]$, $v\frac{\partial v}{\partial r}$ – convective acceleration caused by inertial forces $[m \cdot s^{-2}]$, $\frac{1}{\rho}\frac{\partial p}{\partial r}$ – acceleration from surface forces $[ms^{-2}]$.

If the expression for velocity (4.8) is substituted, the equation takes the following form:

$$\ddot{R}\frac{R^2}{r^2} + 2\dot{R}^2\left[\frac{R}{r^2} - \frac{R^4}{r^5}\right] = -\frac{1}{\rho}\frac{\partial p}{\partial r}, \tag{4.11}$$

$\ddot{R}$ – acceleration at the bubble interface $[m \cdot s^{-2}]$.

This equation can be now integrated with respect to r, while considering the conditions at infinity:

$$\frac{p(r,t) - p_\infty(t)}{\rho} = \ddot{R}\frac{R^2}{r} + 2\dot{R}\left[\frac{R}{r} - \frac{R^4}{4r^4}\right]. \tag{4.12}$$

On the interface $r = R$ and therefore:

$$\frac{p(R,t) - p_\infty(t)}{\rho} = R\ddot{R} + \frac{3}{2}\dot{R}^2. \tag{4.13}$$

We differentiate equation (4.8) and substitute for r to get:

$$\left(\frac{\partial v}{\partial r}\right)_{r=R} = -2\frac{\dot{R}}{R}. \tag{4.14}$$

Now the equation (4.1) can be written as:

$$\left[R\ddot{R} + \frac{3}{2}\dot{R}^2\right]\rho = [p_v - p_\infty(t)] + p_{g0}\left[\frac{R_0}{R}\right]^{3n} - \frac{2\gamma}{R} - 4\mu\frac{\dot{R}}{R}. \tag{4.15}$$

This equation allows for analysis of evolution of radius R and consequently the pressure field in the liquid. It is known as **Rayleigh-Plesset equation**. The term on the left-hand side accounts for variation in kinetic energy of the liquid body [15]. This becomes more clear when we divide this term by density obtaining a physical dimension of energy per unit of mass $m^2 \cdot s^2$, i.e. Jkg^{-1}.

The first term on the right-hand side, namely $p_v - p_\infty(t)$, measures the difference between applied pressure and vapor pressure. It is the most important term, because the bubble size evolution will depend mainly on it [26]. The second term on the right-hand side represents the contribution of non-condensable gas. As the diffusion is by assumption neglected, the mass of gas enclosed in the bubble remains constant. The third term is the contribution of surface tension. As the radius R appears in denominator its importance increases with decreasing radius. The last term on the right-hand side represents dissipation due the effect of dynamic viscosity of the liquid. R again appears in denominator, hence, it is significant mainly for small radii [26].

[9] In general form in 3D space when omitting body forces this is:

$$\rho\frac{\partial \vec{v}}{\partial t} + \rho\vec{v}\cdot\nabla\vec{v} = -\nabla p + \mu\nabla^2\vec{v},$$

where the last term on the right-hand side is the viscous term.

4.3 BUBBLE EQUILIBRIUM

Rayleigh-Plesset equation can be conveniently exploited to study bubble static equilibrium. In this case all time derivatives become zero and the polytropic index becomes isothermal, i.e. $n = 1$. The pressure far from the bubble p_∞ is assumed constant. The resulting equation is:

$$p_\infty = p_{g0}\left[\frac{R_0}{R}\right]^3 + p_v - \frac{2\gamma}{R}. \tag{4.16}$$

The reciprocal relationship of p_∞ and R is plotted in Figure 4.2. The equilibrium curve exhibits a clear minimum. To find it, it is sufficient to take a derivative with respect to R and set it equal to zero, which yields:

$$R_c = \sqrt{\frac{3p_{g0}R_0^3}{2\gamma}}. \tag{4.17}$$

After substituting back to the former equation we get the corresponding value of pressure [26]:

$$p_c = p_v - \frac{4\gamma}{3R_c}. \tag{4.18}$$

The subscript c stands for critical.

Three particular cases will be now briefly analyzed. Case 1 (as shown in Figure 4.2) represents a **stable** behavior because after a theoretical sudden reduction of pressure the bubble will reach position on the curve with a respective higher but finite radius.

The other two cases represent an **unstable** behavior. In the case 2 the magnitude of the pressure drop has to be high enough to avoid reaching a new equilibrium, whereas in the case 3 any pressure reduction leads to further destabilization of the bubble size.

The left branch of the curve is therefore stable while the right branch is unstable. Subsequently, the value of critical pressure p_c then can be considered as threshold value beyond which microbubbles explode to macroscopic dimensions. It is also apparent that the value of critical pressure is lower than the vapor pressure. The difference is mainly due to the surface tension [2].

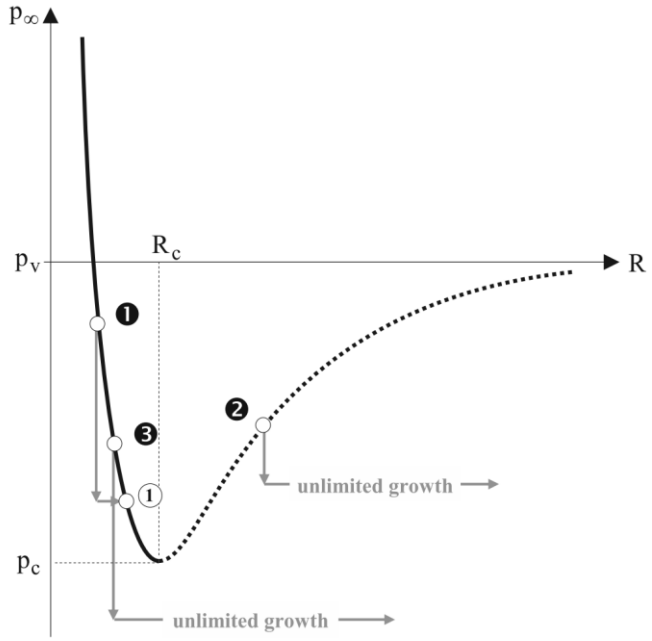

Figure 4.2: *Mutual dependency of bubble radius and pressure at infinity [26]*

In ordinary water that has not been preliminary treated, one finds wide distribution of bubble sizes. From what was concluded in previous paragraph, namely that the reduction of critical pressure is due to surface tension term with radius in denominator, it can be inferred that larger nuclei have higher vapor pressures and therefore cavitate first. The critical pressure of the largest nucleus is called the **susceptibility pressure of liquid**.

The critical value of pressure p_c is the lowest value the nucleus can withstand under stable conditions. The difference $p_v - p_c$ is called **static delay**. Rewriting the equation (4.18), it can be expressed as follows:

$$p_v - p_c = \frac{4\gamma}{3R_c}. \tag{4.19}$$

From the above equation it is clear that the difference between vapor pressure and the actual threshold for phase change is influenced by surface tension term and becomes increasingly important for small radii, i.e. at microscale. Moreover, it was observed that for short bubble residency times in low pressure region the delay increases [14]. Both these effects help us to understand why cavitation inception happens at such low cavitation numbers during experiments in microscale domains.

4.4 BUBBLE AS A LINEAR OSCILLATOR

The dynamics of bubble under effect of oscillating pressure are of great concern as this presents very frequently applied method of inducing cavitation. First, the effect of only small oscillations will be considered.

The pressure field far from the bubble at time t can be described by following equation:

$$p_\infty(t) = p_{\infty 0}(1 + \varepsilon \sin(\omega t)), \tag{4.20}$$

where $p_\infty(t)$ – oscillating pressure far from the bubble $[Pa]$, ε – ratio of amplitude of oscillations to value of static pressure $[-]$, ω – angular frequency $[rad \cdot s^{-1}]$.

Where ε is assumed significantly smaller than 1. For the radius oscillations it then holds:

$$R(t) = R_0[1 + \delta(t)], \tag{4.21}$$

$$\delta(t) = \frac{R(t) - R_0}{R_0}, \tag{4.22}$$

$\delta(t)$ – relative radius change $[-]$.

Small pressure oscillations are assumed and the value of δ therefore remains small. This allows for Rayleigh-Plesset equation to be linearized in following manner [26], [15]:

$$\rho R_0^2 \ddot{\delta} + 4\mu\dot{\delta} + \left(3np_{g0} - \frac{2\gamma}{R_0}\right)\delta \cong -p_{\infty 0}\varepsilon \sin(\omega t). \tag{4.23}$$

As this is an equation of harmonic oscillator, then the natural frequency f_0 $[Hz]$ is given as $\omega_0/2\pi$ or:

$$f_0 = \frac{1}{2\pi R_0}\sqrt{\frac{1}{\rho}\left(3np_{g0} - \frac{2\gamma}{R_0}\right)}. \tag{4.24}$$

If we now substitute equation (4.5) into equation (4.24) we obtain expression for angular frequency:

$${\omega_0}^2 = (2\pi f_0)^2 = \frac{1}{\rho {R_0}^2}\left[3n\left(p_{\infty 0} + \frac{2\gamma}{R_0} - p_v\right) - \frac{2\gamma}{R_0}\right]. \tag{4.25}$$

The resulting bubble natural frequency for various radii for $n = 4/3$ is shown in Figure 4.3.

If the viscous term in equation (4.23) is omitted and we consider initial conditions at $t = 0$ to be $R = 0$ and thus $\dot{R} = 0$, two results for $R(t)$ can be obtained. First case is if $\omega = \omega_0$, i.e. the case when the frequency of oscillating field is the same as the natural frequency of the bubble. The bubble will oscillate with linearly increasing amplitude. This evolution is unstable [15]. In the second case when $\omega \neq \omega_0$ we get for $R(t)$ the following expression [15]:

$$R(t) = \frac{-p_{\infty 0}\varepsilon}{\rho R_0(\omega_0^2 - \omega^2)}\left(\sin(\omega t) + \frac{\omega}{\omega_0}\sin(\omega_0 t)\right). \tag{4.26}$$

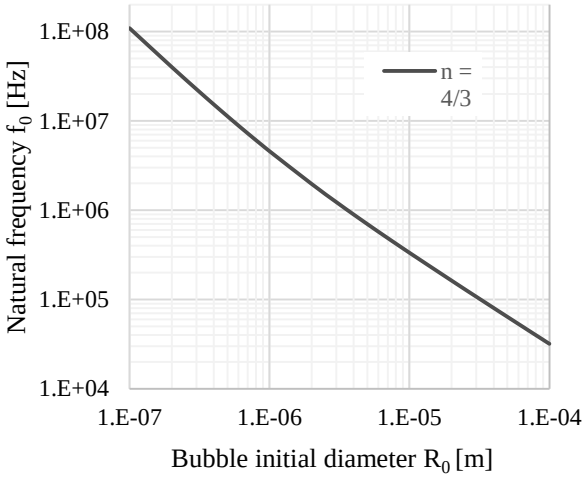

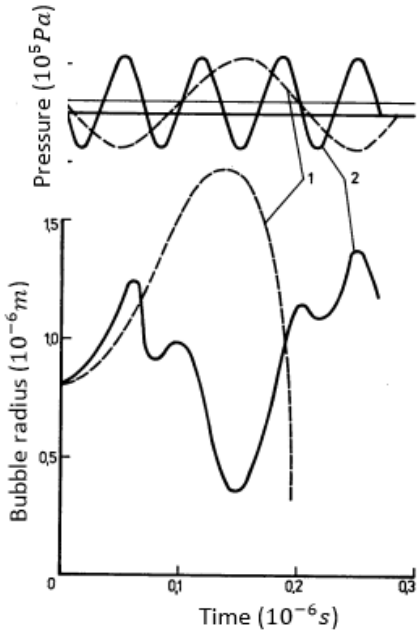

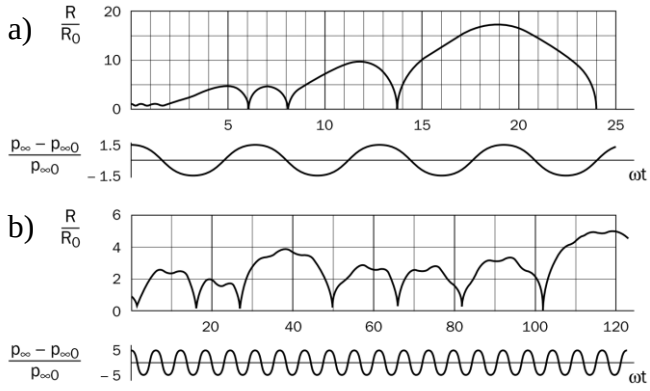

***Figure 4.3**: Upper left: Bubble natural frequency versus its diameter. The values are plotted in logarithmic scales, values used for computation are:* $\rho = 998.3\ kg \cdot m^{-3}, \gamma = 0.072\ N \cdot m^{-1}, p_v = 2339\ Pa, p_{\infty 0} = 101.325\ kPa$

***Figure 4.4:** Upper right: Bubble radius as function of far field pressure for* $p_{\infty 0}\varepsilon = 4 \cdot 10^5\ Pa, R_0 = 0.8 \cdot 10^{-6}\ m$. *Curve **1** -* $\omega = 3 \cdot 10^7\ s^{-1}$, *curve **2** -* $\omega = 9 \cdot 10^7\ s^{-1}$ *[28]*

***Figure 4.5**: Left: Two examples of gas bubble radius oscillations due to pressure field described by equation (4.20) [29]*

The solution composes of two parts, one is due to natural (ω_0) and the second due to forced (ω) oscillations. These two parts are added up and result in oscillations with period T_t. More precisely it can be written:

$$\omega T_t = 2\pi s, \qquad \omega_0 T_t = 2\pi m, \tag{4.27}$$

s, m – integers.

After substituting for $\omega = 2\pi/T$, $\omega_0 = 2\pi/T_0$ and $\omega_t = 2\pi/T_t$ we can write:

$$\begin{aligned} T_t &= sT = mT_0, \\ \omega &= s\omega_t, \qquad \omega_0 = m\omega_t, \end{aligned} \tag{4.28}$$

ω_t – angular frequency of resulting oscillations $[rad \cdot s^{-1}]$.

From last two equations it is apparent that if $\omega/\omega_0 = s/m$ is rational number the resulting oscillations will be periodic.

The numerical solution of linearized Rayleigh-Plesset equation (4.23) was carried out for example by Flynn [27]. His results show that for small values of ε are the bubble oscillations stable.

4.5 NON-LINEAR OSCILLATIONS OF A BUBBLE

As the Rayleigh-Plesset equation is nonlinear the results discussed in previous chapter are not generally valid. For example if the bubble of natural frequency f_0 is exposed to oscillating pressure field with $f = f_0$ the energy will be transferred to the bubble and its average radius

will increase, resulting in decrease of its natural frequency [30].The new natural frequency will be $f_o' = \omega_0'/2\pi$. With increasing oscillations amplitude f_0' decreases. Only for small values of ε is the difference between f_o' and f_0 small.

The response of bubble radius change with respect to angular frequency of applied pressure field oscillations is illustrated in Figure 4.4, where in case 1 is the angular frequency of applied pressure oscillations smaller then natural frequency of the bubble and in case 2 is the angular frequency of applied pressure oscillations greater than the bubble natural frequency.

If the assumption of small ratio ε is violated the response of a bubble to such pressure variations tends to be non-linear. Often it is non-periodic or it exhibits subharmonic frequencies. This is shown in Figure 4.5 where in case a) $\varepsilon = 1.5$ and $\omega/\omega_0 = 0.0154$ and in case b) $\varepsilon = 5$ and $\omega/\omega_0 = 1.54$.

Periodic solutions to equation (4.15) were classified among others by Stoker [31]. The bubble oscillations compose of:

1. Subharmonic component, if $m = 1$ and $s > 1$, i.e. if $\omega_0' = \omega_t$ and $\omega_0' = \omega/s$,
2. Harmonic component, if $s = 1$ and $m > 1$, i.e. $\omega = \omega_t$ and $\omega_0' = m\omega$,
3. Ultraharmonic component, if m and s are integers higher than 1, then $\omega_0' = m\omega_t$ and $\omega = s\omega_t = (s/m)\omega_0'$,

where s, m are integers.

The subharmonic component was experimentally confirmed by Negishi [32].

5 CAVITATION CHEMISTRY

If the collapse of a cavitation bubble in liquid medium is theoretically analyzed [15], one finds that the interface velocity of collapsing bubble resulting from Rayleigh-Plesset equation may reach values of the order of the velocity of sound in water. Similarly the values of pressure in the collapsing bubble are calculated as high as over $100\ MPa$. The temperatures obtained from full Rayleigh-Plesset model [25] exceed $10\ 000\ °C$.

These values are, of course, only theoretical, as the equation ignores several important aspects. Namely the compressibility of the fluid, presence of non-condensable gas in the bubble, finite rate of vapor condensation, presence of surrounding bubbles or the fact that collapsing bubble tends to lose its spherical shape and splits into several smaller bubbles [15]. All these factors will cause the real values to be below the theoretical ones. For example the pressure during a bubble collapse induced by ultrasound is estimated to be several tens of MPa [33]. Likewise, the temperature in this case is estimated around several thousand °C [34], [35]. Nevertheless, it can be concluded that the conditions in collapsing bubble are extreme. They are suitable to initiation of endothermic chemical reactions.

5.1 REACTIONS IN COLLAPSING BUBBLE

A bubble pulsating in water containing dissolved air is thought to contain mainly argon. Other gases, i.e. N_2, O_2 and H_2O that diffuse into bubble should burn off during compression phase [36]. The initial products of chemical reactions inside bubble are $OH^\bullet$ and nitrogen oxides (NO_x). The radical[10] is product of homolytic cleavage (homolysis) of water and eventually forms H_2O_2, as shown consecutively [37]:

$$H_2O \rightarrow H^\bullet + OH^\bullet$$
$$O_2 \rightarrow 2\,O^\bullet$$
$$H^\bullet + H_2O \rightarrow OH^\bullet + H_2$$
$$O^\bullet + H_2O \rightarrow 2OH^\bullet$$
$$H^\bullet + O_2 \rightarrow HOO^\bullet$$
$$2OH^\bullet \rightarrow H_2O_2$$
$$2HOO^\bullet \rightarrow H_2O_2 + O_2.$$

Not all $OH^\bullet$ radicals are consumed in this process however. Some of them oxidize organic compounds in the liquid which can be exploited in practical applications. NO_x reacts with water producing nitrite and nitrate ions [38].

Suslick and Didenko [24] quantitatively studied radical production due to acoustically induced single bubble collapse in water. They concluded that potential energy possessed by a single bubble at its maximum size represents upper energetic limit for formation of radicals. Most of this energy is converted into mechanical form (e.g. interface wall motion and shock waves propagating into the bulk liquid) or into heat. The latter is due to the fact that although radical species are formed in the bubble, most of them will again exothermically recombine [39]. They estimated that only about 10^{-4} of potential energy of the bubble gets consumed in endothermic creation of radicals and ions that escape the collapsing bubble.

5.2 CHEMISTRY CAUSED BY HYDRODYNAMIC CAVITATION

The chemistry induced by acoustic cavitation has been quite well studied [38], [40], [41], [42]. This owes not only to the fact that acoustic cavitation is easier to harness but also to the predominant opinion that acoustic cavitation is more energy-efficient process for radical

[10] Radical, also called free radical, is an atom or group of atoms containing one or more unpaired electrons. They tend to have shorter lifetimes compared to ions and are highly reactive. [91]

transformation [38], [43]. In contrast, hydrodynamically induced chemistry has been investigated only scarcely. Some authors claim it to have higher energy efficiency [11].

One of the first researchers who investigated chemistry induced by HC was *Suslick et al*. [38]. He carried out experiments with solution of KI in water saturated with carbon tetrachloride. Addition of CCl_4 increases the radical production. $Cl^{\bullet}$and Cl_2 are created resulting in higher rates of iodide oxidation. This is a standard procedure employed also in more recent experiments [25]. He concluded that from the onset of cavitation on is the rate of triiodide formation linearly depended on upstream **pressure**. This is shown in Figure 5.1. The threshold value of 150 bar represents the cavitation inception limit.

He further examined the relationship between I_3^- formation rate and the **thermal conductivity** of dissolved gas. The resulting graph is plotted in Figure 5.2. The reason for exponential decrease is best explained by hot-spot model suggesting that the maximum temperature realized in collapsing bubble is decreasing linearly with increasing thermal conductivity of enclosed gas [44]. This relation, with assumption of Arrhenius[11] behavior, leads to an exponential decrease in the triiodide formation rate with increasing thermal conductivity.

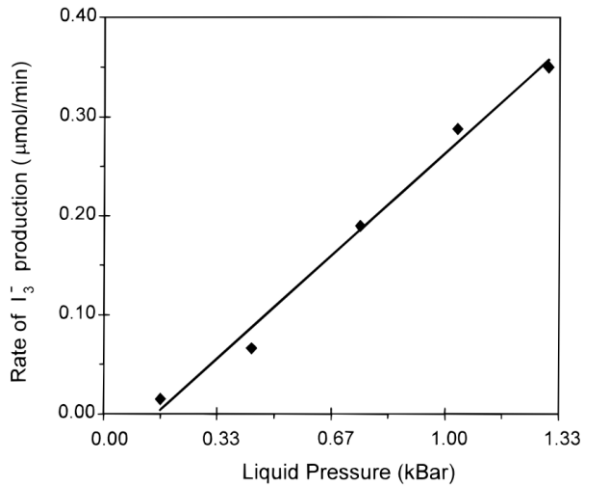

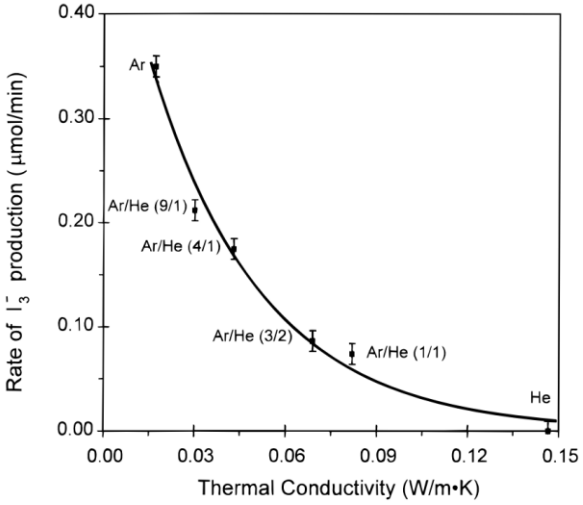

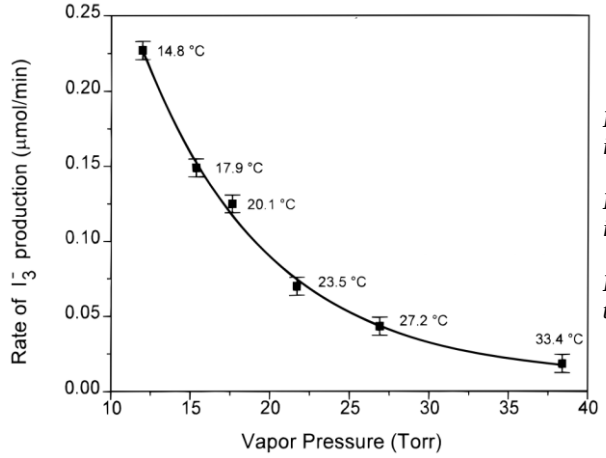

Figure 5.1: *Upper left: Rate of triiodide formation with increasing pressure [38], 1 bar = 100 kPa*

Figure 5.2: *Upper right: Rate of triiodide formation with increasing thermal conductivity [38]*

Figure 5.3: *Left: Rate of triiodide production with increasing temperature [38], 1 Torr =133.322 Pa*

[11] Arrhenius behavior implies dependence of rate constants on temperature. Over a limited range it is represented by following empirical equation: $k = A \cdot \exp\left(\frac{-E_a}{R_m T}\right)$, where k – rate constant $[s^{-1}]$, A – pre-exponential factor $[s^{-1}]$, E_a – activation energy $[J \cdot mol^{-1}]$, $R_m = 8.314\, J \cdot K^{-1} \cdot mol^{-1}$ – universal gas constant and T – temperature $[K]$ [91].

Yet another result is summed in Figure 5.3. It shows the influence of bulk liquid **temperature** and **vapor pressure** on the rate of triiodide production. The ion production decreases steeply with both increasing pressure and increasing temperature. This is probably due to decrease of polytropic ratio n induced by increase of polyatomic vapor inside the bubble. This effectively dampens the collapse [45]. The same behavior was observed for acoustic cavitation [46], [47], [45].

5.3 MICROSCALE CAVITATION CHEMISTRY

Only very recently has been the cavitation studied from chemical viewpoint also at microscale by Tandiono *et al.* [48]. They observed that formed bubbles have rather pancake shape instead of spherical one. As already mentioned, violation of spherical symmetry alleviates the conditions reached during collapse phase. Also the viscous term (see equation 4.15) becomes increasingly important at microscale, slowing down the size evolution of bubbles. Moreover, the small volume of surrounding liquid results in lesser amount of generated bubbles and provides only limited inertia needed for gas compression. On the other hand, smaller number of generated bubbles reduces bubble-to-bubble interaction and presents good conditions for studies of bubble dynamics on induced chemistry.

Despite the limiting factors the authors managed to produce cavitation acoustically in a microfluidic channel fabricated from polydimethylsiloxane (PDMS). The bubbles were generated from gas-liquid interfaces achieved thanks to gas injection. The chemical reactions due to acoustic effects (**sonochemistry**) and light emission caused by ignition of gas in collapsing bubble (**sonoluminiscence**) were measured optically.[12] Production of $OH^{\bullet}$ and $H^{\bullet}$ radicals was confirmed. In comparison to experiments conducted at macroscale [49] the reaction stops much faster (by several orders of magnitude) once the ultrasound source is turned off. Authors suppose that it owes to small volumes leading to faster diffusion rates.

[12] Another method employed in observation of radical formation. It is based on oxidation of luminol by free radicals. This reaction produces observable light emissions [92].

6 APPLICATIONS OF CAVITATION

Cavitation has been intensively studied since 1950s [13]. At first, it was regarded only as detrimental to hydraulic machines. The main purpose was to avoid it. However, in recent decades many possible useful process have been designed and put into practice where the cavitation is beneficial [15], [37], [50], [51], [52]. More focus was devoted to acoustic cavitation as it is easier to control. It is also mostly regarded as more energy efficient [43]. Few researches, on the other hand, claim the hydrodynamic cavitation to be more efficient than acoustic one. This cannot be completely ruled out, at least in some applications, as the hydrodynamic process requires careful parameter optimization and is yet to be thoroughly investigated. In any case it offers an alternative in conditions when it is not suitable to produce the cavitation by application of ultrasound. It appears more convenient when large volume of liquid is to be treated [7].

The effects of cavitation that can be exploited to achieve various means are generation of hot spots, reactive free radicals and new surfaces, furthermore, turbulence is generated as a result of liquid circulating currents [53], [54]. All this can lead to intensification of physical and chemical processes.

6.1 HYDRODYNAMIC CAVITATION APPLICATIONS

6.1.1 FOOD STERILIZATION

This method exploits high physical stresses created in liquid by collapsing bubbles. These stresses are thought to induce cellular inactivation. *Milly et al.* [55] investigated the application of hydrodynamic cavitation for sterilization of juices and milk and reported adequate destructive forces to inactivate yeast, yeast acrospores and bacterial spores. It seems advantageous to use conventional high temperature methods along with cavitation to be able to achieve same sterilization results at lower process temperature which in turn will result in superior quality products [7].

Another method of food sterilization has been recently proposed [56]. It necessitates introduction of steam into the liquid which subsequently causes cavitation. The coupled effect of heat and mechanical stresses could be used to sterilize beverages. *Mahulkar et al.* [57] have found it to be more efficient compared to traditional hydrodynamic cavitation production methods. They also numerically and experimentally showed that the produced collapse conditions were similar to hydrodynamic cavitation.

6.1.2 MICROBIAL CELL DISRUPTION

The need for an efficient microbial cell disruption method is considered as limiting to fabrication of commercial products based on intracellular derivatives [58]. Presently employed methods work with efficiency below 10 % and dissipated heat must be continuously removed to avoid damage to cellular enzymes [59].

Hydrodynamic cavitation has been shown to cause no alteration in activity of released enzymes, effectively removing the need for cooling [60]. It also caused less damage to microbial cells compared to acoustic cavitation (authors of the paper admit that this may be due to non-optimized chosen value of ultrasound frequency). Consecutively, the cell can be disrupted only partially, releasing only periplasmic enzymes while the cytoplasmic ones remain concentrated inside. This offers not only advantage in terms of targeted enzyme yield but also requires lower mechanical stresses applied to the cell, hence less energy [61]. If the enzyme is initially cytoplasmic, the cells can be preliminary treated to translocate the enzyme into periplasmic

region. Various reported methods of translocation include heat stress, time of culture in the fermentation process, variable pH operation and chemical pre-treatment [62], [63].

6.1.3 WATER DISINFECTION

Contaminated water can be processed in different ways. One of them uses Advanced Oxidation Process (AOP) where contaminants are oxidized and therefore destroyed by intermediate radicals formed in the liquid [64]. $OH^{\bullet}$ represents an appropriate radical species to achieve oxidation as it possesses relatively large oxidation potential (2.77 V, which is for example twice the value Cl_2 has).

The oxidizing effect of radicals created within collapsing bubble during cavitation was described in Chapter 5. This process can be exploited to oxidize organic compounds in contaminated water and thus achieve its disinfection. Hydrodynamic cavitation used for this purpose was recently investigated by several researchers [43], [65]. *Jgoti & Pandit* [66] found it to be more economical than cavitation induced by sonochemical reactors (i.e. acoustic cavitation) but more expensive compared to traditional chemical processes (e.g. ozonation or chlorination). They propose that hydrodynamic cavitation could become more economically convenient on larger scale or in cases when byproducts of chemical treatment in disinfected liquid are to be avoided. Future application of joint effects of chemical and hydrodynamic treatment is also interesting as it would increase the mass transfer rate and consequently the rate of chemical reactions.

6.1.4 CYANOBACTERIAL BLOOM REMOVAL

Jancula et al. [67] recently investigated use of HC for cyanobacterial bloom removal. They offer an alternative to more conventional chemical treatment. Although chemical method is relatively cheap and fast, it has its drawbacks. Namely the facts that used agents are often toxic to not-target species and they tend to persist in the environment for long periods of time even after the treatment is over [67].

Hydrodynamic treatment induces intracellular cavitation in cyanobacteria. Their gas vesicles, used as vertical positioning mechanism, serve as cavitation nuclei. Authors of the paper reported gas vesicle destruction of 99 % of observed cyanobacteria in given sample for 18 HC cycles. At the same time they reported no damage to their cell membrane. This is of great importance because cyanobacteria are producers of toxins harmful to range of organisms including humans [68], [69]. If the membrane is not porated[13], the toxins remain safely enclosed in it.

6.2 NOTE ON ACOUSTIC CAVITATION APPLICATIONS

All processes outlined in chapter 6.1 can be carried out using ultrasound to produce cavitation as well. As mentioned in the introduction to this chapter, acoustic cavitation is more widely understood as beneficial for utilization in processes. This resulted in multitude of its applications which description is largely out of the scope of this thesis. Only selected applications of microscale AC will be dealt with in chapter 7. Reader interested in conventional scale AC is advised to consult literature published on the topic [37], [15].

Nevertheless, one application will be dealt with separately. There are two reasons for this: first, no information on cavitation induced hydrodynamically in this case was found and second, it is likely to be scaled to microchannel dimensions for future targeted drug delivery applications.

[13] Poration is a term used to describe damage done to cell membrane resulting in its partial opening.

It is termed **sonoporation** and resembles the process already described in chapter on microbial cell disruption (6.1.2). It was presented in paper published by *Ohl et al.* [70].

The authors used US shock wave (single intensive pulse) to excite bubble growth and subsequent collapse in near-wall regions. The walls were populated with cervix cancer cells. Membrane poration through series of events was reported. First, the bubbles became nucleated and grew explosively. Then they collapsed, losing its spherical symmetry and developing liquid jet towards the wall populated with cells. Then the jet impacted on the boundary and spread along the wall causing strong shear stress. This shear stress resulted in damage done to the attached cells. Three principal regions of damage severity were reported. At the point of the impact the cells became completely detached. Cells at the border of detached area were permanently damaged. Further away from detached area the cells were only temporarily porated. Exactly in this region it is possible to introduce comparatively large-scale molecules inside the cell. This was proved by measurement of the uptake of fluorescent chemical.

7 CAVITATION AT MICROSCALE

In recent decade, microelectromechanical systems (MEMS) research has received a lot of attention and experienced steep growth. A variety of microfluidic MEMS devices was proposed for application in multitude of not only technological fields. Examples include: microrockets [71], microcoolers [72], microrefigerators [73], micromixers [74], micro turbopumps [75], drug delivery systems [76], chemical microreactors [77], DNA synthesis and Bio-MEMS systems [78], [79].

Cavitation has also been already observed in biological fluids [80] which can possibly threaten functionality of Bio-MEMS devices containing microvalves and micropumps, e.g. Lab-on-Chip devices. Last but not least, it has been shown that by miniaturization of sonochemical reactors one can study complex phenomena, such as microbubble creation, to improve their operation efficiency [81]. Similar results could be achieved by scaling down HC.

Although the cavitation has been rather extensively studied since 1950s, in micro domains it remains largely untapped topic. Question arises whether the results obtained on conventional scale can be applied to channels with micrometer dimensions. Recently obtained results suggest that there are indeed some major deviations [14]. Reasons for these deviations and their consequences are discussed in following sections.

7.1 HYDRODYNAMIC CAVITATION SCALING

Decreasing the diameter of constriction was shown to decrease pressure recovery time resulting in increase of bubble collapse intensity. This in turn results in increased hot-spot temperatures and radical formation rates [82], [38]. Interestingly enough this effect seems to have its limit [25].

7.1.1 IMPORTANCE OF SURFACE NUCLEI

Mishra & Peles [14] and *Singh & Peles* [13] confirmed the hypothesis of *Holl* [20] when they found out that the importance of surface nuclei in cavitation generation significantly increases at microscale. On larger scales, stream nuclei are mainly triggering the cavitation [13]. This difference probably owes to small dimensions of microfluidic channel, stream bubbles short residency time in low pressure region, increasing importance of surface tension at small scales, but also preliminary filtration of fluid. In microfluidic experiments, $0.2\ \mu m$ and sometimes $0.1\ \mu m$ filters are applied at the microchannel inlet. This influences the stream nuclei concentration.

7.1.2 DIFFERENT GEOMETRIES AND MATERIAL

If the surface nuclei are of major importance it is quite instinctive to expect deviations from conventional scale applications where steel components are mainly used in contrast to microscale when the components are mainly micro-fabricated on silicon substrate. Likewise, previously has been the cavitation dealt with mainly in pipes and constrictions of circular diameter, whereas microfluidic components usually have rectangular cross section.

7.1.3 LOW CAVITATION NUMBER

Mishra and Peles observed that values of cavitation inception number σ_i are well below unity at microscale [14], approximately 5 times lower than values measured at conventional scales. The obtained values with respective channel geometries are presented in Table 7.1 which originally appeared in their work.

Table 7.1: *Cavitation inception and choking numbers for respective geometries. D_h, d_h – hydraulic diameter[14] of the channel and orifice respectively, w_o – orifice width, w_p – channel width, h – both channel and orifice depth. The cavitation number was evaluated using pressure port located 22 D_h downstream*

Device Description	Device No.	$\frac{d_h}{D_h}$ [−]	$\frac{A_o}{A_p} = \frac{w_o}{w_p}$ [−]	σ_i [−]	σ_{Ch} [−]
$w_o = 11.5\ \mu m$ $w_p = 100.2\ \mu m$ $h = 101.3\ \mu m$	**#1**	0.205	0.1147	0.284	0.242
$w_o = 21.5\ \mu m$ $w_p = 100.2\ \mu m$ $h = 101.3\ \mu m$	**#2**	0.352	0.2145	0.38	0.299
$w_o = 21.5\ \mu m$ $w_p = 201\ \mu m$ $h = 101.3\ \mu m$	**#3**	0.263	0.1069	0.24	0.171
$w_o = 40\ \mu m$ $w_p = 200.2\ \mu m$ $h = 101.3\ \mu m$	**#4**	0.426	0.1998	0.301	0.252

The reported values of σ_i are low again due to increased importance of surface nuclei coupled with importance of surface tension at microscale. For surface nuclei, the bubble departure diameter is mainly dictated by the surface tension force which prevents the departure and the drag force exerted on the bubble by liquid flow which, on the other hand, supports the departure. The size of bubbles remaining attached to the surface increases with increasing surface tension. This was confirmed by experiments in channels of identic geometries using both water and ethanol which has approximately three times lower surface tension than water [13]. It appears that at such small scales the surface tension term dominates over the drag force, thus resulting in bigger departure diameters, longer time and pressure difference necessitated for nuclei growth and consequently in low value of cavitation inception number.

7.1.4 CAVITATION CHOKING

The bubble departure diameter tends to be of the same or even bigger size than the microchannel hydraulic diameter. This is illustrated by Figure 7.1 and we see that bubbles grow to such dimensions that they fill constrained passages in the channel before they are carried away by the flow. This explains the values of cavitation choking number (σ_{Ch}) given Table 7.1. At larger scale the cavitation number has to be reduced significantly beyond its value at inception before cavitation choking is detected [12]. Some authors reported 59 % increase in flow rate beyond inception to cause choking [83], whereas in the microscale study presented by *Mishra & Peles* [14] in some cases only 1–2 % increase of flow rate beyond cavitation inception was sufficient to cause the flow to choke. One can conclude that at microscale the cavitation readily changes its form from inception to choking. For completeness, it should be noted that the used term cavitation choking is employed as a synonym for **supercavitation**.

At choking, the pressure difference loses its control over volumetric flow rate Q. Any increase of pressure difference fails to produce any result in terms of higher flow through orifice, as shown in Figure 7.2, where the volume flow rate Q clearly reaches plateau. With increasing pressure difference only the extension of vapor cavities further downstream was observed. The

[14] $(hydraulic\ diameter) = \frac{4\times(cross-sectional\ area)}{(wetted\ perimeter)}\ [m]$

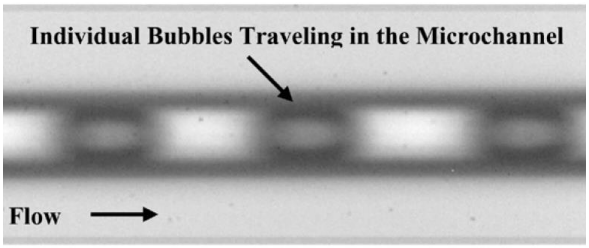

***Figure 7.1**: Up: Bubbles completely filling the cross-section of a microchannel [14]*

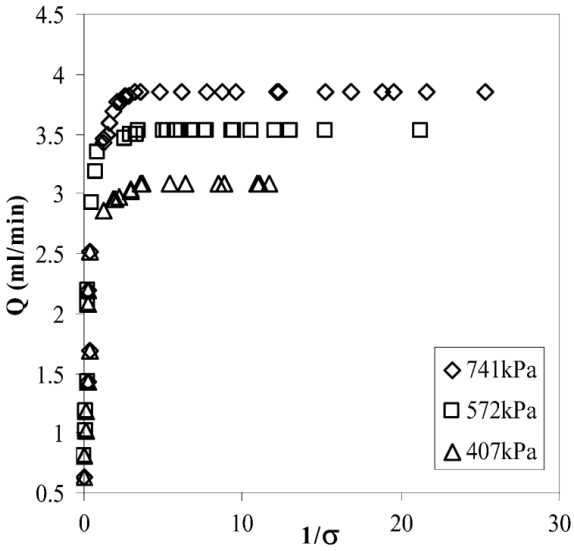

***Figure 7.2**: Right: Volumetric flow as function of cavitation number for different values of inlet pressure. The data correspond to device #2 from Table 7.1. The outlet pressure was lowered even below atmospheric [14]*

inlet pressure remained constant for each dataset as the researchers controlled the cavitation number by lowering pressure at outlet (in some cases even to negative relative pressure values).

The study that is of special interest in this thesis conducted by *Rooze et al*. [25] observed rate of ion production in cavitating flow through microorifice. $100 \times 100\ \mu m^2$ rectangular micro channel with $20 \times 100\ \mu m^2$ constriction and circular $750\ \mu m$ diameter millichannel with constrictions of $100 - 300\ \mu m$ diameter were used.

The authors reported no iodide oxidation by radicals in microchannel whereas they achieved radical production in millichannel. This is probably due to different flow patterns through smaller channel resulting in almost instantaneous transition from cavitation inception to supercavitation. Almost no transient isolated bubbles were observed. *Mishra & Peles* [14] studied channel of similar geometries and showed that in rectangular microchannel the cavitation takes form of large wall-attached cavities engulfing liquid jet and stretching far downstream, in such cases they reported high void fraction and long pressure recovery region. Isolated bubbles were observable only far downstream where they were sheared off the attached cavities.

For millichannel reported Rooze *et al*. [25] the pressure recovery to take place inside the constriction (of length $500\ \mu m$). Similarly, they confirmed long pressure recovery region for microchannel.

7.2 MICROSCALE APPLICATION OF ACOUSTIC CAVITATION

The state-of-the-art research is only beginning to explore the features of hydrodynamic cavitation in microfluidics as described above and studied in further chapters. This also explains why no information on applications of HC in microfluidics was found during researching of science papers. Also the applications of AC in micro-sized domains remain scarce to the date, as it is only recently that researchers managed to produce it [84], [85].

Nevertheless, one possible use of AC, **sonolysis**, was recently reported by *Tandiono et al*. [6]. Sonolysis allows for micro-scale analysis of intracellular contents and it resembles the process already described in chapter 6.1.2 on microbial cell disruption. Cavitation is induced by effect of ultrasound in the microchannel. The resulting mechanical stresses applied to biological content cause disruption of cell membranes. The intracellular content is then released to surrounding liquid and its composition and concentration can be measured. The authors reported only short bursts of ultrasound (less than 0.4 s for Escherichia coli and about 1.0 s for yeast cells) sufficient for complete cell lysis. This prevents additional heating from energy

transmission and preserves the fragile cellular content. Also the large surface area of the microfluidic channels supports the transfer of heat away from liquid. It was observed that if the period of US exposure lengthens, then the concentration of harvested biological material decreases. This is likely due to mechanical and also chemical damage, as formation of oxidizing free radicals was already confirmed in microfluidics (see Chapter 5.3).

8 CFD MODEL

Cavitation in microscale domains has been investigated only sporadically to the date. Although the number of published papers on the topic is on the rise, the presented thesis still deals with phenomena that are neither well documented nor well understood. The main purpose of this thesis is to provide foundation and guidelines for future research in the area of cavitation in microfluidics that will be carried out in joint cooperation between Brno University of Technology (BUT) and Technical University in Liberec (TUL).

The obtained numerical simulations are presented, analyzed and comparison with experimental and numerical data obtained in comparable flow domains is presented when available. The two main sources for comparison are *Rooze et al.* [25] and *Mishra & Peles* [86], [14]. The former serves as point of departure as we deal with exactly the same geometries here. It will be indicated as reference paper throughout the text. Apart from channel dimensions also the boundary conditions are inferred from this source. The latter offers only experimental results and only in the microchannel. These are, on the other hand, quite numerous and inspired the research of *Rooze et al.*

First, the theory behind the applied cavitation model is laid out. This is followed by two sections devoted to two distinct flow geometries. We refer to those as "micro-" and "millichannel", which approximately reflects their dimensions. In each section, the model of the channel and solution preprocessing and setup are presented. Finally, this is followed by results analysis and subsequent discussion where recommendations for future work are made.

8.1 SCHNERR & SAUER CAVITATION MODEL [87]

The numerical solution was carried out with ANSYS Workbench 15.0 software package. Fluent was used for CFD simulations. This software offers three cavitation models to choose from, namely Singhal et al., Zwart-Gerber-Belmari and Schnerr & Sauer model. The last one is used by default and presents the most common choice. This is also the model used for our purposes. The Schnerr & Sauer model uses general vapor equation for the liquid-vapor mass transfer to derive exact expression for net mass transfer term. The general equation is:

$$\frac{\partial}{\partial t}(\alpha\rho_v) + \nabla\cdot(\alpha\rho_v\overrightarrow{v_v}) = S_\alpha, \tag{8.1}$$

where α – vapor volume fraction $[-]$, ρ_v – vapor density $[kg\cdot\ m^{-3}]$, $\overrightarrow{v_v}$ – vapor phase velocity $[m\cdot s^{-1}]$, S_α – net mass transfer source term $[kg\cdot\ m^{-3}\cdot\ s^{-1}]$.
The vapor volume fraction is computed as function of bubble radius R and the number of bubbles contained in unit volume n:

$$\alpha = \frac{(n\frac{4}{3}\pi R^3)}{1+n\frac{4}{3}\pi R^3}. \tag{8.2}$$

If the surrounding pressure p_∞ drops below the vapor pressure threshold, the liquid evaporates and the net mass transfer source term takes the following form:

$$S_\alpha = \frac{\rho_v\rho_l}{\rho}\alpha(1-\alpha)\frac{3}{R}\sqrt{\frac{2(p_v-p_\infty)}{3\rho_l}}. \tag{8.3}$$

Similarly, when the surrounding pressure rises above the vapor pressure the vapor condensates and the net mass transfer source term is now given as:

$$S_\alpha = \frac{\rho_v \rho_l}{\rho} \alpha(1-\alpha) \frac{3}{R} \sqrt{\frac{2(p_\infty - p_v)}{3\rho_l}}, \tag{8.4}$$

where ρ_l – liquid density $[kg \cdot m^{-3}]$, ρ – mixture density $[kg \cdot m^{-3}]$.
The advantage of this model lies in its relative simplicity. The only two parameters we need to provide are the bubble number density n and the magnitude of vapor pressure. Here the value of $10^{14}\ m^{-3}$ for the former is used. This is done consistently with common practice [88]. Vapor pressure is set to 2 339 Pa, which corresponds to ambient temperature of 20 °C.

8.2 MICROCHANNEL

The first considered flow domain is a channel with $100 \times 100\ \mu m^2$ square cross section. Constriction with height 20 μm and length 10 μm is located halfway down the 10 mm long channel. The width remains constant for both channel and constriction. The dimensions together with specified boundary condition locations and types are shown in Figure 8.1. The hydraulic diameters of the channel D_h and of the constriction d_h are 100 and 33.3 μm respectively. The geometry is identical with the one studied in reference paper and it differs only in length from the channel studied by *Mishra & Peles* (see Table 7.1, device #2).

8.2.1 SOLUTION PREPARATION AND SETUP

As the width of the channel remains constant and several times higher than the height and length of the constriction, the flow was modelled in only two dimensions. Furthermore, the symmetry of the domain was exploited and flow only in the upper half was solved. The goal here is to try several setups and to get initial understanding of the problem so that future work on the topic may be more refined. For this reason we want to keep computational times relatively low to be able to iterate over different setups. Hence the simplifications are acceptable and actually desirable.

The geometry was modelled using ANSYS Workbench built-in Design Modeler application. The upstream inlet channel length was modelled as shortened to one fifth of its initial length. Again, this is reasonable simplification as we are chiefly interested in changes in the flow that happen in and downstream of constriction. The length of the inlet region still remained order of magnitude higher than the hydraulic diameter of the constriction. The domain was meshed with in-built meshing functionality of ANSYS Workbench. All faces were mapped meshed with quadrilateral elements. The total number of nodes was over 425 000 and the mesh was refined in the close-to-the-wall and near-constriction regions (see Figure 8.2).

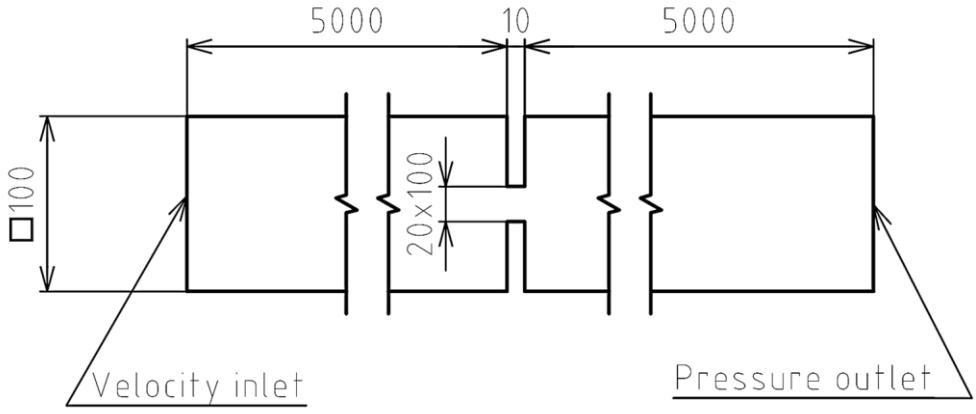

Figure 8.1: *Dimensions of microchannel. All dimensions given in micrometers*

Once the computational domain modelled and meshed, the next step is setting up the solution. Here the value of Reynolds number Re was checked. This non-dimensional parameter marks the transition from laminar to turbulent flow. The generally accepted threshold for internal flow in macroscale circular pipes is 2 300 [1]. For the values of Re between 2 300 and 4 000 the flow is transitional. Nevertheless, the state-of-the-art research suggest that this threshold decreases in microscale domains [89]. The conventional threshold was considered here, but special attention was paid whenever this parameter rose close to and over 1 000. The Reynolds number is defined as:

$$Re = \rho \frac{v \cdot L}{\mu} \, [-], \tag{8.5}$$

where ρ – density $[kg \cdot m^{-3}]$, v – average velocity $[m \cdot s^{-1}]$, L – characteristic dimension of the flow domain $[m]$ and μ – dynamic viscosity $[Pa \cdot s]$.
To calculate average velocity we substitute cross section area A $[m^2]$ and volumetric flow rate Q $[m^3/s]$ to the continuity equation to obtain:

$$v = \frac{Q}{A} \tag{8.6}$$

Using values listed in Table 8.1 and substituting $998.2\ kg/m^3$ and $1\ mPa \cdot s$ for water density and dynamic viscosity respectively, we can evaluate the Reynolds number in the channel as well as in the constriction. For example for the later we obtain:

$$Re_c = 998.2 \cdot \frac{33.3 \cdot 33.3 \times 10^{-6}}{0.001} \frac{kg \cdot m \cdot m \cdot s \cdot m}{m^3 \cdot s \cdot kg} = 1\,107 \tag{8.7}$$

This value lies below the conventional threshold and hence supports the choice of laminar model.

Next, the model for solving two-phase flow must be chosen. Here the Mixture Model is used. This represents a common choice for cavitation. It is suitable for bubbly flows where the bubbles remain small. Gravity can be hence neglected and the relative (slip) velocity equation does not need to be solved [87]. The mixture is then considered as homogeneous distribution of the phases (in this case liquid and vapor). It is not possible to distinguish individual bubbles, rather we obtain a value between 0 and 1 for each vertex of the domain, which describes the void fraction α at this location. At every position in the domain the sum of void and liquid fraction must be then equal to unity. Throughout this thesis the value of 0.2 for void fraction is chosen as threshold under which the vapor phase ceases to be observable. Likewise, the threshold above which the individual bubbles would be observed is set to 0.8. In between lies the region of misty flow, where the fluid appears as continuous hazy mixture.

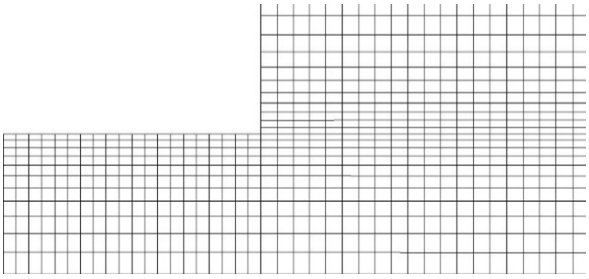

Figure 8.2: *Detail of mesh at constriction exit*

Table 8.1*: Overview of experimental conditions for the microchannel in single case scenario [25]*

$Q\ [\frac{ml}{min}]$	$v_c\ [\frac{m}{s}]$	$v\ [\frac{m}{s}]$	$p_{DS}\ [kPa]$
4	33.3	6.67	102.5
	$d_h[\mu m]$	$D_h[\mu m]$	$\sigma[-]$
	33.3	100	0.365

v_c – average velocity in constriction, v – average velocity in channel, p_{DS} – relative (gage) pressure at channel exit.

***Table 8.2**: Summary of numerical setup*

Model		
	Space:	2D
	Time:	Transient
	Viscous:	Laminar
	Multiphase:	Mixture
	Mass transfer – Cavitation:	Schnerr & Sauer
Solution Methods		
	Pressure – velocity coupling:	SIMPLE
	Discretization Schemes	
	- Pressure:	Presto
	- Momentum:	Second Order Upwind
	- Volume fraction:	First Order Upwind
	- Time:	Second Order Implicit
Unsteady Calculation Parameters		
	Time step $[s]$:	5×10^{-6}
	Maximum iterations per time step:	25
	Data sampling for time statistics:	enabled

Another steps of the solution setup include defining boundary conditions and choosing solution methods and calculation parameters. The complete summary of numerical solution setup is provided in Table 8.2. At each wall a zero normal and tangential velocity were prescribed, this represents the no-penetration and no-slip conditions. The value of time step was chosen low to well accommodate for rapidly evolving nature of cavitating flow, whereas the maximum number of iterations per time step was slightly increased from its default value, i.e. from 20 to 25, to assure solution convergence. Before proceeding to this setup, several hundreds of iterations on less accurate setups were carried out. Each with no more than thousand iterations. This assures that the solution remains well behaved in the initial phase of the calculation, i.e. reduces the likelihood of residuals divergence.

If we wish to track how certain variables change during the solution, we can also choose to define Solution Monitors. These allow us to decipher eventually recurring patterns and to observe the convergence of the solution. Another option how to observe the time development of the flow is to save a picture of chosen variable contours during the calculation. This is done in the Calculation Activities panel. Both ways of variables tracking were used for this thesis. Furthermore, if we suspect that tracked variables continue to change in time during the solution, we may want to review their time-averaged distribution after the calculation has finished. To perform this, we first need to enable Data Sampling for Time Statistics option during the solution setup. This requires us to provide a value for Sampling Interval. It is arbitrary and determines how often, i.e. every which time step, the data for time statistics should be saved. The lower values lead to averaging over larger number of time steps, i.e. more data collected. Also this functionality was enabled in presented solution setup.

8.2.2 ANALYSIS OF RESULTS

The results obtained from calculations with several pairs of boundary conditions are presented in this section. First, results for single case are laid out and these are then built on in section devoted to interpretation of results obtained for multiple boundary conditions pairs.

8.2.2.1 SINGLE CASE RESULTS

The boundary conditions for the single case, namely average velocity at the inlet v and pressure at the outlet p_{DS} are listed in Table 8.1. These values were obtained experimentally by *Rooze et al.* First, the solution monitors tracked during calculation were analyzed, and recurring pattern was deciphered. The liquid forms stable liquid jet engulfed by regions with high void fraction. This jet repeatedly stretches and contracts which induces **periodic changes** in all observed variables. The time-evolving distribution of phases is the most easily understood when looking at the animation included as Appendix on the CD that comes with printed version of the thesis. Approximately one hundred pictures of contours of liquid volume fraction were put into sequence. The images were taken in regular intervals (one image per 20 time steps). The regions in blue are those where liquid volume fraction is close to zero, i.e. where the void fraction α is close to unity. Another possibility how to visualize this periodic behavior is by looking at plots in Figure 8.3. We see there the time record of three distinct variables, all of which clearly manifest periodicity.

If we want to decipher the frequency with which the variables change, it suffices to find times when two consecutive peaks occur and take an inverse value of the difference of those two times. This may become more challenging when the signal becomes noisier and we usually want to use Fast Fourier Transform (FFT) algorithm to search for the frequency for us. This is also what was done here. The algorithm searches supplied data and looks for repeating pattern.

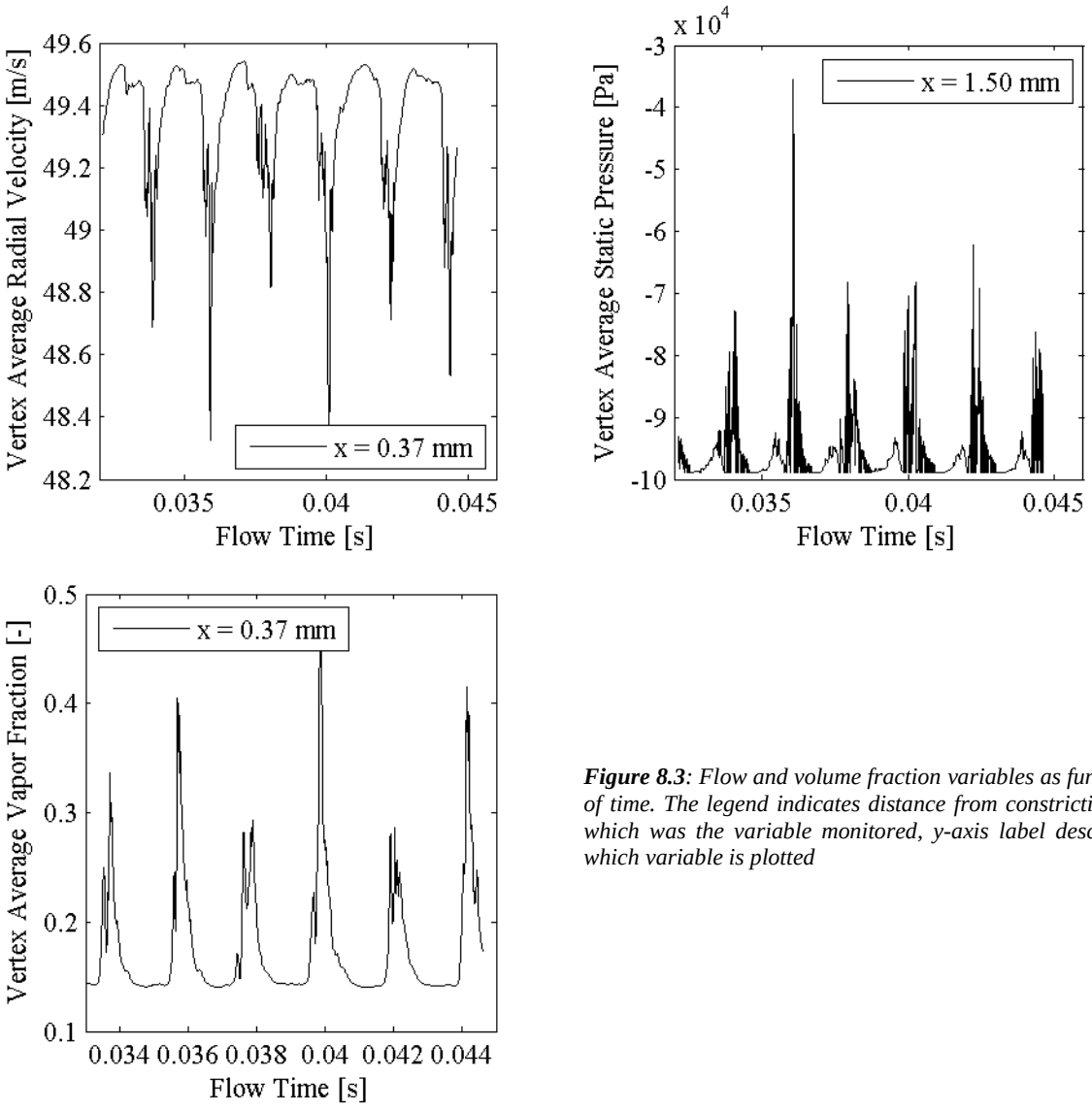

***Figure 8.3**: Flow and volume fraction variables as function of time. The legend indicates distance from constriction at which was the variable monitored, y-axis label describes which variable is plotted*

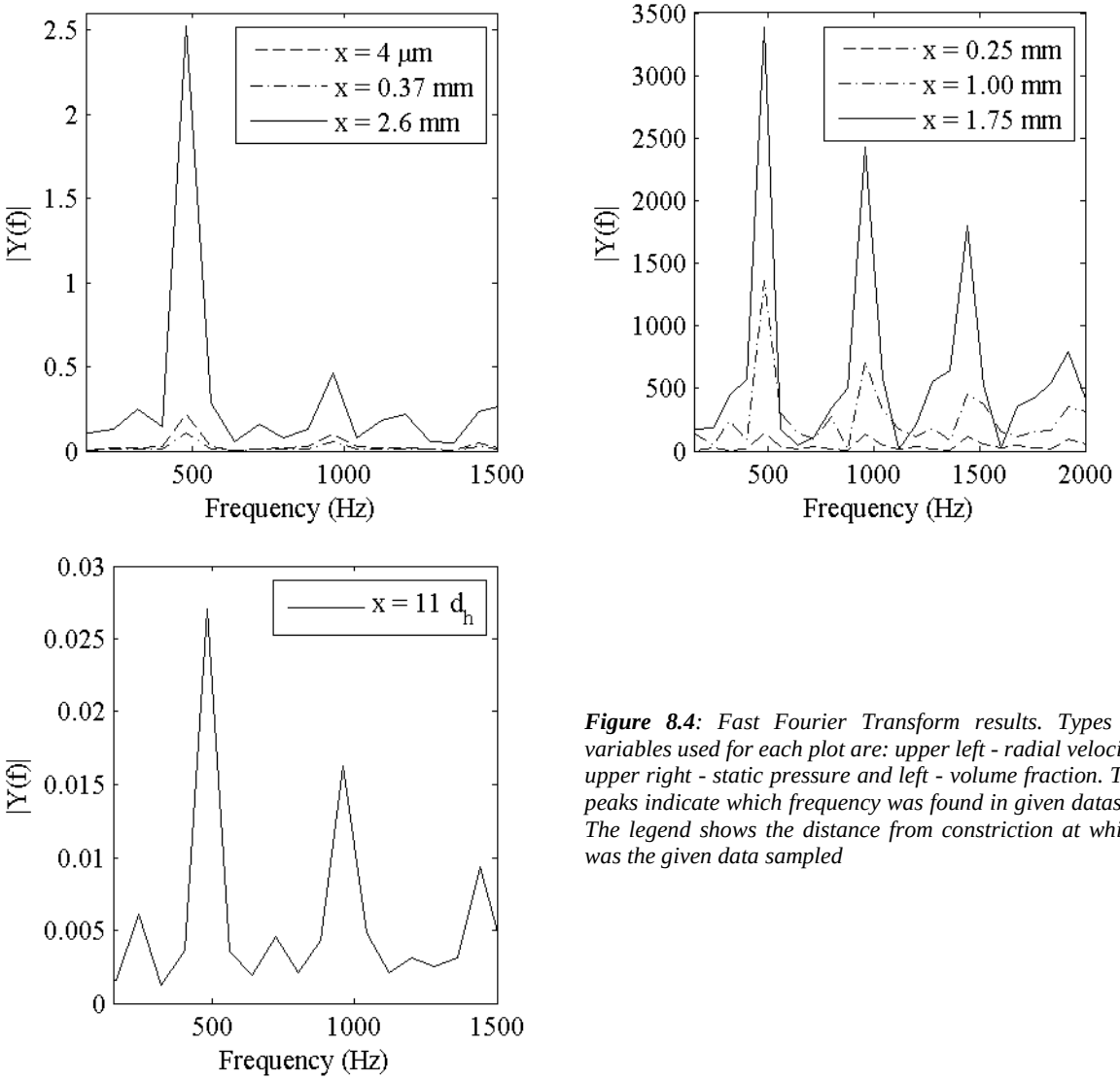

***Figure 8.4**: Fast Fourier Transform results. Types of variables used for each plot are: upper left - radial velocity, upper right - static pressure and left - volume fraction. The peaks indicate which frequency was found in given dataset. The legend shows the distance from constriction at which was the given data sampled*

The output is then plotted as function of frequency, peaks responding to frequencies spotted in the dataset. In this case the frequency found was $480\ Hz$ (see Figure 8.4).

Second, we can analyze the **velocity** in the constriction and compare it with value yielded by calculation of continuity equation (8.6). Before this done, recall that that the velocity distribution in direction orthogonal (y) to the flow direction (x) is by no means constant neither in the channel nor in the constriction. Nevertheless, there is certain location where the velocity profile does not change much along the y direction. This location is constriction entrance. We can verify this by looking at Figure 8.6. The averaged velocity computed from this plot is $34.8\ m/s$ which is less than 5 % different from the value obtained from the continuity equation. The values therefore show a good agreement.

Interesting observation regarding the velocity in the constriction can be made. In the center of the constriction there is liquid jet of high x-velocity. With increasing distance from the centerline of the channel the x-velocity decreases and even goes to negative values, almost half in the magnitude compared to the velocity of the jet in the center. Then the x- velocity rises to zero at the wall to conform to the no-slip condition (Figure 8.5). This indicates a recirculation region. This phenomenon is probably due the global minimum of static pressure that occurs near the wall, soon after the fluid enters the constriction. Pressure minimum at this location was likewise found numerically by *Rooze et al.* in reference paper.

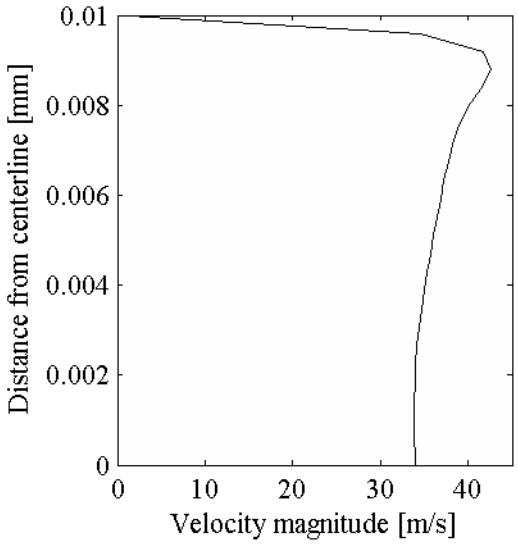

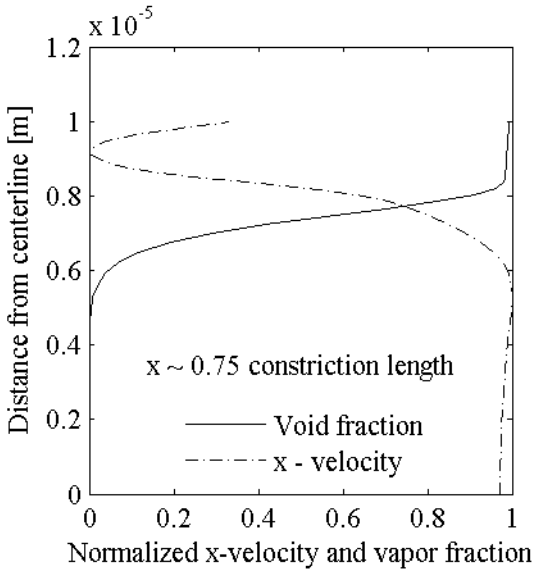

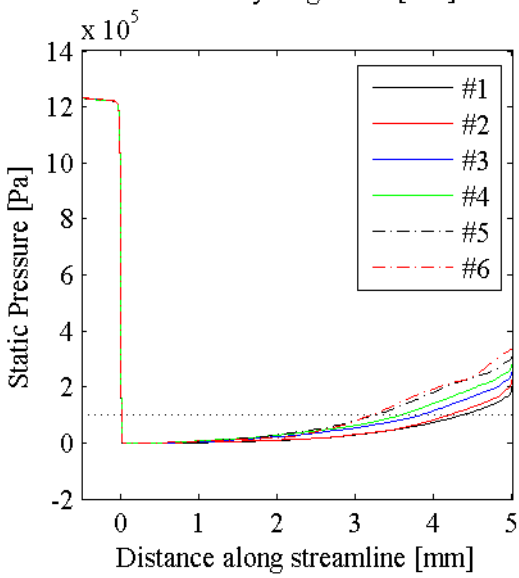

***Figure 8.5**: Upper right: Mean x-velocity and vapor fraction as function of the distance from centerline. The values of velocity were normalized[15] to fall between 0 and 1. The data is taken in three quarters of the constriction length. For actual values of velocity refer to Figure 8.13*

***Figure 8.6:** Upper left: Velocity magnitude at the constriction entrance. Here x = 0. The line of symmetry is located at y = 0*

***Figure 8.7**: Left: Pressure drop along the centerline. The value of pressure is absolute. The dotted line indicates atmospheric pressure. The numbers in legend correspond to cases as in Table 8.3*

Third, let us examine how **pressure** changes along the centerline. The pressure drops rapidly after entering the constriction. We see from Figure 8.7 that the magnitude of pressure drop is 1.2 MPa and this agrees well with numerically found pressure drop of 1.28 MPa reported by *Rooze et al.*

There is a long pressure recovery region and the pressure rises above the ambient atmospheric value only after fluid traveling over 3 mm downstream (see Figure 8.7). This is not straightforward to interpret as conflicting evidence exists for similar conditions. On one hand, such a long pressure recovery region does not agree neither with experimental nor with numerical data obtained by *Rooze et al.* They measured relative pressure at distance 460 μm from constriction and found it to be 50 kPa. On the same account, they reported at this location numerically found value 15 kPa. In our case, the pressure stays close to vapor pressure at this location. On the other hand, when we consult the results of *Mishra & Peles* [14] we get to see wholly different picture. For comparable cavitation number they reported supercavitation (see Table 7.1, device #2 and Figure 7.2) and two long stable vapor bubbles stretching even 4 mm downstream from constriction. This suggests long pressure recovery region and therefore supports presented results.

[15] We find normalized value a_n of quantity a by calculating:

$$a_n = \frac{a - \min(a)}{\max(a) - \min(a)}.$$

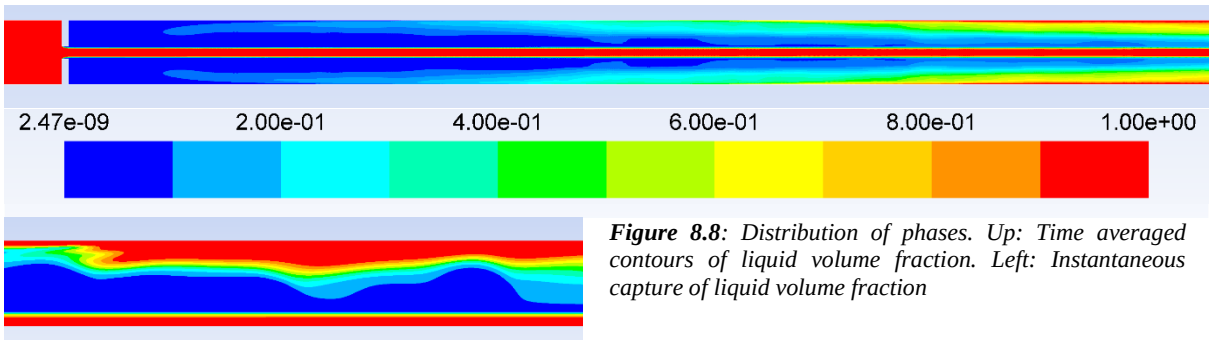

***Figure 8.8**: Distribution of phases. Up: Time averaged contours of liquid volume fraction. Left: Instantaneous capture of liquid volume fraction*

There are, however, several complications that present hurdles to direct comparison with mentioned sources: (A) *Rooze et al.* used steady state SST turbulent model, (B) *Mishra & Peles* evaluated cavitation number using pressure measured at $2.2\,mm$ downstream from the constriction, next (C) they used a channel with twice as long outlet region as the one modelled here and finally they achieved similar pressure differences as we observe here but (D) they did that by lowering exit pressure even below atmospheric pressure.

Fourth, the distribution of **vapor phase** was analyzed. Long and stable liquid jet engulfed by regions of high void fraction periodically stretches all the way to the channel exit and retracts as already described. When we observe instantaneous contours of liquid fraction (as in the included animation or Figure 8.8) we see regions with high void fraction with wavy boundaries that are separated from the channel wall by thin layer of liquid. It is supposed that the wavy pattern supports the stability of vapor phase. When we examine the contours of time averaged distribution of phases, we see the jet, i.e. region where liquid fraction is unity, in the center. Its thickness remains approximately constant till the channel exit. This region is surrounded by area where void fraction remains high. Close to the jet, the vapor volume fraction remains above 0.2 even at the channel exit. This is further shown in Figure 8.8 and Figure 8.16.

As it was already noted, these results agree well with experimental observations of *Mishra & Peles*. This is further evidenced in Figure 8.9 where high speed camera captures of cavitating flow in microchannel are reprinted. Long and stable liquid jet engulfed by vapor bubbles touching device walls can be seen in the upper two images. In the image on the left a wavy pattern of cavity boundary is clearly visible.

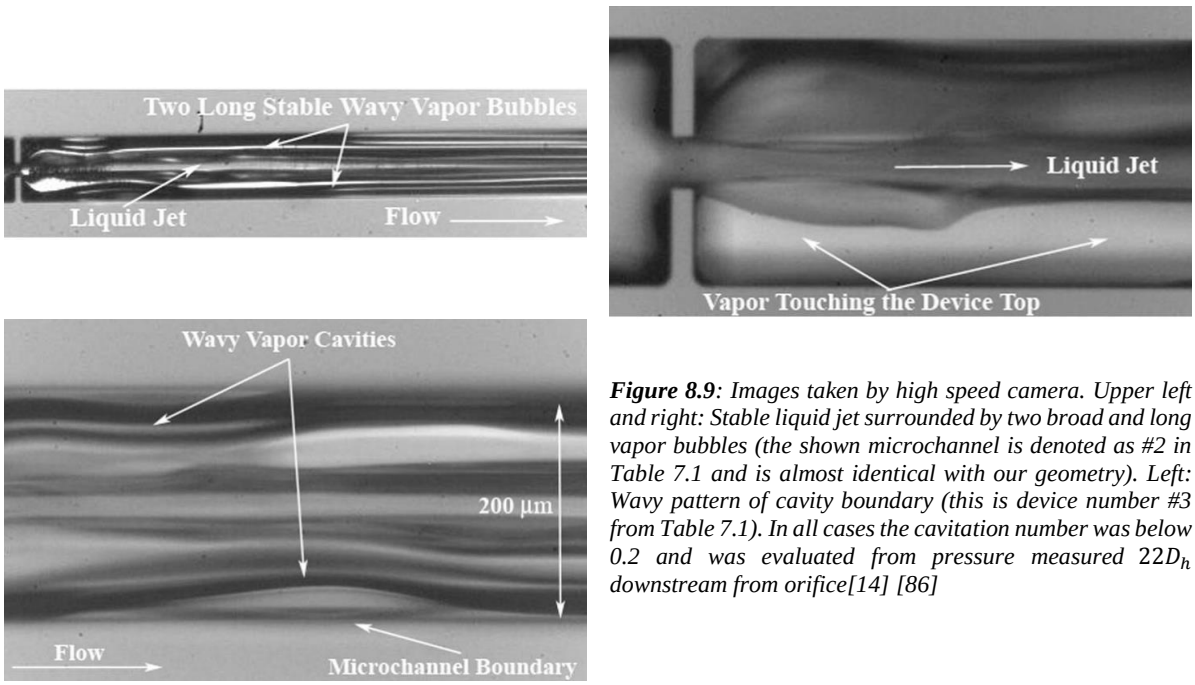

***Figure 8.9**: Images taken by high speed camera. Upper left and right: Stable liquid jet surrounded by two broad and long vapor bubbles (the shown microchannel is denoted as #2 in Table 7.1 and is almost identical with our geometry). Left: Wavy pattern of cavity boundary (this is device number #3 from Table 7.1). In all cases the cavitation number was below 0.2 and was evaluated from pressure measured $22D_h$ downstream from orifice[14] [86]*

8.2.2.2 MULTILPLE CASES RESULTS

This section expands on the previous one. It presents analysis of results obtained on several cases with increasing cavitation number. This is done mainly to get better understanding of the nature of the model as well as of the displayed physical phenomena. To obtain boundary conditions for these cases, the inlet velocity was kept constant at $6.67\ m/s$ and the pressure at the outlet was stepwise increased as indicated in Table 8.3. To obtain pressure magnitudes for cases #2–#6, the cavitation number was increased by 0.05 for each step. For example for case #1 and using pressure at the outlet we get:

$$\sigma = \frac{p_{DS} - p_v}{\frac{1}{2}\rho v_c^2} = \frac{(203\,825) - 2339}{\frac{1}{2} \cdot 998.2 \cdot 33.3^2} = 0.365 \tag{8.8}$$

and because $\sigma = 0.365 + 0.05 = 0.415$, therefore for case #2:

$$p_{DS} = \left(0.415 \cdot \frac{998.2 \cdot 33.3^2}{2} + 2339\right) - 101\,325 = 130\ kPa. \tag{8.9}$$

Following the same order as in the previous section devoted to single case, let us first focus on the **periodicity** of studied flow. Using the same procedure as already described, we can determine the frequency with which the flow variables change. Doing that we arrive to a relationship that is shown in Figure 8.10. This is rather strange as in macroscale domains the usually observed behavior is of increasing frequency with increasing cavitation number, i.e. the opposite. The liquid containing more vapor is generally more compliant. This could be due to the fact that lesser volume of vapor is formed at low cavitation numbers. If we refer to chapter 7, we can see there that cavitation choking occurs almost immediately after cavitation inception. Hence we suppose that presented calculations all happen in choking regime and increasing pressure at outlet leads to "dechoking" and allows more fluid to pass through the constriction. This in turn leads to enhanced mass transfer rate and higher vapor yield.

To check this hypothesis, we look at area where the value of mean vapor fraction is higher than 0.2. This area changes from 0.185 to $0.116\ mm^2$ for cases #1 and # 6 respectively. We plot then the normalized relative size of this area as function of cavitation number. The relative size is calculated as:

$$A'_v = \frac{A_v}{A_t} \cdot 100\ [\%] \tag{8.10}$$

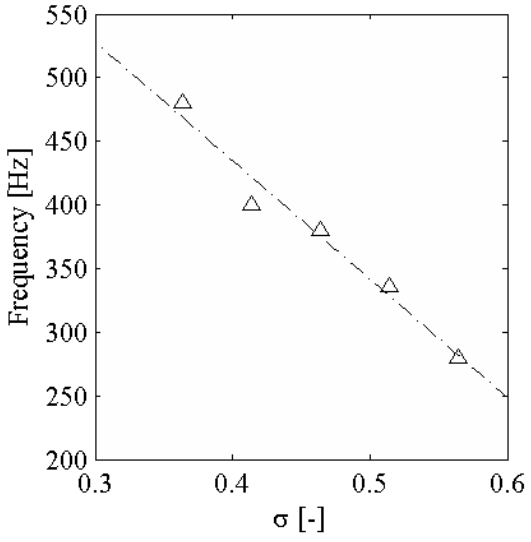

***Figure 8.10**: Frequency with which variables change as function of cavitation number*

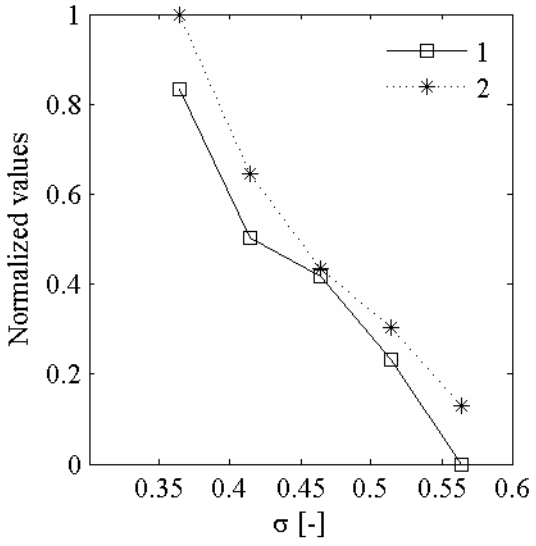

***Figure 8.11**: Normalized values (see footnote 15 at page 37) of: line **1** – frequency and line **2** – fraction of surface*

where A_v – area of the region in and behind the constriction where the void fraction is higher than 0.2 $[mm^2]$ and $A_t = (0.05 \cdot 5) + (0.01 \cdot 0.01) = 0.2501\ mm^2$ – the total area of constriction and behind-constriction region (here only one half of the symmetrical domain is considered).

Upon contemplating the Figure 8.11 we see that with increasing cavitation number the amount of vaporized liquid decreases. This is in agreement with usual macroscale results, however it refutes the proposed hypothesis. Other possible explanation for the frequency-cavitation number relationship could be that the oscillations of flow variables as we observe them represent only minor rebounds. If this was the case, then there would be higher oscillation magnitudes occurring at lower frequencies. To check this hypothesis, data over more than 8 000 time steps for several cases were collected. Considering the time step size we get total observed period of 0.04 s. This represents the lowest observable frequency of 25 Hz. Nevertheless, no stronger periodically repeating oscillations were observed.

It may not have escaped the eye of attentive reader that only 5 out of in total 6 solved cases were plotted in Figure 8.10. This is because the frequency becomes more and more difficult to decipher as the pressure at the outlet increases. Whereas in the case #1 the FFT algorithm finds the frequency without any problems, for case #6 with comparable length of dataset the signal is much noisier. It is believed that what we observe here (see Figure 8.12) is decay of periodic behavior to subharmonics. This may be a sign that some significant change in the flow behavior is soon to happen. It could be either transition from choking cavitation to a developed cavitation or, if we were crossing the boundary of cavitation number at inception, the transition from developed cavitation to non-cavitating regime. We may recall from chapter 7 that these two changes are bound to happen in similar conditions, without necessitating significant change in boundary conditions. What makes the interpretation of these results even more challenging is the notion of flow hysteresis [14]. According to experimental observations of *Mishra & Peles* these two described transitions happen each at different cavitation number depending on whether we are inducing the change

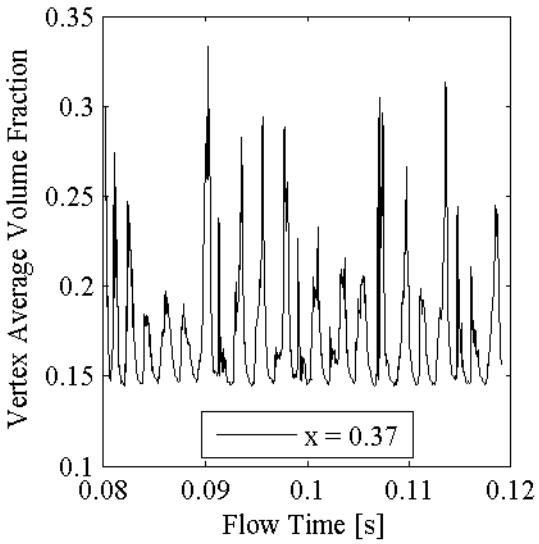

***Figure 8.12**: Up: Vertex average of liquid volume fraction sampled every time step at distance x = 11d_h. The frequency with highest power peak found by FFT is 520 Hz*

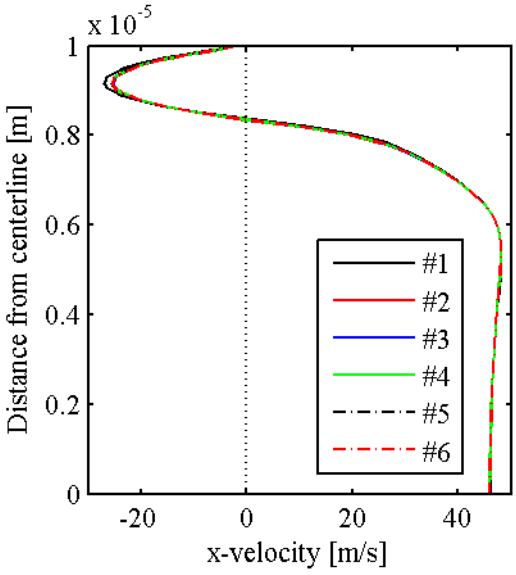

***Figure 8.13**: Right: x-velocity profiles taken at three quarters of constriction length*

***Table 8.3**: Down: Overview of solved cases. The inlet velocity remained constant*

Case No.	p_{DS} $[kPa]$	σ $[-]$
#1	102.5	0.365
#2	130	0.415
#3	158	0.465
#4	186.5	0.515
#5	213	0.565
#6	241	0.615

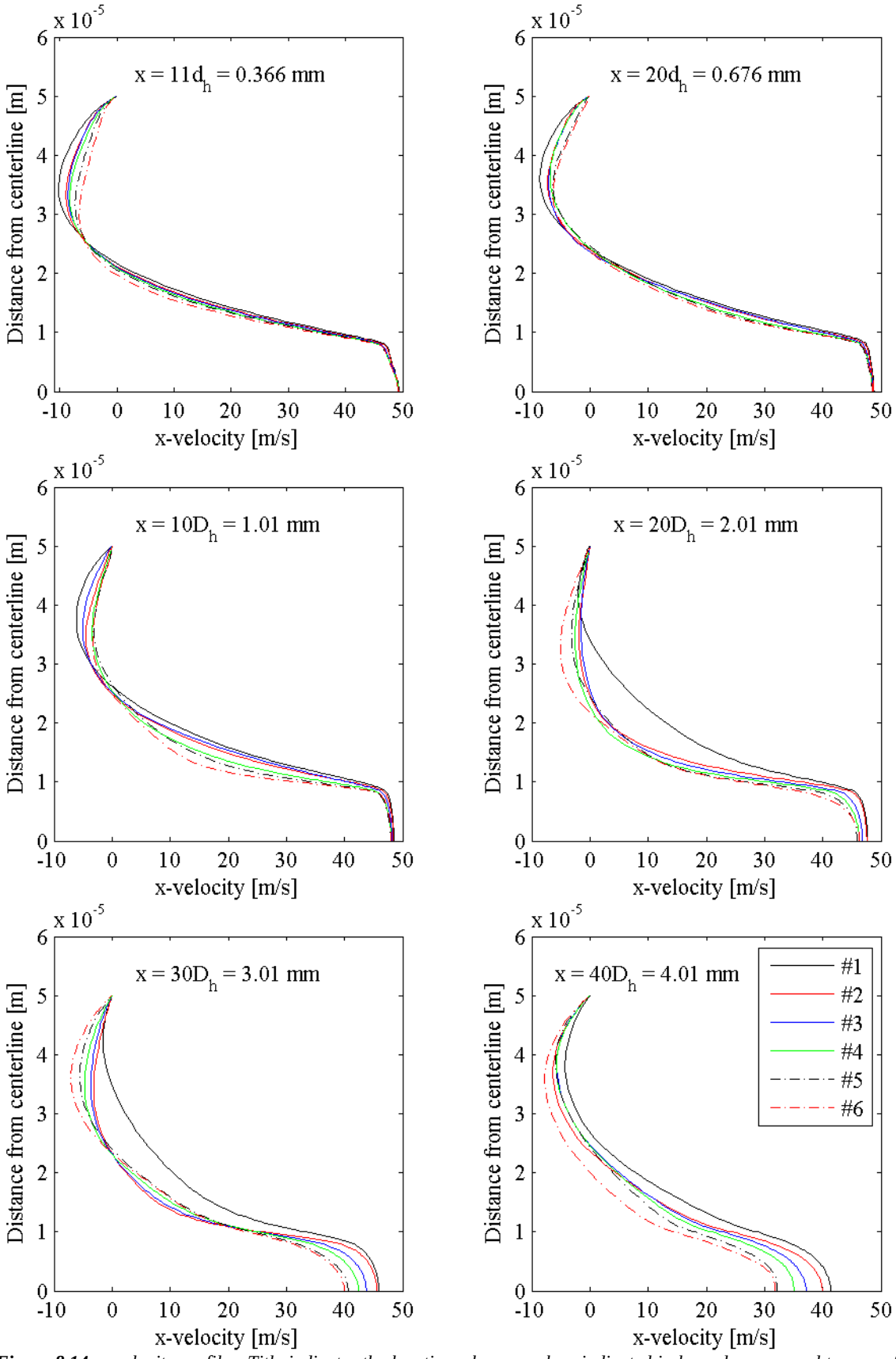

Figure 8.14: *x-velocity profiles. Title indicates the location whereas colors indicated in legend correspond to cases from Table 8.3. Line of symmetry is at y = 0. Data for case #1 was averaged over different number of time steps*

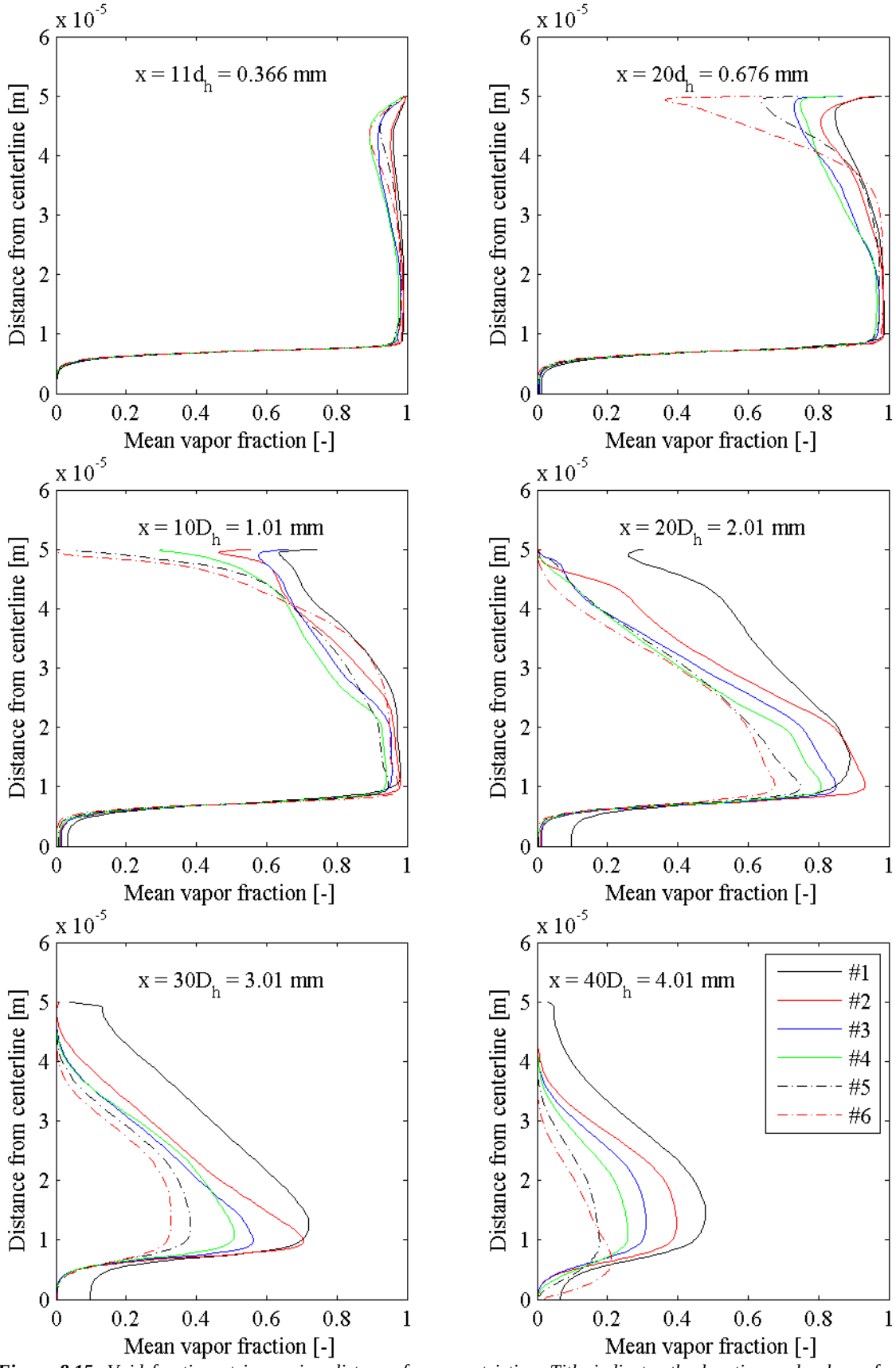

Figure 8.15: *Void fraction at increasing distance from constriction. Title indicates the location and colors of curves correspond to cases from Table 8.3. Legend holds for all plots. The line of symmetry is at y = 0*

to the flow by reducing, or on the other hand by increasing, cavitation number. For comparable geometries they reported the desinent cavitation number (σ at which the cavitation bubbles completely disappear due to outlet pressure increase) to be more than two times higher than cavitation number at inception.

Second, **velocity** profiles in the flow domain were analyzed. These were taken along y direction (orthogonal to the direction of the flow) at increasing distance from constriction. Albeit different at each location, all show the same feature, i.e. they become increasingly sensitive to changed boundary condition with decreasing distance towards the channel exit. This is the most easily understood when we look at Figure 8.13 and Figure 8.14. We observe that there is always recirculation region near the wall present. The shape of the profile is more pointed near the constriction and progressively becomes less so. The profile corresponds to liquid jet of high velocity in the center of the channel with regions of high vapor fraction around it.

Third, if we, quite like with the velocity, plot the profiles of **void fraction,** we can observe how this depends on the counter pressure and the distance from constriction. We can nicely examine the region of high void fraction attached to the microchannel boundary. It can be seen that this region eventually separates from the channel wall as the distance travelled by fluid increases. This happens some 1 to 2 mm from constriction and exact location depends on the value of cavitation number. The lower the cavitation number, the longer it takes before there is region of higher liquid fraction between the void fraction and the wall. In experimental observations this would correspond to bubbles touching the device walls downstream the constriction. This is exactly what we can see in photos taken by high speed camera by *Mishra & Peles* (see Figure 8.9).

Fourth, we will observe the **pressure** recovery along the line of symmetry. The same as for single case discussed in previous section holds true. The value of pressure remains low and recovers to atmospheric pressure only in the last two fifths of the channel, depending on the value of outlet pressure. Studying the plot of pressure recovery (see Figure 8.7) we can understand where the highest pressure gradient happens spatially. We are now interested in where there is the highest time-dependent change of pressure in the fluid domain that is caused by repetitive lengthening and retracting of the liquid jet.

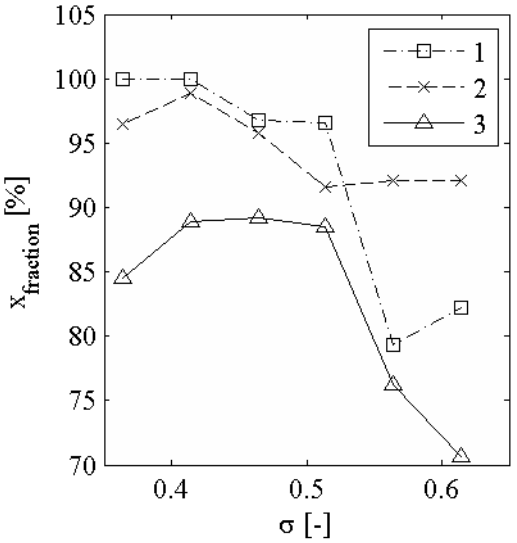

Figure 8.16: *x-coordinates as fraction of total outlet region length (5 mm) and function of cavitation number.* ***1*** *– maximum x-coordinate of area where mean* $\alpha > 0.2$, ***2*** *– area weighted average x-coordinate of area where RMS of Static pressure is higher than 90 % of its maximum value and* ***3*** *– x-coordinate of maximum of mean wall shear stress*

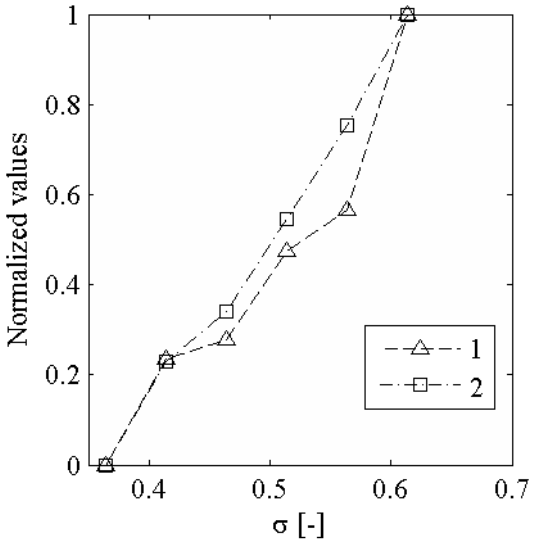

Figure 8.17: *Normalized values (see footnote 15 at page 37) of:* ***1*** *– maximum RMS of Static pressure (range from 102.9 kPa to 131.6 kPa) and* ***2*** *– Mean wall shear stress averaged over outlet channel wall (range from 144.3 Pa to 364.7 Pa)*

We define the location with highest changes of pressure in time using root-mean-square values. More precisely, we consider the area where the RMS of Static pressure is equal to or above 90 % of its maximal value. We observe that this region is located near the channel outlet and it shifts towards the constriction with increasing cavitation number. If we define a region where void fraction is over 0.2 and track maximal stretch of this area, as plotted in Figure 8.16, we can see that this corresponds with the location of highest RMS values of pressure. Moreover, we clearly see that the vapor fraction remains above 0.2, even as the mixture exits the channel, for cases #1 and #2. Also for the rest of the cases #3–#6 this region stretches far in the channel. This supports previous results (see Figure 8.15). Moreover, this helps us to better understand the slow pressure recovery as regions where there is at the same time non-zero void fraction and higher-than-atmospheric pressure have difficult time to coexist in our simulations.

Another variable that is analyzed is **wall shear stress**. This represents tangential part of the stress and when integrated over area it yields shear force [1]. This may be of interest if we want to stretch or porate membranes of microorganisms populating the walls. We see that the wall shear stress averaged over channel wall increases with increasing cavitation number and this corresponds with how much the pressure changes in time (see Figure 8.17). This can further be put into connection with Figure 8.15, where we see that longer part of the wall is in contact with liquid when the cavitation number is higher. It may be concluded that liquid shears the wall more than mixture with high void fraction. Furthermore, in studying again Figure 8.16, we observe that the location of the maximum of mean wall shear stress moves towards constriction with increasing outlet pressure. The observed maxima range from 950 Pa for case #1 to 1375 Pa for case #6.

Last but not least, one more case was solved to complement the presented analysis. It differs from the previous six cases by much higher magnitude of downstream pressure. The pressure outlet boundary condition was set to $400\ kPa$ of gage pressure. This was done in order to observe fast transition between cavitation regimes as discussed in this chapter and in chapter 7. The solver pressure drops as low as vapor pressure at the wall near the constriction entrance but rises immediately to higher values and this does not suffice for formation of vapor phase. No cavitation was observed. Still, this result is valuable as it represents the upper boundary for future numerical simulations in this domain.

8.2.3 DISCUSSION AND RECOMMENDATIONS

In presented analysis, several aspects lend themselves for further research. Foremost, the exhibited frequency-cavitation number relationship is inverse to what has been observed on macroscale so far. More numerical and experimental studies are required on this to either confirm or refute the validity of suggested relation. Likewise the slow pressure recovery and to this related stability of vapor phase are peculiar and should be subject to further investigations.

Several recommendations for further research can be inferred from analyzed results:

- Numerical simulations using turbulent model and eventually also Large Eddy Simulation (LES) model are advisable. Especially to investigate the pressure recovery and the length of region filled with vapor phase.
- Longer computational domain should be used to rule out the influence of outlet boundary condition on the development of flow in the region of interest. Twice the current length shall suffice.
- Using the insight gained thanks to this thesis, numerical calculations should be carried out with increased values of outlet pressure (or reduced volumetric flow). By doing this, the fast transition between cavitation regimes and flow hysteresis can be studied in-depth.

- It is worth considering modelling the flow domain in 3D to get more accurate picture of near wall regions and how the variables in near wall regions change in time and also spatially. Moreover, LES model is available only in 3D.
- An experiment building on knowledge acquired during numerical projects would represent quite rare example of research and would put numerical results under strict scrutiny. Also more thorough understanding of the cavitation phenomenon is bound to be gained in this way.

8.3 MILLICHANNEL

The main goal of the paper presented by *Rooze et al.* [25] was to evaluate radical production due to cavitation in micrometer sized constrictions and channels. They were not able to measure any radical production (and consecutive species oxidation) in the microchannel. Possibly due to shape of the cavities which by far are not spherical and thus lead to reduction of hot spot temperatures (see previous section and chapter 5). They therefore proceeded to experiments in a larger domain, i.e. millichannel. Following section of the thesis deals with modeling this setup and analyzing obtained results.

The millichannel device from reference paper is represented by circular inlet channel of diameter $750\ \mu m$, this is followed by circular constriction with diameter $180\ \mu m$.The constriction is $500\ \mu m$ long and expands to brick-shaped chamber with dimensions $8 \times 5.2 \times 4\ mm^3$(length, height and width respectively). This chamber then again shrinks to form long outlet channel with same diameter as inlet channel. The lengths of the inlet and outlet channel are 10 and 28 mm respectively.

8.3.1 SOLUTION PREPARATION AND SETUP

The model of the channel is defined in Figure 8.18, where also locations and types of boundary conditions are pictured. Only one quarter of the full domain was modelled as two planes of

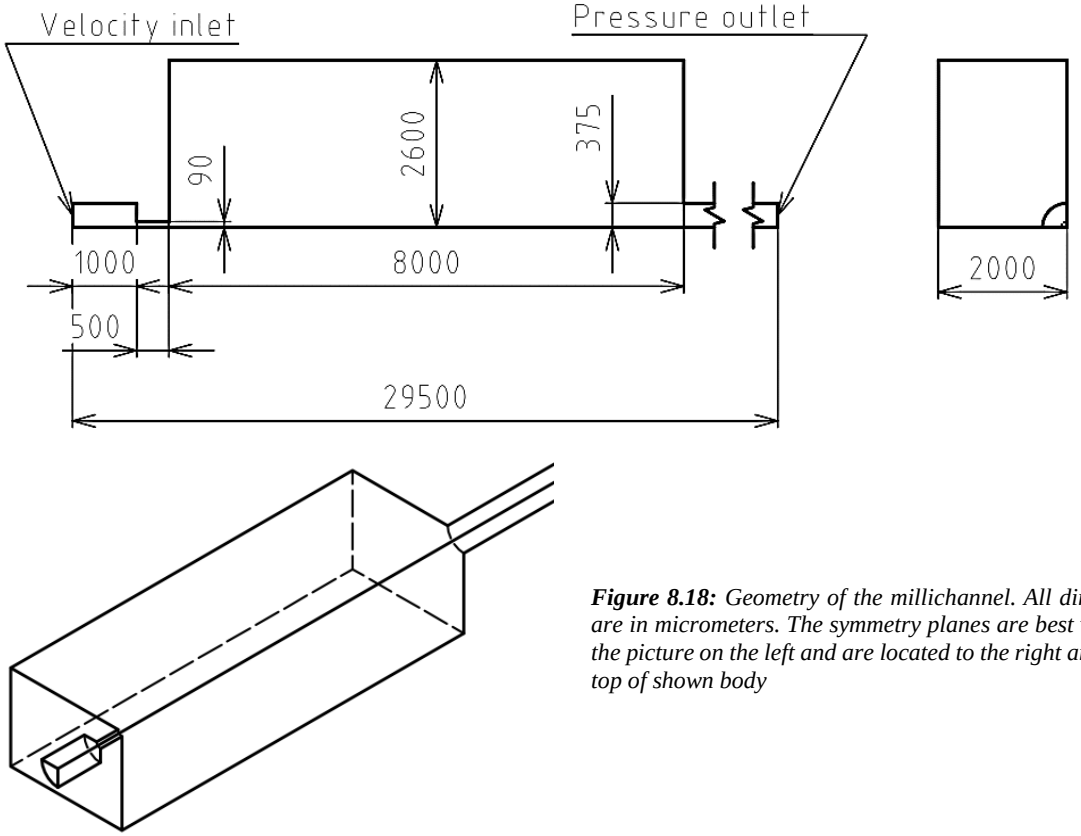

Figure 8.18: *Geometry of the millichannel. All dimensions are in micrometers. The symmetry planes are best visible in the picture on the left and are located to the right and on the top of shown body*

symmetry were exploited. Furthermore, the inlet region was modelled as reduced to 1/10 of original length. Its length remained several times larger than the constriction hydraulic diameter. The goal here is again to get initial understanding of the problem so that future work on the topic may be more refined. For this reason we want to keep computational times in reasonable scale, hence the simplifications are acceptable and actually desirable.

The computational domain for the 3D case was meshed using ANSYS Workbench meshing utility. All faces were mapped with quadrilateral elements and sweep method was used to create hexahedral volume elements. The total number of nodes was over 529 000, which even exceeds the mesh density used in reference paper. The minimum orthogonal quality was 0.42. The mesh was positively biased towards the walls and towards the constriction region, whereas the far-outlet-region mesh quality was reduced.

The same procedure as in the case of microchannel was followed. The experimental data provided in reference paper are listed in Table 8.4. We substitute velocity and cross section area to the continuity equation to obtain velocity at corresponding location of the flow domain. Before proceeding to solution setup we check the value of Reynolds number. Considering the worst case scenario, i.e. case #3 (see Table 8.4) with the highest volumetric flow rate and evaluating the Reynolds number at the constriction, we get:

$$Re_c = 998.2 \cdot \frac{39 \cdot 180 \times 10^{-6}}{0.001} \frac{kg \cdot m \cdot m \cdot s \cdot m}{m^3 \cdot s \cdot kg} = 7\,007. \tag{8.11}$$

On the other hand when we evaluate Reynolds number for case #1 in the inlet channel we obtain:

$$Re = 998.2 \cdot \frac{0.53 \cdot 750 \times 10^{-6}}{0.001} \frac{kg \cdot m \cdot m \cdot s \cdot m}{m^3 \cdot s \cdot kg} = 397. \tag{8.12}$$

As can be immediately seen the Reynolds number varies quite widely among considered cases and among different locations in the flow domain. To facilitate comparison among the cases same model should be applied for numerical solution. Consistently with the microchannel setup we choose here also the laminar model.

The complete overview of solution setup is in Table 8.5. It is almost identical to microchannel set-up except for that we use 3D model here. Also the size of the time step differs. The chosen value, i.e. $2 \times 10^{-7}\ s$, is quite low but was necessitated by momentum and pressure equations divergence that otherwise occurred during the calculations.

8.3.2 ANALYSIS OF RESULTS

Following the same pattern as in the microchannel case, first results for a single solved case will be presented and interpreted and this will be followed by comparison of results across several cases. The boundary conditions for all cases are summed up in Table 8.4.

8.3.2.1 SINGLE CASE RESULTS

For the single case scenario the case #3 is chosen, as the reference paper provides the most information on it. It is also the one where the most intense cavitation was observed. First, the

Table 8.4: *Overview of experimental conditions provided in reference paper [25] and used for presented simulations*

Case No.	$Q\ [ml/min]$	$v\ [m/s]$	$v_c\ [m/s]$	$p_{DS}\ [kPa]$	$\sigma\ [-]$
#1	14	0.53	9	130	5.67
#2	20	0.76	13	150	2.95
#3	60	2.26	39	310	0.53

v_c – average velocity in constriction, v – average velocity in channel, p_{DS} – relative (gage) pressure at the channel exit, hydraluic diameter of the channel $D_h = 750\ \mu m$ and hydraulic diameter of the constriction $d_h = 180\ \mu m$.

***Table 8.5**: Overview of solution setup for millichannel*

Model		
	Space:	3D
	Time:	Transient
	Viscous:	Laminar
	Multiphase:	Mixture
	Mass transfer – Cavitation:	Schnerr & Sauer
Solution Methods		
	Pressure – velocity coupling:	SIMPLE
	Discretization Schemes	
	- Pressure:	Presto
	- Momentum:	Second Order Upwind
	- Volume fraction:	First Order Upwind
	- Time:	Second Order Implicit
Unsteady Calculation Parameters		
	Time step $[s]$:	2×10^{-7}
	Maximum iterations per time step:	25
	Data sampling for time statistics:	enabled

distribution of **vapor volume fraction** was studied. We can see that the vapor phase develops soon but not right after the liquid enters the constriction. This evolution of vapor phase in constriction is shown in Figure 8.19 and Figure 8.20 displays a surface where the void fraction α is constant and equal to 0.2. It can be seen that the region of high vapor phase first travels along the wall but becomes detached approximately in three quarters of the constriction length and then enters the chamber in form of a ring. These vapor rings were experimentally observed by *Rooze et al.* According to their numerical solutions the pressure recovery takes place already in the constriction. It can be supposed then, that there is a relationship between where the pressure recovery occurs and where the vapor phase detaches from the channel boundary.

Next, let us study how this vapor rings develops once it enters the brick-shaped chamber. The vapor fraction in the chamber remains high. In significant part of the domain there is volume where the vapor fraction rises above 0.2 (Figure 8.21). Investigating the distribution of phases further we realize that there are two locations where the void fraction approaches values close to unity (Figure 8.22). One such volume becomes detached from the main stream as the mixture enters the chamber and resides in immediate vicinity of the chamber wall. The other, more oblong, is located along center part of the channel. Contrary to that, the immediate center of the chamber shows liquid fraction equal to unity and this, as in the microchannel case, testifies the presence of liquid jet engulfed by cavities. Regions with vapor fraction over 0.2 would likely appear as sort of milky and misty flow when observed experimentally, whereas regions of high vapor fraction, i.e over 0.8 would appear as vapor bubbles and should have distinguishable boundaries. We can also remark that the regions of noticeable void fraction disappear once the chamber narrows down to form the outlet channel. At this point, the reader may want to consult Appendix where the animation of changing contours of liquid volume fraction is included. The contours are plotted on the plane of symmetry and the animation spans over 8 000 time-steps.

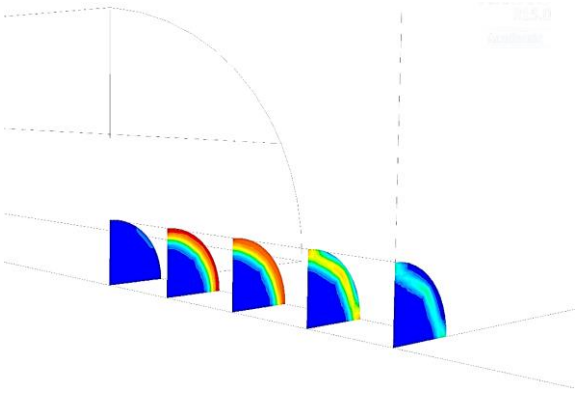

Figure 8.19: *Contours of vapor fraction in the constriction. The values range from 1 (red) to 0 (deep blue). The contours are plotted every 125 μm starting at constriction entrance (i.e. x = 0)*

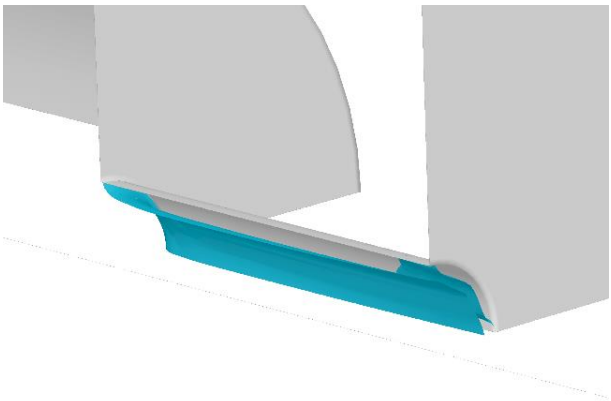

Figure 8.20: *Surface of constant volume fraction (α = 0.2) in constriction*

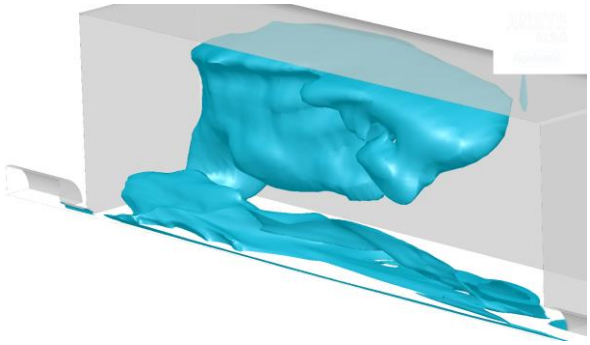

Figure 8.21: *Surface where vapor volume fraction is constant and equal to 0.2*

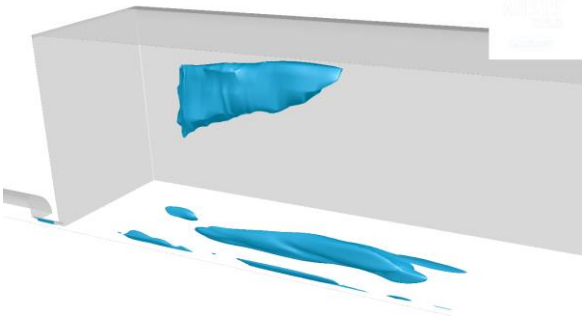

Figure 8.22: *Surface where vapor volume fraction is constant and equal to 0.8*

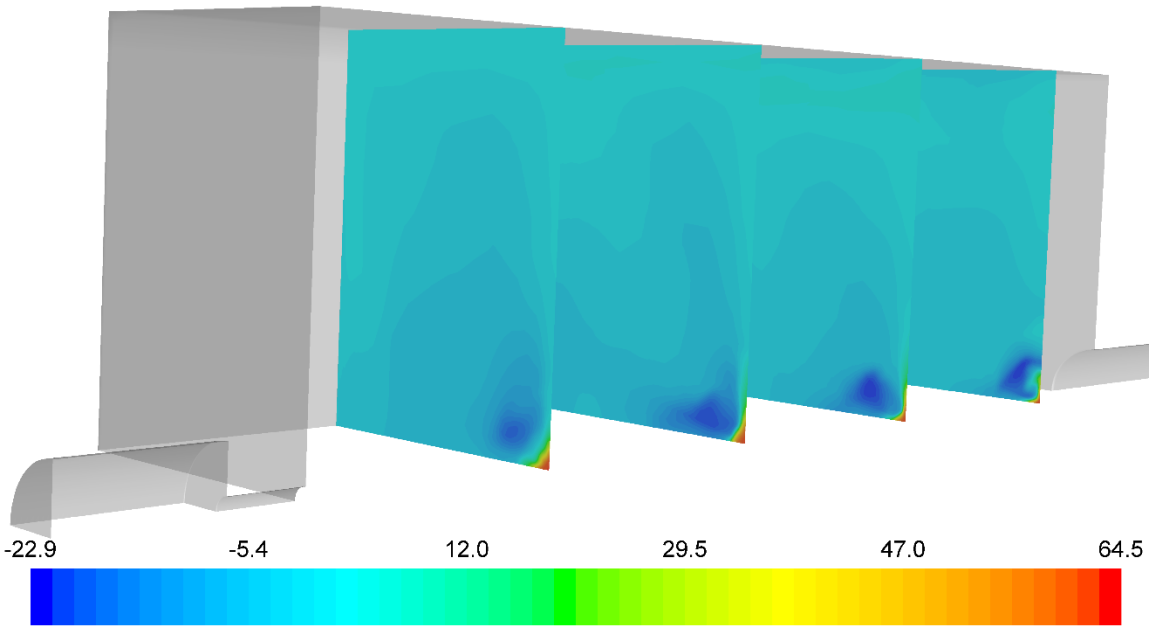

Figure 8.23: *Contours of x velocity [m/s] in the chamber, x direction represents the direction of the flow. The contours are taken at 10, 20, 30 and 40 D_h from constriction exit. We see a thin liquid jet surrounded by region of intense recirculation*

Third, the liquid jet, its immediate surroundings and axial **velocity** distribution can be closely reviewed. As aforementioned, the fluid enters the brick-shaped chamber through the constriction and forms a liquid jet. This jet manifests high velocity and is surrounded by recirculation regions where the x-velocity is negative. This can be observed on velocity contour plots taken at increasing distance from constriction (Figure 8.23). We can see that the jet slightly

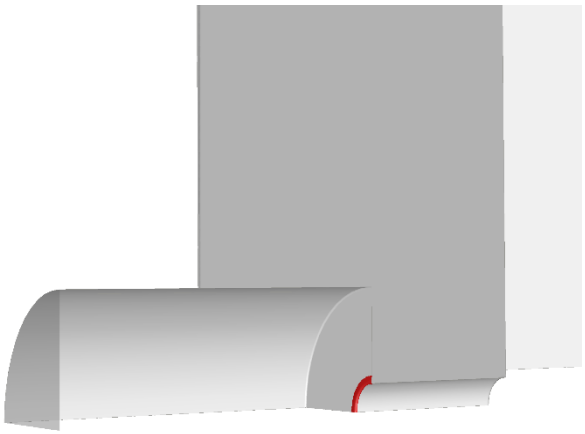

***Figure 8.24**: Location of global maximum of wall shear stress*

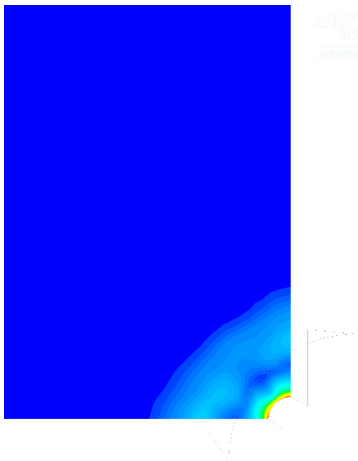

***Figure 8.25:** Distribution of the wall shear stress on the upstream wall of the chamber*

expands and then again becomes thinner as the fluid exits the chamber. This is accompanied by increase of magnitude of recirculation velocity (i.e. the x-velocity becomes more negative) and also the amount of recirculated fluid increases. The described center region is then surrounded by fluid moving at fraction of speed of the liquid jet. The x-velocity gradually rises and becomes positive in the near-to-wall regions. The same x-velocity pattern as in the microchannel case develops inside the constriction. There is thin recirculation region between the fast moving jet and the stationary liquid at wall that obeys the no-slip condition.

Last, we examine the values of **wall shear stress.** It reaches local maxima whenever there is a rapid change in the cross section area of the domain. The global maximum is observed on the upstream edge of the constriction (Figure 8.24). Another maximum occurs as the constriction rapidly expands into the chamber (Figure 8.25).

8.3.2.2 MULTIPLE CASES RESULTS

Quite unfortunately, the reference paper provides only three complete pairs of boundary conditions (as listed in Table 8.4). This limits our possibility to infer trends from observed data. Still, some interesting observations can be made.

We often want to know, what the magnitude of pressure drop across the narrowed domain is. The Figure 8.26 presents the magnitude of **pressure** drop across the constriction as function of

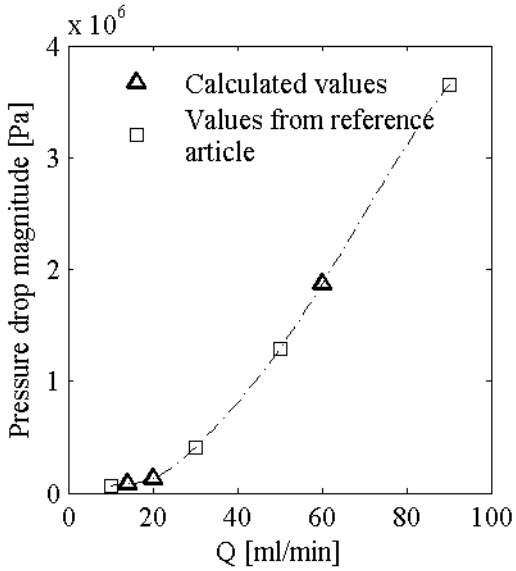

***Figure 8.26:** Pressure drop across the constriction as function of flow rate*

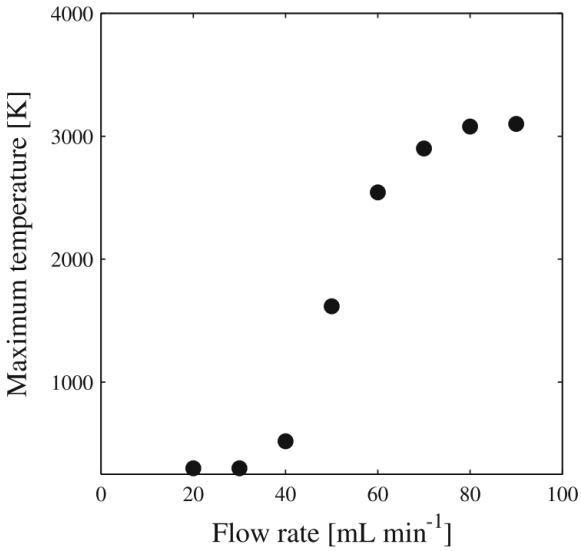

***Figure 8.27**: Maximum temperature of bubble collapse. The values were calculated from Rayleigh-Plesset model [25]*

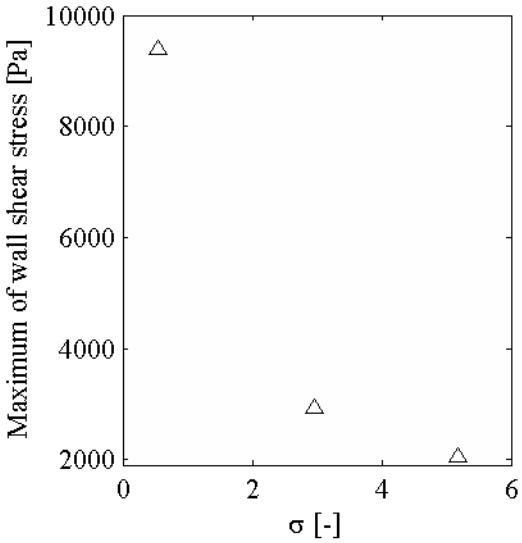

Figure 8.28: *Maximum wall shear stress as function of cavitation number*

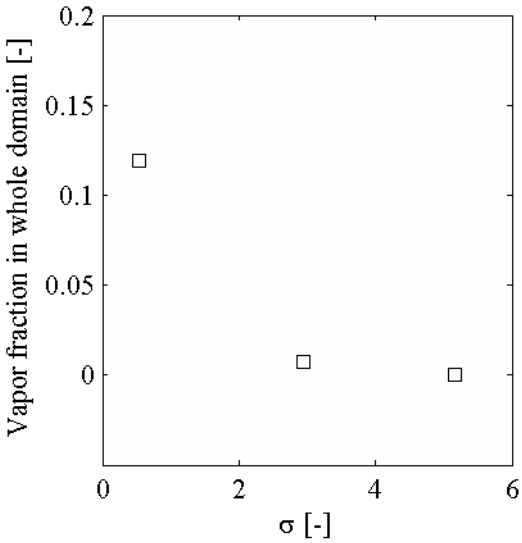

Figure 8.29: *Volume average of the vapor fraction in the whole computational domain*

volumetric flow rate. It includes both the values computed for this thesis and quantities inferred from reference paper. If we recall from chapter five that higher pressure drop results in more severe conditions of bubble collapse, we can also look at the maximum temperature of collapsing bubble calculated by authors of reference paper (see Figure 8.27). It can be observed that at lower flow rates the magnitude of pressure drop is not sufficient to cause rapid nonlinear growth of nuclei and bubble collapse accompanied by high hot-spot temperatures. This, in turn, would translate to no, or very little, species oxidation rate.

We can further evaluate the maximal values of **wall shear stress** found by numerical calculations. Looking at Figure 8.28, we see that the values increase with decreasing cavitation number and follow the same trend as the vapor fraction averaged over the whole computational domain (Figure 8.29). The highest observed wall shear stress is of the order of 9 kPa.

For both cases #2 and #3 the **vapor fraction** in the whole domain is nonzero. It rises to over 11 % for the case #3 and stays only around 1 % for case #2. For the case #1 no cavitation was found in calculations and the vapor fraction is therefore zero. This does not agree completely with results presented in reference paper as it was reported there that cavitation became first observable at this flow rate. Finally, to get better understanding of how the vapor phase develops in time for cases #2 and #3, the reader may wish to consult Appendix where two animations thereof are attached. They were sampled and then created with constant time parameters, therefore we can easily see how much faster the flow moves when the volumetric flow rate is increased threefold. The contours of liquid phase are shown on the plane of symmetry and we can observe that a ring of vapor develops in the constriction. This ring then sheds bubbles to the chamber where they grow only to disappear again once the chamber transitions to smaller outlet channel.

8.3.3 DISCUSSION AND RECOMMENDATIONS

Presented analysis shows major characteristics of cavitation flow in a channel with circular constriction of diameter of the order of hundreds of micrometers. The chosen number of cases, i.e. 3, is relatively low and is not sufficient for reliable deduction of trends. However, no more complete information on boundary conditions were available in the reference paper.

Based on gained insight about the flow in this domain, several recommendations can be made for further work in this area:

- During presented calculations, despite relatively high value of Reynolds number, a laminar model was used. It will be interesting to compare presented results with results obtained from turbulent model. The biggest advantage of the turbulent model should be that it will allow for longer time steps and therefore we will be able to average flow variables over longer periods. In doing so, eventual recurring patterns will become much easier to unravel.
- If significant computational power and certain experience with fluid flow modelling are available, Large Eddy Simulation (LES) may prove fruitful. This enables modelling laminar flows with turbulent regions which is likely the case for a cavitating flow in such a small domain.
- Together with numerical study, an experiment will be of great use as it will help to compare numerical data from three different models (laminar, turbulent, LES) with data measured experimentally. Eventually this can provide greater insight on which model is optimal in this scenario and point out weaknesses and strengths of each of those.
- Another benefit of experimental studies is that they will provide more boundary conditions to be fed into the solver and subsequently more data for comparison and verification.

9 DESIGN OF EXPERIMENT

Computational fluid dynamics (CFD) represent a powerful tool for an engineer. Nevertheless, their results should be closely reviewed, as they are highly dependent on input values. Even a small change of those can lead to significant alterations in resulting flow. In order to validate numerical results it is always highly advisable to carry out accompanying experiments. Following chapter presents a design of such an experiment which is planned in joint cooperation between Brno University of Technology (BUT) and Technical University in Liberec (TUL). The subsections of this chapter describe the design of microfluidic unit, the setup of apparatuses needed for experiment and experimental procedure. Also basics of micro particle image velocimetry (μ-PIV) are sketched out.

This thesis closely follows the work of *Rooze et al.* from reference paper. They investigated the creation of free radicals and subsequent oxidation of selected chemical species and reported it exclusively in the millichannel. This represents the main reason why the millichannel geometry is considered throughout this chapter. Moreover, having larger dimensions than the microchannel, it is easier to fabricate and to be observed experimentally. If a microchannel was to be studied, majority of described steps would remain identic, only a different microfabrication method would have to be chosen.

9.1 DEVICE DESIGN, FABRICATION AND PACKAGING

The device was modelled using Catia CAD software, the dimensions of the channel are given in section 8.3. High magnitudes of pressure are central to cavitation in microfluidics and the device must be capable of withstanding pressure reaching as high as 4 MPa. Therefore the usage of aluminum or carbon steel as base material is both being considered. The channel will be micromachined to the base material on the precise NANOTECH 350FG milling machine at the Regional Centre for Special Optics and Optoelectronic Systems (Turnov OPToElectronic Centre - TOPTEC) using fly-cutting technology. This procedure leads to minimal dimensional deviations and well defined surface roughness along the channel walls.

The microfluidic unit must be also securely packaged to avoid any leaks or ruptures. In order to assure that, a packaging module was designed. The microchannel is micro-machined onto a 10 mm thick plate that constitutes the bottom part of the module as Figure 9.1 shows. The top face is made out of steel and there is a rectangular slot in it. In between these two a Polymethyl methacrylate (PMMA) transparent plate is entrenched. This allows for sufficient transparent area for optical observations while minimizing the fragility of the unit. The top and bottom adapter plates are connected by four ISO 4762 –M3 x 20 screws. The bottom face of the transparent plate as well as the steel plate in contact with it must be highly polished to assure hermetic sealing. Moreover a layer of silicone will be put on contact surfaces to enhance sealing abilities of the unit.

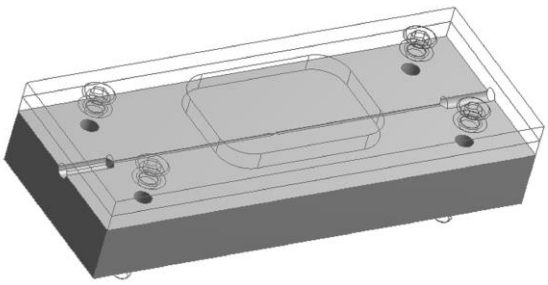

Figure 9.1: *Bottom plate with micro-machined channel and constriction in the middle, the rest of the unit is shown as transparent (device prototype courtesy of D. Jašíková, TUL)*

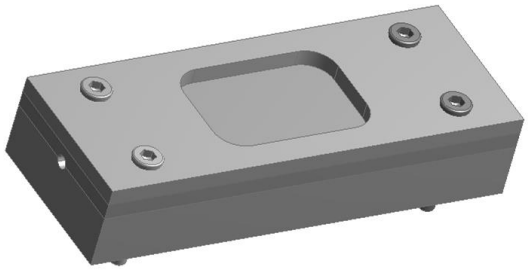

Figure 9.2: *Microfluidic unit with packaging. Four screws connect the top and bottom plate. The top plate has a rectangular slot for optical observations (device prototype courtesy of D. Jašíková, TUL)*

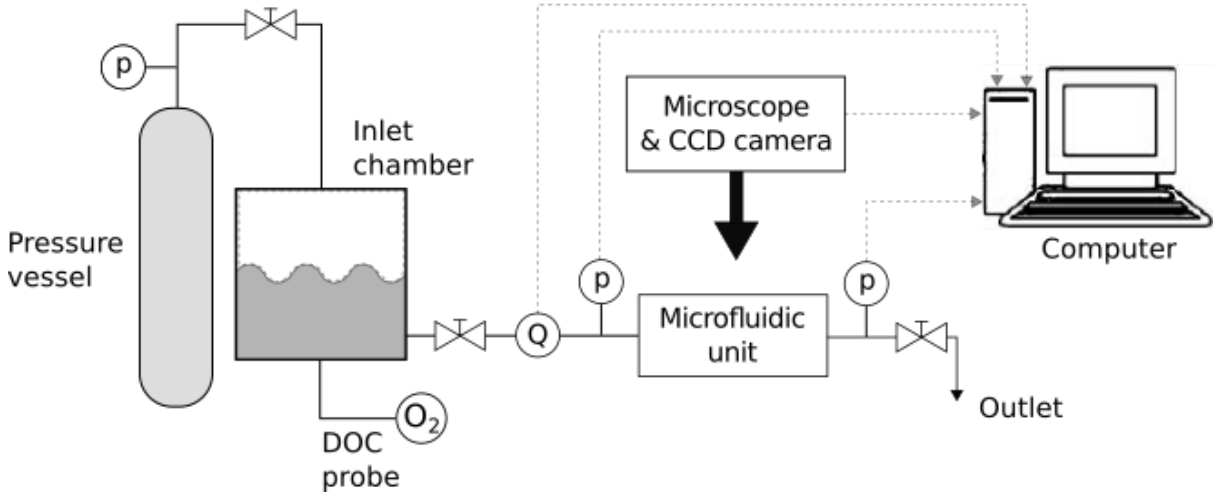

Figure 9.3: *Schematics of experimental setup*

The dimensions of the unit and enclosing module, as shown in Figure 9.2, are $80 \times 30 \times 16\ mm^3$ (length width, height). There are also steel parts in contact with side surfaces that secure the plates in sideways direction. These are not shown in the figure.

9.2 EXPERIMENTAL SETUP

Apart from the microfluidic unit, the experimental circuit consists of several other components. These are shown in scheme in Figure 9.3. The pressure difference between inlet and outlet is achieved by placing a pressure vessel with dry nitrogen at the inlet. On the outlet side of the system a simple water tank is placed, imposing atmospheric pressure. The vessel is connected to a water tank and then to a microfluidic unit by means of high-pressure metal flexible hoses, then another hose leads the liquid out in the exit tank. The hoses are connected to the microfluidic unit via pairs of couplings and nipples. The high pressure requirement holds above all for the upstream part of the experimental track and thinner and cheaper hoses can be chosen for the downstream part.

Right in front and behind the hose connection with microfluidic unit, pressure sensors are located. Their distance from the orifice is $60\ mm$ on both sides. Data from pressure sensors is transmitted to computer running LabView software for storage and further analysis. The optical observations are facilitated by means of a Leica DM IL inverted laboratory microscope together with Neo CMOS 5.5 megapixel camera. The microscope objective zoom is 10x. The observation unit is mounted directly above the transparent window in the upper adapter plate. The volumetric flow is controlled by flow meter placed after water tank at the inlet section and the oxygen concentration is measured before the experiment by the mobile Hach HQ30d oximeter equipped with luminscent dissolved oxygen (LOD) probe.

9.3 EXPERIMENTAL PROCEDURE

Prior to experiment start, no air removal from the system is carried out. Neither the liquid is preliminary treated resulting in usual dissolved oxygen concentration (DOC) of $5 - 7\ ppm$ for tap water and slightly higher for distilled water[16] which are both used in the experiments. The water is not filtered nor recirculated. The ambient temperature is $20\ °C$.

[16] Tap water generally holds less oxygen because the amount of salts already contained in it limits its capability to dissolve further gas. Other conditions like pressurization, open air exposure or temperature should be also considered. [93]

First, the vessel is pressurized to achieve desired pressure difference, then it is allowed to lower its pressure by forcing liquid through the experimental system. The pressure loss at inlet is safely assumed negligible due to small flow rates through the system. The inlet pressure and data from flow meter and pressure sensors are stored for further analysis. The constriction as well as regions up and downstream from it are continuously observed using microscope and a charge-coupled device (CCD) camera. All light-reflecting objects must be covered with dark cloth to prevent reflections from appearing as cavitation bubbles on the video. Eventually, an uncertainty analysis is carried out to accurately interpret measured data.

9.4 MICRO-PIV

Particle image velocimetry (PIV) is often used for the visualization of fluid flow. If we wish to observe flow in micro-scale domain we add magnifying lens system to the traditional setup. Next two subsections provide basics of PIV and description of measurement setup proposed for this experiment.

9.4.1 THEORETICAL INTRODUCTION [3]

The way PIV operates can be described in simplified manner as follows: First, we add particulate seeding tracers to the flowing medium. Common examples include the use of polystyrene latex beads or Rhodamine B. In any case the particles shall be fluorescent. Second, two images of the fluid traces are taken in rapid succession. To achieve high temporal resolution this usually means synchronizing dual pulse laser with a CCD camera. Once two subsequent pictures taken, they are cross-correlated. If one image is $q \times p$ array of brightness values $f(i,j)$ and the second image array of same size but of brightness values $g(i,j)$, than the cross correlation ϕ can be calculated as:

$$\phi(m,n) = \sum_{i=1}^{q}\sum_{i=j}^{p} f(i,j) \cdot g(i+m, j+n), \tag{9.1}$$

where m, n – pixel offsets and i, j – directions.
The cross-correlation is large when two offsets m, n cause two subsequent pictures to overlap as perfectly as possible. If the offsets cause pictures to misalign, the value of ϕ is small. To determine the distance fluid has travelled between the times the two images were taken, we look for maximal value of ϕ. The corresponding pixel offset represents this distance. To obtain complete velocity field, we divide the observed domain into many smaller regions and run the described algorithm on each of those. These regions are called interrogation regions. The spatial resolution increases with decreasing size of interrogation region.

It should be clear to the reader by now that PIV, as described, measures velocity field of particles. If we want to use this field to represent fluid velocity field we must understand and control the relation between them. This usually means assuring that tracers follow the flow well. Two key error sources are (1) body forces on the particles, e.g. forces caused by gravitational or electric fields, and (2) the inertia of particles if their dimensions are too large or they are too dense. We avoid the first error source by ruling out the influence of electric fields and using neutrally buoyant particles, i.e. particles of the same density water has. The second error source can be neglected if the Stokes number of the particle is small, i.e. < 1. This represents the assumption that the viscous force due to the fluid flow is much higher than the inertia. We calculate Stokes number as:

$$Sk = \frac{2v}{d} \cdot \tau_p = \frac{2v}{d} \cdot \frac{d^2 \rho_p}{18\mu} = \frac{d\rho_p v}{9\mu}, \tag{9.2}$$

where v – fluid velocity $[m \cdot s^{-1}]$, d – particle diameter $[m]$, τ_p – particle lag time $[s]$, ρ_p – particle density $[kg \cdot m^{-3}]$, μ – fluid dynamic viscosity $[Pa \cdot s]$.
On the account of low Stokes number, we wish to use small flow tracers. Nevertheless, there is also a restriction on minimal size of used particles. First, they should remain well visible in the taken pictures. Second, with the decreasing particle diameter increases the importance of its random motion due to statistical nature of fluid forces on particles. This is well known **Brownian motion**. The root-mean-square PIV measurement error due to it is:

$$\langle \Delta v \rangle^2 = \frac{2D}{\Delta t}, \tag{9.3}$$

where D – particle diffusivity $[m^2 \cdot s^{-1}]$ and Δt – time between two images are taken $[s]$.
The particle diffusivity is given by **Stokes-Einstein equation**:

$$D = \frac{k_B T}{3\pi\mu d}, \tag{9.4}$$

where $k_B = 1.38 \times 10^{-23}\, J \cdot K^{-1}$ is Boltzmann's constant and T – temperature $[K]$.
Equation (9.3) computes the error owing to the random velocity fluctuations between two exposures and assumes that each exposure is infinitely fast. However if the exposure time is long, the Brownian motion can cause images to be blurred and this may represent another source of errors when inferring the fluid velocity field.

9.4.2 SETUP EMPLOYED FOR MEASUREMENTS

To adapt PIV to microscopic dimensions of the flow domain, Leica DM IL inverted laboratory microscope will be utilized. The objective zoom is 10x. NewWave Gemini Nd:YAG pulse laser with $120\ mJ$ energy per pulse will be used to make tracers fluoresce. The duration of one pulse is $10\ ns$ and the light wavelength $532\ nm$. The pictures will be taken with Neo CMOS camera with 5.5 megapixel resolution and pixel size 6.5 μm. An advanced cross-correlation algorithm is used to improve spatial resolution of μ-PIV measurements. The algorithm adjusts the size of interrogation areas in 8 steps. The area size ranges from 32×32 to 64×64 pixels.

Consistently with previously conducted experiments [90], the particles of Rhodamine B will be used to seed the flow. For particles with diameter 1 μm, density $1\ g/cm^3$ and considering the volumetric flow through millichannel $20\ ml/min$ with resulting average velocity in constriction $13\ m/s$, we can evaluate the Stokes number as follows:

$$Sk = \frac{d\rho_p v_c}{9\mu} = \frac{(1 \times 10^{-6}) \cdot 1\,000 \cdot 13}{9 \cdot 0.001} = 1.4. \tag{9.5}$$

This slightly exceeds the limit of low Stokes number but still remains acceptable, the particles will hence behave as Lagrangian flow tracers, i.e. they will follow the flow well. The error caused by Brownian motion can be neglected as the particle size remains large relative to random displacement fluctuations.

10 CONCLUSION

In the presented work, cavitation in micrometer sized domains was numerically investigated. Prior to calculations, a study of theoretical background information as well as state-of-the-art research was conducted. The calculations are followed by proposal of experiment which is to be conducted in joint cooperation between Brno University of Technology (BUT) and Technical University in Liberec (TUL).

All goals of the thesis were accomplished and are reported on in listed chapters:

- Theoretical introduction to the phenomenon of cavitation (chapters 1–5)
- Study of publications relevant to cavitation in microfluidics (chapter 6 and 7)
- Numerical simulation of flow in a micro-millimeter sized channels (chapter 8)
- Design of experiment (chapter 9)

The main outcomes of the thesis include:

- Guidelines for preprocessing and setup of numerical solutions that can be directly followed up on by another students.
- Analysis of periodically evolving flow in the microchannel and the influence of cavitation number on this behavior. The opposite trend as is the case on macroscale was observed. Several explanations were proposed and tested and eventually a hypothesis was presented together with tips for its verification. Further experimental and numerical work is needed here to better understand the frequency-cavitation number relationship.
- Information on the distribution of phases in the case of cavitation occurring in channels with micro-sized constrictions. Visualization is eased by attaching several animations. The outcomes are presented together with experimental results of other researchers and the results are then compared. The areas of agreement and disagreement are pointed out and this is done mainly to test suitability of laminar model. The model shows good agreement when the pressure difference is achieved by reducing outlet pressure under the atmospheric threshold.
- Report on velocity distribution and how this depends on the location in the channel and the cavitation number. Thin and fast moving liquid jet is observed and regions of intense recirculation are reported. The high velocity gradients present an opportunity for fluid mixing.
- Design of experimental setup and procedure together with the schematics of experimental track and introductory chapter on μ-PIV.
- Recommendations for future numerical projects in this field including the choice of model and length of computational domain.

Other thesis outcomes include concise summary of relevant information on the topic of cavitation in microscale encompassing fluid mechanics and related chemistry. Moreover, brief listing of interesting cavitation applications is included. Numerous references are listed throughout the thesis to make it easier for reader to study the topic in greater depth.

The presented results and methodology will serve as a stepping stone towards further work in this area planned at BUT. Especially comparing the results with different numerical models (turbulent and Large Eddy Simulation) as well as carrying out accompanying experiments promises to be fruitful. Together with foundation laid out the thesis it will allow for determining strengthens and weaknesses of each model. In a like manner, the experiments shall lead to better understanding of not-yet-well-documented phenomena.

11 REFERENCES

[1] ÇENGEL, Yunus a John CIMBALA *Fluid mechanics: fundamentals and applications*. 2nd ed. Boston: McGraw-Hill Higher Education, 2010, xxiii, 994 s. : bar. il. ; 27 cm. 1 CD-ROM. ISBN 9780073529264.

[2] FRANC, Jean-Pierre a Jean-Marie MICHEL. *Fundamentals of cavitation*. Dordrecht: Springer Netherlands, 2005, xxii, 300 p. ISBN 978-904-8166-183.

[3] KIRBY, Brian. *Micro- and Nanoscale Fluid Mechanics: Transport in Microfluidic Devices*. Cambridge: Cambridge University Press, 2010. DOI: 10.1017/CBO9780511760723. ISBN 9780511760723.

[4] LAUTERBORN, Werner a Claus-Dieter OHL. Cavitation bubble dynamics. *Ultrasonics - Sonochemistry* [online]. 1997, **4**(2), 65-75 [cit. 2015-12-19]. DOI: 10.1016/S1350-4177(97)00009-6. ISSN 13504177.

[5] SCHMIDT, Ernst a Ulrich GRIGULL. *Properties of water and steam in SI-units: 0-800 °C , 0-1000 bar = Thermodynamische Eigenschaften von Wasser und Wasserdampf*. 3rd ed. Berlin: Springer-Verlag, 1989, 194 s. 2 přílohy. ISBN 3540096019.

[6] TANDIONO, Tandiono, Dave SIAK-WEI OW, Leonie DRIESSEN, Cara SZE-HUI CHIN, Evert KLASEBOER, Andre BOON-HWA CHOO, Siew-Wan OHL a Claus-Dieter OHL. Sonolysis of Escherichia coli and Pichia pastoris in microfluidics. *Lab on a Chip*. The Royal Society of Chemistry, 2012, **12**(4), 780-786. DOI: 10.1039/C2LC20861J. ISSN 14730197.

[7] GOGATE, Parag. Hydrodynamic Cavitation for Food and Water Processing. *Food and Bioprocess Technology* [online]. New York: Springer-Verlag, 2011, **4**(6), 996-1011 [cit. 2015-12-19]. DOI: 10.1007/s11947-010-0418-1. ISSN 19355130.

[8] MILLY, P., R. TOLEDO, W. KERR a D. ARMSTEAD Hydrodynamic Cavitation: Characterization of a Novel Design with Energy Considerations for the Inactivation of Saccharomyces cerevisiae in Apple Juice. *Journal of Food Science* [online]. Malden, USA: Blackwell Publishing Inc, 2008, **73**(6), 298-303 [cit. 2015-12-19]. DOI: 10.1111/j.1750-3841.2008.00827.x. ISSN 00221147.

[9] CHAND, Rashmi, David BREMNER, Kyu NAMKUNG, Phillip COLLIER a Parag GOGATE Water disinfection using the novel approach of ozone and a liquid whistle reactor. *Biochemical Engineering Journal* [online]. 2007, **35**(3), 357-364 [cit. 2015-12-19]. DOI: 10.1016/j.bej.2007.01.032. ISSN 1369703X.

[10] BRAEUTIGAM, P., M. FRANKE, Z. WU a B. ONDRUSCHKA Role of Different Parameters in the Optimization of Hydrodynamic Cavitation. *Chemical Engineering & Technology* [online]. Weinheim: WILEY-VCH Verlag, 2010, **33**(6), 932-940 [cit. 2015-12-19]. DOI: 10.1002/ceat.201000021. ISSN 09307516.

[11] GOGATE, Parag, Irfan SHIRGAONKAR, M. SIVAKUMAR, P. SENTHILKUMAR, Nilesh VICHARE a Aniruddha PANDIT Cavitation reactors: Efficiency assessment using a model reaction. *AIChE Journal* [online]. Hoboken: Wiley Subscription Services, Inc., A Wiley Company, 2001, **47**(11), 2526-2538 [cit. 2015-12-19]. DOI: 10.1002/aic.690471115. ISSN 00011541.

[12] YAN, Y a R.B THORPE. Flow regime transitions due to cavitation in the flow through an orifice. *International Journal of Multiphase Flow* [online]. 1990, **16**(6), 1023-1045 [cit. 2015-12-19]. DOI: 10.1016/0301-9322(90)90105-R. ISSN 03019322.

[13] SINGH, Randip a Yoav PELES. The effects of fluid properties on cavitation in a micro domain. *Journal of Micromechanics and Microengineering* [online]. 2009, **19**(2), 025009 [cit. 2015-12-19]. DOI: 10.1088/0960-1317/19/2/025009. ISSN 09601317.

[14] MISHRA, C. a Y. PELES Size scale effects on cavitating flows through microorifices entrenched in rectangular microchannels. *Microelectromechanical Systems, Journal of* [online]. USA: IEEE, 2005, **14**(5), 987-999 [cit. 2015-12-19]. DOI: 10.1109/JMEMS.2005.851800. ISSN 10577157.

[15] BRDIČKA, Miroslav, Oldřich TARABA a Ladislav SAMEK. *Kavitace: diagnostika a technické využití*. 1. vyd. Praha: SNTL, 1981, 332 s. : obr., fot., tb. ; 25 cm.

[16] TEMPERLEY, H. The behaviour of water under hydrostatic tension: II. *Proceedings of the Physical Society* [online]. 1946, **58**(4), 436-443 [cit. 2015-12-19]. DOI: 10.1088/0959-5309/58/4/311. ISSN 09595309.

[17] BRIGGS, Lyman Limiting Negative Pressure of Water. *Journal of Applied Physics*. 1950, **21**(7), 721-722. DOI: 10.1063/1.1699741. ISSN 00218979.

[18] PEASE, D a L BLINKS. Cavitation from solid surfaces in the absence of gas nuclei. *The Journal of physical and colloid chemistry* [online]. 1947, **51**(2), 556 [cit. 2015-12-19]. ISSN 00927023.

[19] BILLET, M.L. Cavitation nuclei measurements with an optical system. *TRANS. ASME J. FLUIDS ENGNG* [online]. 1986, **108**(3) [cit. 2015-12-19]. ISSN 00982202.

[20] HOLL, J.W. Nuclei and cavitation. *J Basic Eng Trans ASME* [online]. 1970, **92**(4), 681-688 [cit. 2015-12-19].

[21] BLAKE, F.G. *The Onset of Cavitation in Liquids: Cavitation threshold sound pressure in water as a function of temperature and hydrostatic pressure. I*. USA: Acoustics Research Laboratory, Department of Engineering Sciences and Applied Physics, Harvard University, 1949. PhD Thesis. Harvard University.

[22] HARVEY, E.N., W.D. MC ERLOY a A.H. WHITELEY On Cavity Formation in Water. *Journal of Applied Physics* [online]. AIP, 1947, **18**(162), 162-172 [cit. 2015-12-19]. DOI: 10.1063/1.1697598. ISSN 00218979.

[23] HSIEH, Din-Yu a Milton PLESSET Theory of Rectified Diffusion of Mass into Gas Bubbles. *The Journal of the Acoustical Society of America* [online]. ASA, 1961, **33**(2), 206-215 [cit. 2015-12-19]. DOI: 10.1121/1.1908621.

[24] DIDENKO, Yuri a Kenneth SUSLICK The energy efficiency of formation of photons, radicals and ions during single-bubble cavitation. *Nature* [online]. Nature Publishing Group, 2002, **418**(6896), 394-397 [cit. 2015-12-19]. DOI: 10.1038/nature00895. ISSN 00280836.

[25] ROOZE, Joost, Matthieu ANDRÉ, Gert-Jan GULIK, David FERNÁNDEZ-RIVAS, Johannes GARDENIERS, Evgeny REBROV, Jaap SCHOUTEN a Jos KEURENTJES. Hydrodynamic cavitation in micro channels with channel sizes of 100 and 750 micrometers. *Microfluidics and Nanofluidics* [online]. Berlin/Heidelberg: Springer-Verlag, 2012, **12**(1), 499-508 [cit. 2015-12-19]. DOI: 10.1007/s10404-011-0891-5. ISSN 16134982.

[26] FRANC, Jean-Pierre. The Rayleigh-Plesset equation: a simple and powerful tool to understand various aspects of cavitation. *Fluid Dynamics of Cavitation and Cavitating Turbopumps, CISM Courses and Lectures, vol. 496*. Wien: Springer, 2007, **496**, s. 1-41. DOI: 10.1007/978-3-211-76669-9. ISBN 3211766685.

[27] FLYNN, H. Physics of acoustic cavitation in liquids (Acoustic cavitation phenomena including single cavity equations of motion, transient cavity collapse, cavitation nucleus models, etc.). In: *Physics of acoustic cavitation in liquids (Acoustic cavitation phenomena including single cavity equations of motion, transient cavity collapse, cavitation nucleus models, etc.)* [online]. New York: Academic Press, 1964, s. 58-172 [cit. 2015-12-19].

[28] NEPPIRAS, E.A. a B.E. NOLTINGK Cavitation produced by ultrasonics: Theoretical conditions for the onset of cavitation. *Proceedings of the Physical Society. Section B* [online]. 1951, **64**(12), 1032-1038 [cit. 2015-12-19]. DOI: 10.1088/0370-1301/64/12/302. ISSN 03701301.

[29] VOROTNIKOVA, M.I. a R.I. SOLOUKHIN A calculation of the pulsations of gas bubbles in an incompressible fluid subject to a periodically varying pressure. *Akust. Zh.* 1964, **10**(1), 28-32. ISSN 0066-4189.

[30] CONNOLLY, W. Ultrasonic Cavitation Thresholds in Water. *The Journal of the Acoustical Society of America*. 1954, **26**(5), 843-848. DOI: 10.1121/1.1907427. ISSN 00014966.

[31] STOKER, J.J. *Nonlinear vibrations in mechanical and electrical systems*. Michigan: Wiley-Interscience, 1992. ISBN 978-0471570332.

[32] NEGISHI, Katsuo. Experimental Studies on Sonoluminescence and Ultrasonic Cavitation. *Journal of the Physical Society of Japan* [online]. Tokyo: The Physical Society of Japan, 1961, **16**(7), 1450 [cit. 2015-12-19]. ISSN 00319015.

[33] KAMATH, V., A. PROSPERETTI a F.N. EGOLFOPOULOS A theoretical study of sonoluminescence. *The Journal of the Acoustical Society of America* [online]. 1993, **94**(1), 248-246 [cit. 2015-12-19]. DOI: 10.1121/1.407083. ISSN 00014966.

[34] MCNAMARA, William, Yuri DIDENKO a Kenneth SUSLICK Sonoluminescence Temperatures During Multi-Bubble Cavitation. *Nature* [online]. Nature Publishing Group, 1999, **401**(6755), 772-775 [cit. 2015-12-19]. DOI: 10.1038/44536.

[35] HILGENTFELD, S, S GROSSMAN a D LOHSE. Sonoluminescence light emission. *Physics of Fluids* [online]. AIP, 1999, **11**(6), 1318-1330 [cit. 2015-12-19]. DOI: 10.1063/1.869997. ISSN 10706631.

[36] LOHSE, Detlef a Sascha HILGENFELDT. Inert gas accumulation in sonoluminescing bubbles. *The Journal of Chemical Physics* [online]. AIP, 1997, **107**, 6986-6997 [cit. 2015-12-20]. DOI: 10.1063/1.474939. ISSN 00219606.

[37] MASON, T. a J. LORIMER. *Applied sonochemistry: the uses of power ultrasound in chemistry and processing*. Weinheim: Wiley-VCH, 2002. ISBN 3527302050.

[38] SUSLICK, K.S., M.M. MDLELENI a J.T. RIES Chemistry Induced by Hydrodynamic Cavitation. *Journal of the American Chemical Society* [online]. American Chemical Society, 1997, **119**(39) [cit. 2015-12-19]. DOI: 10.1021/ja972171i. ISSN 00027863.

[39] STOREY, Brian a Andrew SZERI Water Vapour, Sonoluminescence and Sonochemistry. *Proceedings: Mathematical, Physical and Engineering Sciences* [online]. The Royal Society, 2000, **456**(1999), 1685-1709 [cit. 2015-12-20]. ISSN 13645021.

[40] SUSLICK, Kenneth Applications of ultrasound to materials chemistry. *MRS Bulletin* [online]. Materials Research Society, 1995, **20**(4), 29-34 [cit. 2015-12-19]. ISSN 08837694.

[41] MASON, T.J. *Advances in Sonochemistry, Volume 4*. Amsterdam: Elsevier Science, 1996. ISBN 9781559387934.

[42] PRICE, Gareth. ROYAL SOCIETY OF CHEMISTRY (GREAT BRITAIN). *Current trends in sonochemistry*. Cambridge: Royal Society of Chemistry, 1992. ISBN 0851863655.

[43] BRAEUTIGAM, P., Z. WU, A. STARK a B. ONDRUSCHKA Degradation of BTEX in Aqueous Solution by Hydrodynamic Cavitation. *Chemical Engineering & Technology* [online]. Weinheim: WILEY-VCH Verlag, 2009, **32**(5), 745-753 [cit. 2015-12-19]. DOI: 10.1002/ceat.200800626. ISSN 09307516.

[44] YOUNG, F.. Sonoluminescence from water containing dissolved gases. *The Journal of the Acoustical Society of America* [online]. ASA, 1976, **60**, 100 [cit. 2015-12-19]. DOI: 10.1121/1.381076. ISSN 00014966.

[45] SUSLICK, K.S., J.J. GAWIENOWSKI, P.F. SCHUBERT a H.H. WANG Sonochemistry in non-aqueous liquids. *Ultrasonics* [online]. 1984, **22**(1), 33-36 [cit. 2015-12-19]. DOI: 10.1016/0041-624X(84)90059-3. ISSN 0041624X.

[46] IBISI, M. a B. BROWN Variation of the Relative Intensity of Cavitation with Temperature. *The Journal of the Acoustical Society of America* [online]. ASA, 1967, **41**, 568 [cit. 2015-12-19]. DOI: 10.1121/1.1910381.

[47] SEHGAL, C., R.G. SUTHERLAND a R.E. VERRALL Sonoluminescence intensity as a function of bulk solution temperature. *Journal of Physical Chemistry* [online]. 1980, **84**(5), 525-528 [cit. 2015-12-19]. DOI: 10.1021/j100442a015. ISSN 00223654.

[48] TANDIONO, Siew-Wan, Dave OHL, Evert OW, Victor KLASEBOER, Rainer WONG, Claus-Dieter DUMKE a Claus-Dieter OHL. Sonochemistry and sonoluminescence in microfluidics. *Proceedings of the National Academy of Sciences of the United States of America* [online]. 2011, **108**(15), 5996 [cit. 2015-12-22]. DOI: 10.1073/pnas.1019623108.

[49] RADI, R, T COSGROVE, J BECKMAN a B FREEMAN. Peroxynitrite-induced luminol chemiluminescence. *Biochemical Journal* [online]. 1993, **290**(1), 51-57 [cit. 2015-12-22]. DOI: 10.1042/bj2900051. ISSN 02646021.

[50] FERNANDES, Fabiano, Francisca OLIVEIRA a Sueli RODRIGUES. Use of Ultrasound for Dehydration of Papayas. *Food and Bioprocess Technology* [online]. New York: Springer-Verlag, 2008, **1**(4), 339-345 [cit. 2015-12-19]. DOI: 10.1007/s11947-007-0019-9. ISSN 19355130.

[51] TIWARI, B., C. O' DONNELL, K. MUTHUKUMARAPPAN a P. CULLEN Effect of Low Temperature Sonication on Orange Juice Quality Parameters using Response Surface Methodology. *Food and Bioprocess Technology* [online]. New York: Springer-Verlag, 2009, **2**(1), 109-114 [cit. 2015-12-19]. DOI: 10.1007/s11947-008-0156-9. ISSN 19355130.

[52] WALKLING-RIBEIRO, M., F. NOCI, J. RIENER, D. CRONIN, J. LYNG a D. MORGAN The Impact of Thermosonication and Pulsed Electric Fields on Staphylococcus aureus Inactivation and Selected Quality Parameters in Orange Juice. *Food and Bioprocess Technology* [online]. New York: Springer-Verlag, 2009, **2**(4), 422-430 [cit. 2015-12-19]. DOI: 10.1007/s11947-007-0045-7. ISSN 19355130.

[53] LUCHE, Jean-Louis. *Synthetic organic sonochemistry*. New York: Plenum Press, 1998. ISBN 0306459167.

[54] MASON, Timothy a J. LORIMER. *Sonochemistry: theory, applications and uses of ultrasound in chemistry*. Ellis Horwood ;--Halsted Press distributor, 1988. ISBN 0745802400.

[55] MILLY, P., R. TOLEDO, M. HARRISON a D. ARMSTEAD Inactivation of Food Spoilage Microorganisms by Hydrodynamic Cavitation to Achieve Pasteurization and Sterilization of Fluid Foods. *Journal of Food Science* [online]. Malden, USA: Blackwell Publishing Inc, 2007, **72**(9), 414-422 [cit. 2015-12-19]. DOI: 10.1111/j.1750-3841.2007.00543.x. ISSN 00221147.

[56] DE BONIS, Maria a Gianpaolo RUOCCO. Heat and mass transfer modeling during continuous flow processing of fluid food by direct steam injection. *International Communications in Heat and Mass Transfer* [online]. 2010, **37**(3), 239-244 [cit. 2015-12-19]. DOI: 10.1016/j.icheatmasstransfer.2009.09.008. ISSN 07351933.

[57] MAHULKAR, A., P. BAPAT, A. PANDIT a F. LEWIS Steam bubble cavitation. *AIChE Journal* [online]. Hoboken: Wiley Subscription Services, Inc., A Wiley Company, 2008, **54**(7), 1711-1724 [cit. 2015-12-19]. DOI: 10.1002/aic.11509. ISSN 00011541.

[58] GECIOVA, Jana, Dean BURY a Paul JELEN. Methods for disruption of microbial cells for potential use in the dairy industry—a review. *International Dairy Journal* [online]. 2002, **12**(6), 541-553 [cit. 2015-12-19]. DOI: 10.1016/S0958-6946(02)00038-9. ISSN 09586946.

[59] HARRISON, Susan. Bacterial cell disruption: A key unit operation in the recovery of intracellular products. *Biotechnology Advances* [online]. 1991, **9**(2), 217-240 [cit. 2015-12-19]. DOI: 10.1016/0734-9750(91)90005-G. ISSN 07349750.

[60] SAVE, S.S., A.B. PANDIT a J.B. JOSHI Use of Hydrodynamic Cavitation for Large Scale Microbial Cell Disruption. *Food and Bioproducts Processing* [online]. 1997, **75**(1), 41-49 [cit. 2015-12-19]. DOI: 10.1205/096030897531351. ISSN 09603085.

[61] CHISTI, Yusuf a Murray MOO-YOUNG. Disruption of microbial cells for intracellular products. *Enzyme and Microbial Technology* [online]. 1986, **8**(4), 194-204 [cit. 2015-12-19]. DOI: 10.1016/0141-0229(86)90087-6. ISSN 01410229.

[62] FARKADE, Vivek, Sue HARRISON a Aniruddha PANDIT Heat induced translocation of proteins and enzymes within the cell: an effective way to optimize the microbial cell disruption process. *Biochemical Engineering Journal* [online]. 2005, **23**(3), 247-257 [cit. 2015-12-19]. DOI: 10.1016/j.bej.2005.01.001. ISSN 1369703X.

[63] ANAND, H., B. BALASUNDARAM, A.B. PANDIT a S.T.L. HARRISON The effect of chemical pretreatment combined with mechanical disruption on the extent of disruption and release of intracellular protein from E. coli. *Biochemical Engineering Journal* [online]. 2007, **35**(2), 166-173 [cit. 2015-12-19]. DOI: 10.1016/j.bej.2007.01.011. ISSN 1369703X.

[64] BAIRD, N. Free radical reactions in aqueous solutions: Examples from advanced oxidation processes for wastewater and from the chemistry in airborne water droplets. *Journal of Chemical Education* [online]. Easton: American Chemical Society, 1997, **74**(7), 817-819 [cit. 2015-12-19]. DOI: 10.1021/ed074p817. ISSN 00219584.

[65] WANG, X, Y ZHANG a X WANG. Degradation of alachlor in aqueous solution by using hydrodynamic cavitation. *Journal of Hazardous Materials* [online]. Elsevier BV, 2009, **161**(1), 202-207 [cit. 2015-12-19]. DOI: 10.1605/01.301-0004071779.2008.

[66] JYOTI, K.K a A.B PANDIT. Water disinfection by acoustic and hydrodynamic cavitation. *Biochemical Engineering Journal* [online]. 2001, **7**(3), 201-212 [cit. 2015-12-19]. DOI: 10.1016/S1369-703X(00)00128-5. ISSN 1369703X.

[67] JANČULA, Daniel, Přemysl MIKULA, Blahoslav MARŠÁLEK, Pavel RUDOLF a František POCHYLÝ. Selective method for cyanobacterial bloom removal: hydraulic jet cavitation experience. *Aquaculture International* [online]. Cham: Springer International Publishing, 1404, **22**(2), 509-521 [cit. 2015-12-22]. DOI: 10.1007/s10499-013-9660-7. ISSN 09676120.

[68] COSTA, Pedro, Maria BOTELHO a Susana RODRIGUES. Accumulation of paralytic shellfish toxins in digestive gland of Octopus vulgaris during bloom events including the dinoflagellate Gymnodinium catenatum. *Marine Pollution Bulletin* [online]. 2009, **58**(11), 1747-1750 [cit. 2015-12-22]. DOI: 10.1016/j.marpolbul.2009.08.005. ISSN 0025326X.

[69] SMITH, Juliette, Greg BOYER a Paul ZIMBA A review of cyanobacterial odorous and bioactive metabolites: Impacts and management alternatives in aquaculture. *Aquaculture* [online]. Elsevier B.V, 2008, **280**(1-4), 5-20 [cit. 2015-12-22]. DOI: 10.1016/j.aquaculture.2008.05.007. ISSN 00448486.

[70] OHL, Claus-Dieter, Manish ARORA, Roy IKINK, Nico DE JONG, Michel VERSLUIS, Michael DELIUS a Detlef LOHSE. Sonoporation from Jetting Cavitation Bubbles. *Biophysical Journal* [online]. 2006, **91**(11), 4285-4295 [cit. 2015-12-22]. DOI: 10.1529/biophysj.105.075366. ISSN 00063495.

[71] LONDON, A.P., A.A. AYÓN, A.H. EPSTEIN, S.M. SPEARING, T. HARRISON, Y. PELES a J.L. KERREBROCK Microfabrication of a high pressure bipropellant rocket engine. *Sensors & Actuators: A. Physical* [online]. 2001, **92**(1), 351-357 [cit. 2015-12-19]. DOI: 10.1016/S0924-4247(01)00571-4. ISSN 09244247.

[72] BURGER, J., H. HOLLAND, E. BERENSCHOT, J.-H. SEPPENWOOLDE, M. TER BRAKE, H. GARDENIERS a M. ELWENSPOEK 169 kelvin cryogenic microcooler employing a condenser, evaporator, flow restriction and counterflow heat exchangers. In: *Micro Electro Mechanical Systems, 2001. MEMS 2001. The 14th IEEE International Conference on* [online]. USA: IEEE, 2001, s. 418-421 [cit. 2015-12-19]. DOI: 10.1109/MEMSYS.2001.906567. ISBN 0780359984. ISSN 10846999.

[73] LEONI, R. On-chip micro-refrigerators for sub-Kelvin cooling. *New Astronomy Reviews* [online]. 1999, **43**(2), 317-327 [cit. 2015-12-19]. DOI: 10.1016/S1387-6473(99)00024-X. ISSN 13876473.

[74] YANG, Ren. A rapid micro-mixer/reactor based on arrays of spatially impinging micro-jets. *Journal of Micromechanics and Microengineering* [online]. 2004, **14**(10), 1345-1351 [cit. 2015-12-19]. DOI: 10.1088/0960-1317/14/10/008. ISSN 09601317.

[75] EPSTEIN, A.H., S.D. SENTURIA, G. ANATHASURESH et al. Power MEMS and microengines. In: *Solid State Sensors and Actuators, 1997. TRANSDUCERS '97 Chicago., 1997 International Conference on* [online]. Chicago, IL: IEEE Publishing, 1997, **2**, s. 753-756 [cit. 2015-12-19]. DOI: 10.1109/SENSOR.1997.635209. ISBN 0780338294.

[76] RICHTER, M., P. WOIAS a D. WEIβ Microchannels for applications in liquid dosing and flow-rate measurement. *Sensors & Actuators: A. Physical* [online]. 1997, **62**(1), 480-483 [cit. 2015-12-19]. DOI: 10.1016/S0924-4247(97)01486-6. ISSN 09244247.

[77] LOSEY, M.W., R.J. JACKMAN, S.L. FIREBAUGH, M.A. SCHMIDT a K.F. JENSEN Design and fabrication of microfluidic devices for multiphase mixing and reaction. *Microelectromechanical Systems, Journal of* [online]. USA: IEEE, 2002, **11**(6), 709-717 [cit. 2015-12-19]. DOI: 10.1109/JMEMS.2002.803416. ISSN 10577157.

[78] ANDERSON, Rolfe, Gregory BOGDAN, Zuri BARNIV, Timothy DAWES, James WINKLER a Kajal ROY. Microfluidic biochemical analysis system. *International Conference on Solid-State Sensors and Actuators, Proceedings* [online]. IEEE, 1997, **1**, 477-480 [cit. 2015-12-19].

[79] HUH, Dongeun, Yi-Chung TUNG, Hsien-Hung WEI, James GROTBERG, Steven SKERLOS, Katsuo KURABAYASHI a Shuichi TAKAYAMA. Use of Air-Liquid Two-Phase Flow in Hydrophobic Microfluidic Channels for Disposable Flow Cytometers. *Biomedical Microdevices* [online]. Boston: Kluwer Academic Publishers, 2002, **4**(2), 141-149 [cit. 2015-12-19]. DOI: 10.1023/A:1014691416614. ISSN 13872176.

[80] CHAMBERS, D., H. BARTLETT a L. CECCIO Determination of the In Vivo Cavitation Nuclei Characteristics of Blood. *ASAIO Journal* [online]. Copyright © 1999 by the American Society for Artificial Internal Organs, 1999, **45**(6), 541-549 [cit. 2015-12-19]. ISSN 10582916.

[81] FERNANDEZ RIVAS, David, Andrea PROSPERETTI, Aaldert ZIJLSTRA, Detlef LOHSE a Han GARDENIERS Efficient Sonochemistry through Microbubbles Generated with Micromachined Surfaces. *Angewandte Chemie International Edition* [online]. Weinheim: WILEY-VCH Verlag, 2010, **49**(50), 9699-9701 [cit. 2015-12-19]. DOI: 10.1002/anie.201005533. ISSN 14337851.

[82] ARROJO, S. a Y. BENITO A theoretical study of hydrodynamic cavitation. *Ultrasonics - Sonochemistry* [online]. 2008, **15**(3), 203-211 [cit. 2015-12-19]. DOI: 10.1016/j.ultsonch.2007.03.007. ISSN 13504177.

[83] TULLIS, J a R GOVINDARAJAN. Cavitation and Size Scale Effects for Orifices. *Journal of Hydraulic Engineering* [online]. 1973, **99**(3), 417-430 [cit. 2015-12-19].

[84] TANDIONO, Siew-Wan, Dave OHL, Evert OW, Victor KLASEBOER, Andrea WONG, Claus-Dieter CAMATTARI a Claus-Dieter OHL. Creation of cavitation activity in a microfluidic device through acoustically driven capillary waves. *Lab on a chip* [online]. 2010, **10**(14), 1848 [cit. 2015-12-22]. DOI: 10.1039/c002363a. ISSN 14730197.

[85] TAYLOR, Michael, Phillip BELGRADER, Burford FURMAN a Farzad POURAHMADI. Lysing bacterial spores by sonication through a flexible interface in a microfluidic system. *Analytical Chemistry* [online]. Washington: American Chemical Society, 2001, **73**(3), 492-496 [cit. 2015-12-22]. ISSN 00032700.

[86] MISHRA, Chandan a Yoav PELES. Flow visualization of cavitating flows through a rectangular slot micro-orifice ingrained in a microchannel. *Physics of Fluids* [online]. AIP, 2005, **17**(11), 13602-13616 [cit. 2016-04-10]. DOI: 10.1063/1.2132289. ISSN 10706631.

[87] *ANSYS Fluent Theory Guide 15.0* [online]. Canonsburg, PA: ANSYS, Inc., 2013 [cit. 2016-04-10]. Dostupné z: http://148.204.81.206/Ansys/150/ANSYS%20Fluent%20Theory%20Guide.pdf

[88] SRINIVASAN, Vedanth, Abraham J. SALAZAR a Kozo SAITO. Numerical simulation of cavitation dynamics using a cavitation-induced-momentum-defect (CIMD) correction approach. *Applied Mathematical Modelling* [online]. 2009, **33**(3), 1529-1559 [cit. 2016-04-10]. DOI: 10.1016/j.apm.2008.02.005. ISSN 0307904X.

[89] SHOU-SHING HSIEH, . Liquid flow in a micro-channel. *Journal of Micromechanics and Microengineering* [online]. 2004, **14**(4), 436-445 [cit. 2016-05-07]. DOI: 10.1088/0960-1317/14/4/002. ISSN 09601317.

[90] JASIKOVA, D., M. KOTEK a V. KOPECKY The feasible study of the water flow in the micro channel with the Y-junction and narrow structure for various flow rates. *EPJ Web of Conferences*. 2015, **2015**(92), 02030-1-02030-6. DOI: dx.doi.org/10.1051/epjconf/20159202030.

[91] SILBEY, Robert, Robert ALBERTY a Moungi BAWENDI. *Physical chemistry*. 4th ed. Hoboken: John Wiley, 2005, vii, 944 s. : il. ISBN 047121504X.

[92] HATANAKA, Shin-ichi, Hideto MITOME, Kyuichi YASUI a Shigeo HAYASHI. Single-bubble sonochemiluminescence in aqueous luminol solutions. *Journal of the American Chemical Society* [online]. 2002, **124**(35), 10250-10251 [cit. 2016-02-02]. DOI: 10.1021/ja0258475. ISSN 00027863.

[93] Is dissolved oxygen higher in tap water or distilled water?. *ResearchGate* [online]. Berlin, Germany: ResearchGate GmbH, 2013 [cit. 2016-05-10]. Dostupné z: https://www.researchgate.net/post/Is_dissolved_oxygen_higher_in_tap_water_or_distilled_water

12 LIST OF APPENDICES

APPENDIX A

CD containing animations of changing contours of liquid volume fraction for:

- Microchannel, case #1
- Microchannel, case #5
- Microchannel, case #6
- Millichannel, case #2
- Millichannel, case #3